

UC Riverside

UC Riverside Electronic Theses and Dissertations

Title

Mathematical Modeling of Hair Follicle Regeneration Dynamics and of Polarization Initiation

Permalink

<https://escholarship.org/uc/item/5f58p42t>

Author

Duran, Cecilia

Publication Date

2024

Copyright Information

This work is made available under the terms of a Creative Commons Attribution-NonCommercial-NoDerivatives License, available at

<https://creativecommons.org/licenses/by-nc-nd/4.0/>

Peer reviewed|Thesis/dissertation

UNIVERSITY OF CALIFORNIA
RIVERSIDE

Mathematical Modeling of Hair Follicle Regeneration Dynamics and of Polarization
Initiation

A Dissertation submitted in partial satisfaction
of the requirements for the degree of

Doctor of Philosophy

in

Mathematics

by

Cecilia C. Duran

March 2024

Dissertation Committee:

Dr. Qixuan Wang, Co-Chairperson

Dr. Weitao Chen, Co-Chairperson

Dr. Yat Tin Chow

Copyright by
Cecilia C. Duran
2024

The Dissertation of Cecilia C. Duran is approved:

Committee Co-Chairperson

Committee Co-Chairperson

University of California, Riverside

Acknowledgements

Thank you to my husband and my family for their unwavering love and support. Their encouragement and belief in me have been the most important part of my journey. I would also like to thank my advisors Dr. Qixuan Wang and Dr. Weitao Chen for all their help in my research work, and for not letting me give up during challenging times. Also thank you to all my peers and anyone with whom I've had positive interactions throughout my educational career. Special acknowledgements to those who shared in the demanding hours and rigorous work that a mathematics degree entails, this support and camaraderie have been invaluable in this endeavor.

To my parents.

ABSTRACT OF THE DISSERTATION

Mathematical Modeling of Hair Follicle Regeneration Dynamics and of Polarization
Initiation

by

Cecilia C. Duran

Doctor of Philosophy, Graduate Program in Mathematics

University of California, Riverside, March 2024

Dr. Qixuan Wang, Co-Chairperson

Dr. Weitao Chen, Co-Chairperson

This thesis consists of two parts.

In the first part, we develop an ODE cell differentiation population model to study the dynamics of hair follicles (HFs). In particular, we wish to understand the mechanisms underlying the cyclical regenerations that this mammalian organ undergoes throughout an organism's lifetime. We'd also like to study the effect of ionizing radiation (IR) on the regeneration processes. In brief, the cycle of a HF consists of three consecutive phases: anagen—the active proliferation phase, catagen—the degeneration phase, and telogen—the resting phase, and while HFs undergo irreversible degeneration during the catagen phase, recent experimental research on mice shows that when anagen HFs are subject to IR, they undergo a transient degeneration, followed by a nearly full regeneration that makes the HFs return to homeostatic state. In our model we propose various feedback mechanisms and study their role in determining the degenerative and regenerative behavior of HF cells. The model is built based on current theoretical knowledge in biology and model parameters are calibrated to IR experimental data. We perform bifurcation and sensitivity analyses to determine the effect of IR exposure on the stability of the HF homeostatic steady state and compare with the dynamics of the irreversible degeneration during catagen.

The second part is motivated by the biological process of cell polarization. Cell polarity refers to the asymmetrical spatial distribution of molecules and substances within a cell or cell membrane, which occurs as a response to internal or external stimuli. In this work, we study autonomous reaction-diffusion models to find mechanisms that can lead to polarization at a single cell-membrane. In particular, we investigate the role that positive and negative feedbacks play in the early polarization process. We first perform and document ample tests for various reaction-diffusion models using three numerical methods; two of them are based on fast Fourier transform (FFT) differentiation, while the third model is of finite-difference type. The performance of the numerical methods is compared while simultaneously selecting those reaction-diffusion models that are likely to attain polarization. We then present a more detailed investigation of two reaction-diffusion models which include diffusion-inhibiting negative feedback and a positive production feedback; these models are studied using one of the FFT-based numerical methods. A similar analysis for the remaining numerical methods is pending and will be detailed in the discussion section of this part of the thesis.

Contents

List of Figures	x
List of Tables	xiv
I Modeling of Ionizing Radiation Induced Hair Follicle Regenerative Dynamics	1
1 Introduction	2
1.1 Hair Cycle Biology and Modeling Background	3
1.2 Development of HF ODE Model	7
Summary of HF Biology and Model Assumptions	7
HF Cell Differentiation Population Model.....	8
Derivation of Model Equations 1.1.....	10
Modeling IR Effect on HF Regeneration	16
Modeling of Mx Lineage Tracing after IR	17
1.3 Model Parameters	18
Information from Control Case.....	18
Summary of Major Discoveries from IR Experimental Results	20
2 Results	22
2.1 Parameter Calibration	22
Simulation Results	27
2.2 Stability of the Homeostatic State of Anagen HF.....	30
Linear Stability Analysis.....	30
Local Sensitivity Analysis	32
Global Sensitivity Analysis	34
Bifurcation Analysis.....	36
2.3 Modeling Effect of PGE2 Treatment on IR-exposed HF	42
3 Conclusions and Discussion	46

II	Autonomous Regulation can Produce Robust Polarization Pattern	55
4	Introduction	56
4.1	Preliminaries	58
4.2	Numerical Methods.....	61
	Simulation Tests.....	63
4.3	Methodology	70
5	Results	73
5.1	Model 1.....	74
5.2	Model 2.....	78
5.3	Model 1 and Model 2 Comparison	82
6	Conclusions and Discussion	88

List of Figures

1.1	Illustration of a hair follicle (HF) in telogen (A) and anagen (B). ..	5
1.2	HF cell differentiation diagram. A HF cell differentiation diagram during anagen, with green arrows indicating the feedback controls. B HF cell differentiation diagram with IR exposure: upon IR exposure, all current Mx cells turn into Mx^{IR} cells, after that, Mx^{IR} cells either return to normal Mx cells or start apoptosis.....	8
1.3	An illustration diagram of the symmetric divisions of ORS_a cells in the HF model.	11
2.1	Parameter calibration of the IR induced HF regeneration model. Red lines show simulations results, blue boxes show experimental data. ABC show the simulations / experimental observations with 2 Gy IR, and A'B'C' show simulations / experimental observations with 5.5 Gy IR. Parameters are calibrated to apoptotic Mx cells (AA'), bulb cells (BB') and the percentage of HF length (CC') – modeled as the ratio of current ORS cell number to that in controlled mice.	23
2.2	Figures of p_{ORS}^a (equation 1.4a), p_{Mx}^a (equation 1.4b), and p_{ORS}^p (equation 1.5). Parameters values are taken from the the 2 Gy (AB) and 5.5 Gy (A'B') simulations, respectively (table 2.1). In the plots of p_{ORS}^p (BB'), we take $[ORS_q] = E_q$ so that p_{ORS}^p depends on $[Apop]$ and $[Mx]$	25
2.3	Trajectories of ORS_q with parameters generated by LHS in the PRCC performance.	26
2.4	Simulations of IR induced HF regenerative dynamics. A 2 Gy IR, B 5.5 Gy IR.	28

2.5	Model-data comparison of the IR induced HF regeneration model. Red lines show simulations results with the red y -axis on the right, blue boxes show experimental data with the blue y -axis on the left. AB show the simulations / experimental observations with 2 Gy IR, and A'B' show simulations / experimental observations with 5.5 Gy IR. AA' compare the simulated proliferation Mx cells and the BrdUrd+ Mx cells from experimental observations. BB' show the K5+ Mx cells and simulated ORS-to-Mx flow, with red solid lines showing the percentage of post IR Mx cells that are derived from ORS, and red dashed lines showing the percentage of post IR Mx cells that are derived from Mx cells.....	29
2.6	Sensitivity of the parameters. At each time, only one parameter value changes, ranged from 0.5- to 1.5-fold of the calibrated value. Heatmap shows the number of quiescent ORS cells (ORS_q) at day 20, as a measure of the HF regeneration ability. Simulations are taken from A 0 Gy IR, no radiation, B 2 Gy IR and C 5.5 Gy IR models. In 0 Gy simulations, we use the calibrated values of $\alpha_2, p_2, \alpha_3, p_3$ from the 2 Gy IR data.....	33
2.7	PRCC performed on the A) 2 Gy and B) 5.5 Gy IR models. Parameter values are sampled using LHS, with each parameter uniformly distributed between 0.5 to 1.5 folds of the calibrated value. The first / second index on top of each panel shows the PRCC / p-value of that parameter. Parameters showing large PRCC and small p-value are highlighted by the green boxes. ..	35
2.8	Bifurcation diagrams of the HF regeneration dynamics with respect to the Mx cells' spontaneous apoptosis rate s_3. A , 2 Gy IR system. BCDE , intermediate systems 1-4, F 5.5 Gy IR system. Parameter values of $p_2, p_3, \alpha_2, \alpha_3$ of the systems are provided in table 2.2. Red solid line - stable state, black solid line - unstable state, green dots - stable periodic solution, blue circles - unstable periodic solution. A close up view in D shows a small region of unstable periodic solution. Close up views of the stable (red) and unstable (black) solutions near the anagen HF homeostatic state are shown in F , with the dots indicating periodic solutions removed. ..	37
2.9	Dynamic simulations of the HF cell population system with different Mx spontaneous apoptosis rate values (s_3). A , $s_3 = 0$, no spontaneous apoptosis in Mx cells, HF stays in the stable homeostatic state. B , $s_3 = 0.05$, HF degenerates, followed by small amplitude of periodic dynamics. C , $s_3 = 0.2$, HF fully degenerates.....	39
2.10	Bifurcation diagrams of the HF regeneration dynamics with respect to the apoptosis feedback strength $p = p_2 = p_3$. α_2, α_3 values are taken from the 5.5 Gy IR system. A , $s_3 = 0.05$. B , $s_3 = 0.2$	40
2.11	Simulation of the anagen-to-catagen transition dynamics. A At day 5, s_3 increases linearly, causing the degeneration of the HF epithelium. B ODE simulation results.	41
2.12	s_3, q, γ parameter space (top) and trajectories (bottom) for systems IS3, IS4 and 5.5Gy In parameter space, degenerative trajectories of ORSq are represented as black open dots, other solid dots are regenerative trajectories. The bottom figures are the sample trajectories of ORSq over time.	43

2.13	HF dynamics for IS3, IS4 and 5.5Gy systems with increased s_3 and q. Increase in Mx cells' spontaneous apoptosis rate s_3 and rate q at which IRMx returns to Mx, results in a less abrupt spike in Apop cells compared to the dynamics from Figure 2.4, which can be considered a slight delay in apoptosis. When we compare the trajectories of the 5.5Gy system with $s_3 = 0.05$ and $q = 0.8$ to the dynamics of 5.5G in Figure 2.9 B , we note that the increase in q results in less-oscillating dynamics for all compartments. Here, γ is fixed at the 5.5Gy fitted value.	44
2.14	HF dynamics for IS3, IS4 and 5.5Gy systems with increased s_3 and q and decreased γ. Increase in Mx cells' spontaneous apoptosis rate s_3 and rate q at which IRMx returns to Mx while also reducing the frequency at which IRMx quits interrupted state, γ , results in a less abrupt wave of apoptosis that is subtle yet prolonged over time.	45
4.1	SD Nonhomogeneous Diffusion. Temporal evolution of u on $(0, 2\pi]$, that is the family of functions $\{u_t t = 0, 0.1, 0.2, \dots, 1\}$. A Method 1. B Method 2. C Method 3.	64
4.2	CD Nonhomogeneous Diffusion. Temporal evolution of u on $(0, 2\pi]$, that is the family of functions $\{u_t t = 0, 0.1, 0.2, \dots, 1\}$. Diffusion-related parameters $k_D = 0.05$, $n_D = 15$, $D_{\min} = 0.01$, $D_{\max} = 20$. A Method 1. B Method 2. C Method 3.	65
4.3	SD Nonhomogeneous Diffusion, Constant Production, Linear Degradation. Temporal evolution of u on $(0, 2\pi]$, that is the family of functions $\{u_t t = 0, 0.1, 0.2, \dots, 1\}$. Parameter values $M = 0.2$, degradation $d = 0.5$. A Method 1. B Method 2. C Method 3.	65
4.4	CD Nonhomogeneous Diffusion, Constant Production, Linear Degradation. Temporal evolution of u on $(0, 2\pi]$, that is the family of functions $\{u_t t = 0, 0.1, 0.2, \dots, 1\}$. Parameter values $M = 0.2$, degradation $d = 0.5$. Diffusion-related parameters $k_D = 0.05$, $n_D = 15$, $D_{\min} = 0.01$, $D_{\max} = 20$. A Method 1. B Method 2. C Method 3.	66
4.5	Homogeneous Diffusion, Positive Production Feedback, Linear Degradation. Temporal evolution of u on $(0, 2\pi]$, that is the family of functions $\{u_t t = 0, 0.1, 0.2, \dots, 1\}$. Parameter values $M = 0.2$, degradation $d = 0.5$. Diffusion-related parameters $k_D = 0.05$, $n_D = 15$, $D_{\min} = 0.01$, $D_{\max} = 20$. Production feedback parameters $k_f = 0.15$, $n_f = 15$. A Method 1. B Method 3.	67
4.6	SD Nonhomogeneous Diffusion, Production Feedback, Linear Degradation. Temporal evolution of u on $(0, 2\pi]$, that is the family of functions $\{u_t t = 0, 0.1, 0.2, \dots, 1\}$. Parameter values $M = 0.2$, degradation $d = 0.5$. Production feedback parameters $k_f = 0.15$, $n_f = 15$. A Method 1. B Method 2. C Method 3.	68

4.7	CD Nonhomogeneous Diffusion, Production Feedback, Linear Degradation. Temporal evolution of u on $(0, 2\pi]$, that is the family of functions $\{u_t t = 0, 0.1, 0.2, \dots, 1\}$. Parameter values $M = 0.2$, degradation $d = 0.5$. Diffusion- related parameters $k_D = 0.05$, $n_D = 15$, $D_{\min} = 0.01$, $D_{\max} = 20$. Production feedback parameters $k_f = 0.15$, $n_f = 15$. A Method 1. B Method 2. C Method 3.	69
4.8	Random initial concentration. $u_0 = c_0 + \varepsilon c_0 \chi$, $c_0 = 0.25$, $\varepsilon = 0.5$, $\chi \sim N(0, 1)$	71
5.1	Model 1. Average number of polarization sites heatmaps. (Left) Average (μ) number of polarization sites with percentages in zone 3 cells representing the proportion of successful simulations; all other cells have a success rate of 70% or higher. (Right) Heatmap zone designation.....	75
5.2	Model 1, zone 1 simulation results Sample simulations for parameter pair $(k_D, M) = (0.06, 1)$	76
5.3	Model 1, zone 2 simulation results Sample simulations for parameter pair $(k_D, M) = (0.04, 0.8)$	76
5.4	Model 1, zone 3 simulation results Sample simulations for parameter pair $(k_D, M) = (0.06, 0.6)$	77
5.5	Model 2 Average number of polarization sites heatmaps. Each heatmap is a slice of the parameters space for different values of k_f , with the average value (μ) displayed in each cell. Percentages in zone 3 cells represent the proportion of successful simulations, all other cells have a success rate of 70% or higher.	79
5.6	Model 2, zone 1 simulation samples for low and high k_f. Simulation results for parameter points $(k_D, M, k_f) = (0.05, 0.6, 0.1)$ and $(k_D, M, k_f) = (0.05, 0.8, 0.25)$	80
5.7	Model 2, zone 2 simulation samples for low and high k_f. Simulation results for parameter points $(k_D, M, k_f) = (0.03, 0.8, 0.1)$ and $(k_D, M, k_f) = (0.03, 0.8, 0.25)$	81
5.8	Model 1 average number of polarization sites.	82
5.9	Model 2 average number of polarization sites.	82
5.10	Model 1 coefficient of variation of number of polarization sites.	83
5.11	Model 2 coefficient of variation of number of polarization sites.	83
5.12	Model 1 average height of polarization sites.	84
5.13	Model 2 average height of polarization sites	84
5.14	Model 1 coefficient of variation of height of polarization sites.	85
5.15	Model 2 coefficient of height variation of polarization sites	85
5.16	Model 1 average width of polarization sites.	86
5.17	Model 2 average width of polarization sites	86
5.18	Model 1 coefficient of variation of width of polarization sites.	87
5.19	Model 2 coefficient of variation of width of polarization sites	87

List of Tables

2.1	Parameter values of the HF model calibrated from the IR experimental data.	24
2.2	Parameter values of p_2 , α_2 , p_3 , α_3 in the bifurcation diagrams from figure 2.8. IS stands for “intermediate system”.....	36

Part I

Modeling of Ionizing Radiation
Induced Hair Follicle Regenerative
Dynamics

Chapter 1

Introduction

Hair follicle (HF) research in mathematical biology holds great significance due to its potential applications in the medical field. It may be able to inform cancer research by providing insight on how certain chemotherapy drugs affect hair follicles, or it may help in screening potential compounds for hair growth-promoting or -inhibiting effects which can lead to the creation of novel pharmaceuticals. In this work, we focus on studying the effects of ionic radiation (IR) on the hair follicle growth cycle and its inherent regenerative dynamics.

This first part of the thesis parallels our recent publication [66] and is organized as follows. In this introductory chapter, we first present a brief background of the HF cycle and biology, we also discuss existing modeling literature in the field of hair follicle dynamics. In section 1.2, we develop a HF model following the classic cell differentiation population model framework and based on currently known HF biology from literature. In section 1.3, we derive further parameter constraints from the proposed mathematical model in order to calibrate the model parameters using experimental data. In the results chapter, we first describe the calibration process and present the calibrated parameter values as well as the corresponding simulation results (section 2.1). Then in section 2.2, we apply stability, sensitivity and bifurcation analyses to our system to identify the key model factors that regulate IR-induced HF regeneration or anagen-to-catagen degeneration. We then present

ongoing work to extend our model to reproduce recent experimental findings that test the efficacy of a certain drug on IR-induced hair-loss in 2.3. Lastly, we provide our conclusions and discussion of our work, as well as possible future direction for this project.

1.1 Hair Cycle Biology and Modeling Background

Hair follicles (HFs) are mammalian skin mini-organs which are rich in stem cells. Unlike other tissues and organs, HFs undergo cyclical regeneration throughout the lifetime of an organism. Each HF growth cycle consists of three phases: anagen, the active proliferation phase; catagen, the degeneration phase; and telogen, the quiescent phase. The dynamics of a HF growth cycle are briefly summarized below.

During telogen, a HF rests in its smallest possible size made up of three main compartments: the bulge, hair germ (HG), and the dermal papillae (DP). (figure 1.1A). The bulge is a niche of *bona fide* epithelial stem cells. Underneath the bulge lies the HG, which houses short-lived epithelial progenitors derived from bulge stem cells. The DP marks the bottom of the HF, it contains specialized fibroblasts and serves as the signaling "command center". However, the cells of a telogen HF are relatively biochemically and proliferatively quiescent [1, 3].

During late telogen, DP cells become activated and this marks the onset of anagen. Once activated, DP cells produce various signaling factors, which cooperatively activate proliferation of HF epithelial cells and initiate hair growth. At the beginning of anagen, HG cells give rise to fast-dividing epithelial hair matrix (Mx) cells (figure 1.1B). Mx cells are transient-amplifying (TA) cell that have limited mitotic potential [2] yet show a fast cell cycle time of only 12-13 hours in mice and 24 hours in humans [4, 5]. Meanwhile, the bulge stem cells also become activated and contribute to the formation of the outer root sheath (ORS) which forms the outer epithelial layer of the HF. Mx cells surround the DP and also connect to the lower ORS (figure 1.1B)

As Mx continues to grow, its cells start to differentiate to several types of terminally differentiated (TD) cells, including the hair shaft (HS) and the inner root sheath (IRS). On the other hand, ORS cell proliferation drives the downward HF growth in response to various signaling factors, including *Sonic Hedgehog* (Shh) and *Wingless/Integrated* (Wnt) signaling ligands [16, 17, 40–44]. When a HF grows to a certain length, further downward growth stops, and the HF reaches a dynamic equilibrium that can be maintained for an extended period of time. Despite the relatively constant and stable HF length, its lower compartments (including DP, Mx and lower ORS) remain active, in the way that: 1) cells actively participate in signaling dynamics, and 2) epithelial cells actively divide in response to various signals. In contrast, in the upper HF, as DP and Mx move downward away from the bulge, the signaling source disappears, thus bulge stem cells and upper ORS cells return to a telogen-like quiescence.

Throughout anagen there are only very few apoptotic cells [4, 5]. However, upon transition to early catagen, a coordinated apoptotic wave originates in the Mx and propagates upward through the rest of epithelial HF compartments [7–15]. During catagen, distinct HF compartments produce factors that either activate or inhibit apoptosis [7, 8, 14, 49, 50], as well as factors that terminate pro-proliferation signaling [6, 14]. For example, cells could exchange apoptosis-activating signals, including the *Tumor Necrosis Factor* (Tnf) which contributes to its wave-like propagation [23, 24]. On the other hand, DP cells do not undergo apoptosis, but move upward following the shrinking epithelium until the HF returns to its minimal structure and enters telogen. [14, 15, 25, 27, 45, 46, 59, 60]. Catagen typically lasts for about 2-3 weeks in humans and for 3 days in mice [9, 47, 48].

While the anagen-to-catagen degeneration is irreversible, recent experimental studies revealed that HFs exhibit regenerative dynamics when follicle damage is induced by ionizing radiation (IR) at the mature anagen stage [22, 57]. It is observed that when weak IR is applied, a HF experiences minor length shrinkage then returns to its homeostatic state, compared to strong radiation where a major HF involution accompanied by a high level of apoptosis occurs, yet the HF is still able to regenerate and return to its normal homeostatic

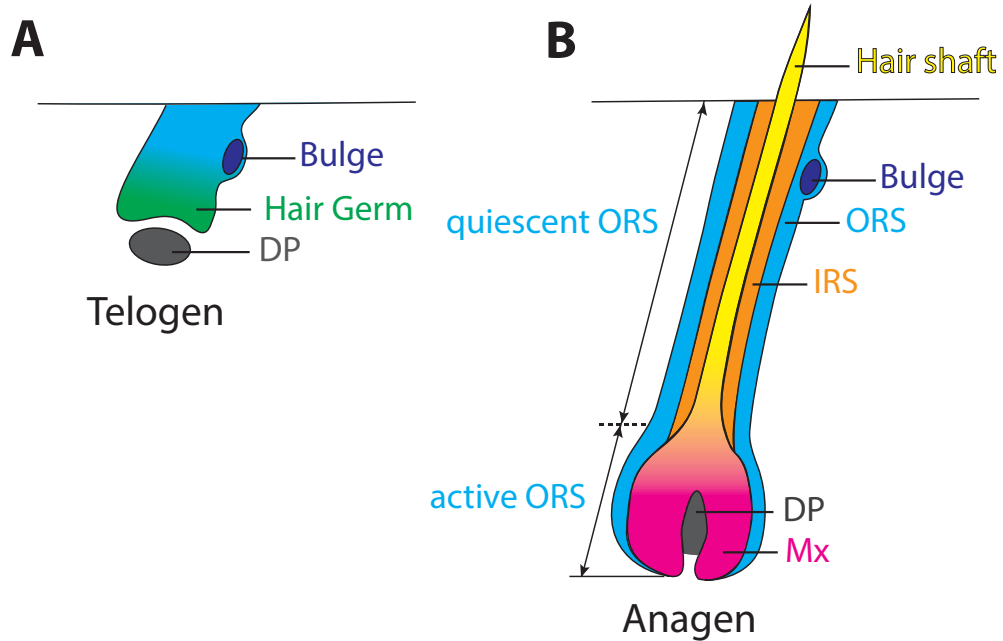


Figure 1.1: *Illustration of a hair follicle (HF) in telogen (A) and anagen (B).*

state. Both regenerative dynamics – after weak and strong IR – are essentially different from the normal progressive, irreversible degeneration during catagen. This gives rise to critical questions related to HF regeneration control: while both degenerative dynamics start with massive apoptosis, why is the degeneration during catagen irreversible while the IR induced degeneration is transient and followed by regeneration? Are the mechanisms underlying these degenerative dynamics essentially different?

In recent years, the HF system has caught the interests of many modeling groups. Automaton models have been adopted to study the HF pattern development [52], [53]. In [52], the authors develop a "follicular automaton" model that simulates transitions between the successive stages of the human HF cycle according to certain stochastic rules. The model is able to produce patterns resembling those of alopecia consistent with the input patterns of mean duration of the anagen phase. In [53] a cellular automaton model of a population of hair follicles is used to study the regenerative behavior of stem cells in mice and rabbits. They demonstrate that regenerative cycling of SCs can be coordinated by diffusible

signals of activator and inhibitor type. Other recent models also attempt to investigate signaling dynamics that control HF growth: in [54] a prototypic feedback-control based ODE model was developed attributing the HF cyclic growth dynamics to feedback interactions between Mx and DP cells. To study the coordinated HF activation dynamics and HF wave propagation behavior, the classic FitzHugh-Nagumo model has been adopted in [55] to reveal the excitable medium property of skin. An activator-inhibitor-based 3-dimensional multi-scale model is developed in [56]. In addition, in recent years more models have been developed to investigate different aspects of HF growth and HF cell fate decisions. For example, the bio-mechanics of the hair shaft fiber protrusion in mammals is recently investigated using a multiscale, finite element modeling framework [58], and a probabilistic Boolean model based on both literature and single cell RNA sequencing data has been developed to study the HF epithelial cell fate regulation mechanisms [64]. We also refer the reader to [51] for a recent review of modeling studies in HF morphogenesis.

Despite the HF system being extensively studied in both experimental and modeling settings, the questions regarding the difference between the catagen degeneration and IR-induced degeneration dynamics, the latter of which is followed by a regeneration, have not to our knowledge been studied. Here we investigate possible mechanisms responsible for a HF's cyclical, degenerative and regenerative dynamics. We develop an ODE model for HF cell population whose main components differentiate according to the network in figure 1.2, we call this a HF cell differentiation population model and we use it to investigate the underlying mechanisms behind the IR-induced regenerative dynamics and compare to those that drive the catagen degenerative dynamics. The focus will be on the instant dynamic behaviors of HF cell populations after a one-time application of IR, these will be compared to the cell population dynamics of nonradiated HF in the anagen-to-catagen phase transition.

1.2 Development of HF ODE Model

Summary of HF Biology and Model Assumptions

While we have provided a HF introduction above, here we briefly expand upon key biological components and mechanisms based on which we develop our model.

- The DP is a cluster of specialized fibroblasts that actively participate in the HF signaling dynamics. It interacts with Mx and *active* ORS (see explanations below for ORS) through various signaling pathways that help regulate Mx and ORS cell division and differentiation. In our model we consider these signals as background regulators and since DP cells do not divide or undergo cell death, we do not explicitly include the DP in the dynamics of our model. Instead, we consider the DP as dynamically stable.
- ORS are epithelial cells mostly derived from bulge stem cells; they form the outer epithelial layer of the HF. At the base of the HF, ORS cells connect with and can differentiate into Mx cells. In our model, we roughly divide ORS into two sub-parts: the dynamic part of ORS at the bottom of the HF, referred to as the *active* ORS (denoted ORS_a), and the rest of the ORS referred to as the *quiescent* ORS (denoted ORS_q), as they are away from the DP signaling center and do not actively divide during most of anagen.
- Mx cells are a group of epithelial transient amplifying cells, they divide fast and give rise to several types of terminally differentiated cells including HS and IRS. When Mx cells run out of dividing potential, they start apoptotic death. During anagen, Mx cells produce signals such as Wnt and Shh that activate ORS cell divisions – in the model we denote these signals as signal B (figure 1.2A).
- During anagen there are only very few apoptotic cells, yet upon the anagen-to-catagen transition, a coordinated apoptotic wave originates in the Mx and propagates upward thanks to the exchange of apoptosis-activating signals, such as Tnf. In our model, cells

undergoing apoptosis are represented as their own population, denoted Apop, which produce signal A that can activate apoptosis in Mx and ORS cells.

The cell differentiation relations and the feedback controls at the bottom part of an anagen HF in our model are illustrated in figure 1.2A.

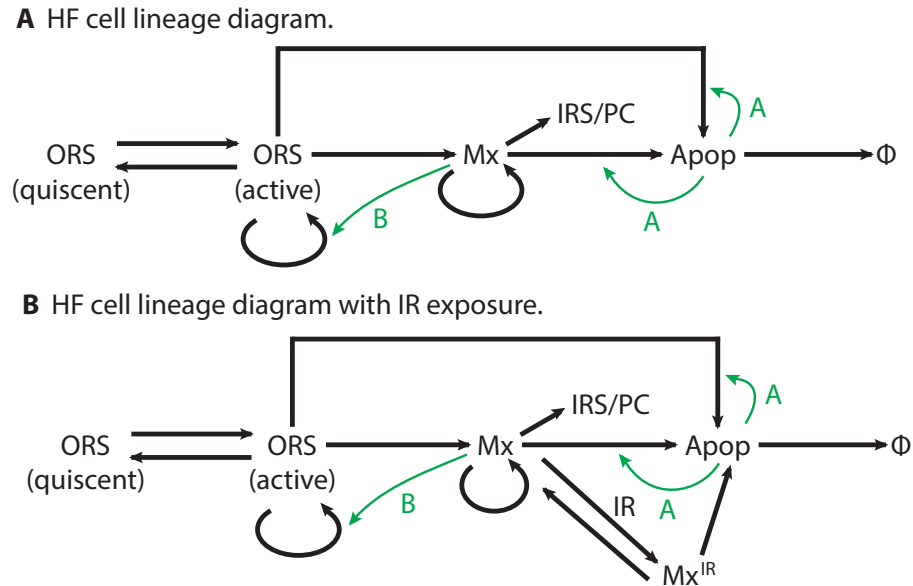


Figure 1.2: HF cell differentiation diagram. *A HF cell differentiation diagram during anagen, with green arrows indicating the feedback controls. B HF cell differentiation diagram with IR exposure: upon IR exposure, all current Mx cells turn into Mx^{IR} cells, after that, Mx^{IR} cells either return to normal Mx cells or start apoptosis.*

HF Cell Differentiation Population Model

We develop a new cell differentiation population model for HF dynamics and regeneration, shown in equation 1.1, following the classic cell lineage ODE modeling framework [18–21]

and described in more detail as follows, as well as in 1.2.

$$\frac{d[\text{ORS}_q]}{dt} = -f([\text{ORS}_a]) \quad (1.1a)$$

$$\frac{d[\text{ORS}_a]}{dt} = f([\text{ORS}_a]) + (2p_{\text{ORS}}^p - 1) \nu_{\text{ORS}}[\text{ORS}_a] \quad (1.1b)$$

$$\frac{d[\text{Mx}]}{dt} = 2p_{\text{ORS}}^d \nu_{\text{ORS}_a}[\text{ORS}_a] + (2p_{\text{Mx}}^p - 1) \nu_{\text{Mx}}[\text{Mx}] \quad (1.1c)$$

$$\frac{d[\text{Apop}]}{dt} = p_{\text{ORS}}^a \nu_{\text{ORS}_a}[\text{ORS}_a] + p_{\text{Mx}}^a \nu_{\text{Mx}}[\text{Mx}] - d[\text{Apop}] \quad (1.1d)$$

where ORS_q and ORS_a denote quiescent and active ORS cells, respectively, Mx denotes hair matrix cells and Apop represents cells undergoing apoptosis. In equations 1.1, $[\cdot]$ denotes the size of a certain type of cell. Since we do not consider spatial information in the HF system, $[\cdot]$ can be equivalently considered as the cell concentration, which is the usual meaning in cell population models.

The expressions p_{ORS}^p , p_{Mx}^p denote the proliferation rates of ORS and Mx cells, respectively; p_{ORS}^d , p_{Mx}^d denote the differentiation rates of ORS and Mx cells, respectively; and p_{ORS}^a , p_{Mx}^a the apoptosis rates of ORS and Mx cells, respectively. Notice that p_{Mx}^d does not explicitly appear in the system, rather it plays an implicit role since we impose that these rate functions should satisfy the following constraints:

$$p_{\text{ORS}}^p + p_{\text{ORS}}^d + p_{\text{ORS}}^a = 1 \quad (1.2a)$$

$$p_{\text{Mx}}^p + p_{\text{Mx}}^d + p_{\text{Mx}}^a = 1 \quad (1.2b)$$

ν_{ORS} , ν_{Mx} are the dividing frequencies of ORS and Mx cells, which relate to the cell cycle time T by the relation $\nu = \ln 2/T$. The average cell cycle time of Mx cells in mice is ~ 12 hours [3,5], in our model we take it as 1 computational time unit, i.e., $T = 1$ is equivalent to 12 hours, and we have $\nu_{\text{Mx}} = \ln 2$. d is the degradation rate of apoptosis cells, that is, the rate at which they exit the system. The function $f([\text{ORS}_a])$ describes the transition between the quiescent ORS and active ORS cells, and we assume the following simple form

of f :

$$f([\text{ORS}_a]) = h_{\text{ORS}} (C_{\text{ORS}} - [\text{ORS}_a]) \quad (1.3)$$

where C_{ORS} stands for the equilibrium size of active ORS cells, and h_{ORS} is the transition rate.

The feedback controls are modeled as follows. Apop cells may produce signals to activate apoptosis in ORS_a and Mx cells, we assume that the apoptosis rates of ORS and Mx cells p_{ORS}^a , p_{Mx}^a depend on the size of Apop cells via the following Hill-function type of controls:

$$p_{\text{ORS}}^a([\text{Apop}]) = p_2 \left[s_2 + \frac{\alpha_2 [\text{Apop}]^{n_2}}{1 + \alpha_2 [\text{Apop}]^{n_2}} \right] \quad (1.4a)$$

$$p_{\text{Mx}}^a([\text{Apop}]) = p_3 \left[s_3 + \frac{\alpha_3 [\text{Apop}]^{n_3}}{1 + \alpha_3 [\text{Apop}]^{n_3}} \right] \quad (1.4b)$$

Mx cells may produce signal A that activates ORS_a cells' proliferation, thus we assume that the ORS_a proliferation rate, p_{ORS}^p depends on the size of Mx cells:

$$p_{\text{ORS}}^p([\text{Mx}], [\text{Apop}], [\text{ORS}_q]) = (1 - p_{\text{ORS}}^a([\text{Apop}])) g([\text{ORS}_q]) p_1 \frac{\alpha_1 [\text{Mx}]^{n_1}}{1 + \alpha_1 [\text{Mx}]^{n_1}} \quad (1.5)$$

where we include another control function g to describe the control of the HF length. The functional forms of equations 1.4ab and 1.5 are illustrated in figure 2.2 using calibrated parameter values (table 2.1). Finally, all probability functions (p 's) in our model are forced to be bounded between 0 and 1.

Derivation of Model Equations 1.1

The formulation of the HF model (equations 1.1) mostly follows the classic cell differentiation population model, which can be found in literature including [18–21]. Below we briefly justify the formulation of equations 1.1 together with the constraints equations 1.2.

Consider equation 1.1b for ORS_a . First, in the case that $f([\text{ORS}_a](t)) > 0$, that is, there is an inflow from ORS_q to ORS_a , during a short time period $[t, t + \Delta t)$, the change in ORS_a

cell number consists of two parts: the part that comes from ORS_q transition (denoted by I_1), and the part that comes from ORS_a cells' proliferation / differentiation / apoptosis (denoted by I_2):

$$[ORS_a](t + \Delta t) - [ORS_a](t) \approx I_1 + I_2$$

It is easy to see that during the short time period $[t, t + \Delta t)$,

$$I_1 \approx f([ORS_a](t))\Delta t$$

ORS_a cell divisions happen at the frequency of ν_{ORS} . The classic cell differentiation population model assumes that on the population level, on average, all cells undergo divisions at the same frequency; or in plain words, all cells divide into two at the frequency ν_{ORS} . In addition, here we adopt the symmetric division assumption, that is, as a cell divides, it gives rise to two daughter cells of the same type. With the symmetric division, if the two daughter cells are of the same type of their dividing mother cell, we refer it to as proliferation; otherwise, if the two daughter cells are of a progeny type of their dividing mother cell, then it is referred to as differentiation. In our follicle model, since we also consider the apoptosis cells as a transient cell type, we adopt the “differentiation” formulation for apoptosis cells, with the difference that instead of dividing into two, one ORS_a cell turns into one apoptosis cell. The dividing relations of ORS_a are summarized in Figure 1.3.

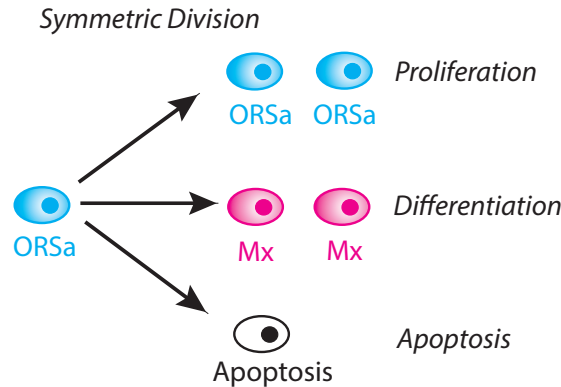


Figure 1.3: *An illustration diagram of the symmetric divisions of ORS_a cells in the HF model.*

From these assumptions, that all ORS_a cells divide at the frequency ν_{ORS} , and each dividing cell either proliferates, differentiates, or undergoes apoptosis, we obtain the constraint equation 1.2a, that is, the portion of proliferating, differentiating and apoptosis ORS_a cells should sum up to 1. Therefore, the net change in ORS_a cell number due to cell division during $[t, t + \Delta t)$ is

$$I_2 \approx (2p_{\text{ORS}}^p - 1) [\text{ORS}_a](t)\Delta t$$

where -1 comes from that all ORS_a cell divide, and $2p_{\text{ORS}}^p$ comes from that p_{ORS}^p of the dividing ORS_a cells proliferate, that is, turn into 2 daughter ORS_a cells. Similarly, it can be derived that after the dividing, there will be $2p_{\text{ORS}}^d[\text{ORS}_a]$ newly differentiated Mx cells from ORS_a , and $p_{\text{ORS}}^a[\text{ORS}_a]$ apoptosis cells from ORS_a – again notice that unlike the proliferating and differentiating cells, we assume that one ORS_a cell turns into only one apoptosis cell. Therefore we obtain

$$\begin{aligned} [\text{ORS}_a](t + \Delta t) - [\text{ORS}_a](t) &\approx I_1 + I_2 \\ &= f([\text{ORS}_a](t))\Delta t + (2p_{\text{ORS}}^p(t) - 1) \nu_{\text{ORS}}[\text{ORS}_a](t)\Delta t \end{aligned}$$

which gives equation 1.1b:

$$\begin{aligned} \frac{d[\text{ORS}_a]}{dt} &= \lim_{\Delta t \rightarrow 0} \frac{[\text{ORS}_a](t + \Delta t) - [\text{ORS}_a](t)}{\Delta t} \\ &= f([\text{ORS}_a]) + (2p_{\text{ORS}}^p - 1) \nu_{\text{ORS}}[\text{ORS}_a] \end{aligned}$$

In the case that $f([\text{ORS}_a](t)) < 0$, that is, there is an outflow from ORS_a to ORS_q , we assume that $|f([\text{ORS}_a](t))| \sim O(1)$. In addition, since generally speaking, the ORS_a -to- ORS_q transition and ORS_a cell divisions happen at different frequencies, we may roughly consider that in a short time period $[t, t + \Delta t)$, the ORS_a -to- ORS_q transition and the ORS_a cell division happen successively. That is, if the transition happens in the interval $[t, t + \Delta t)$, then the ORS_a cells divide at $t + \Delta t$. Therefore, the ORS_a cell number right before the cell

division is

$$\lim_{\tau \rightarrow (t+\Delta t)^-} [\text{ORS}_a](\tau) \approx [\text{ORS}_a](t) + f([\text{ORS}_a](t))\Delta t$$

then at $t + \Delta t$, ORS_a cell divisions will lead to a change in the ORS_a cell number as

$$(2p_{\text{ORS}}^p(t) - 1) ([\text{ORS}_a](t) + f([\text{ORS}_a](t))\Delta t)$$

Notice that the constraint equation 1.2a still holds as we are only considering the dividing ORS_a cells, and the ORS_a to ORS_q transition mostly happens at a different frequency and we have included the transition term inside the current ORS_a cell number. Therefore, we get the estimate

$$\begin{aligned} & [\text{ORS}_a](t + \Delta t) - [\text{ORS}_a](t) \approx \\ & [f([\text{ORS}_a](t)) + (2p_{\text{ORS}}^p(t) - 1) \nu_{\text{ORS}} ([\text{ORS}_a](t) + f([\text{ORS}_a](t))\Delta t)] \Delta t \end{aligned}$$

Under the assumption of $|f([\text{ORS}_a](t))| \sim O(1)$, we have

$$\frac{[\text{ORS}_a](t + \Delta t) - [\text{ORS}_a](t)}{\Delta t} \approx f([\text{ORS}_a](t)) + (2p_{\text{ORS}}^p - 1) \nu_{\text{ORS}} [\text{ORS}_a] + o(\Delta t)$$

Let $\Delta t \rightarrow 0$, again we get equation 1.1b:

$$\frac{d[\text{ORS}_a]}{dt} = f([\text{ORS}_a]) + (2p_{\text{ORS}}^p - 1) \nu_{\text{ORS}} [\text{ORS}_a]$$

We point out that though we could not rigorously prove it, but the assumption $|f([\text{ORS}_a](t))| \sim O(1)$ mostly holds true when $f([\text{ORS}_a](t)) < 0$ in our system. Notice that $f([\text{ORS}_a](t)) < 0$, or equivalently, the ORS_a -to- ORS_q transition, only happens when the ORS_a cell number ($[\text{ORS}_a]$) exceeds the equilibrium size (C_{ORS}). To break the constraint $|f([\text{ORS}_a](t))| \sim O(1)$, it needs a very large ORS_a cell number, which is rarely the case in

either a controlled system or a radiated system. This can also be seen from our simulation results (for example, figure 2.4).

We have shown that in either ORS_a inflow or outflow case, equation 1.1b holds, though in the outflow case, some condition applies. We also point out that if we consider the size of the entire ORS as $[\text{ORS}_q] + [\text{ORS}_a]$, the only change in the cell number comes from cell proliferation, differentiation and apoptosis, which can be obtained by adding up equations 1.1a and b:

$$\frac{d[\text{ORS}_q]}{dt} + \frac{d[\text{ORS}_a]}{dt} = (2p_{\text{ORS}}^p - 1) \nu_{\text{ORS}}[\text{ORS}_a]$$

Analogously, equation 1.1cd for Mx and apoptosis cells can be derived in a similar way. In 1.1c, $(2p_{\text{Mx}}^p - 1) \nu_{\text{Mx}}[\text{Mx}]$ comes from the dividing of Mx cells, and $2p_{\text{ORS}}^d \nu_{\text{ORS}_a}[\text{ORS}_a]$ comes from the differentiating ORS_a cells, with the constraint equation 1.2b for dividing Mx cells. In 1.1d, $p_{\text{ORS}}^a \nu_{\text{ORS}_a}[\text{ORS}_a]$ comes from the apoptosis ORS_a cells, $p_{\text{Mx}}^a \nu_{\text{Mx}}[\text{Mx}]$ comes from the apoptosis Mx cells, and apoptosis cells die, or say, leave the system at the rate d , which leads to the $-d[\text{Apop}]$ term.

On the control function g HFs grow during the early stage of anagen until they reach their maximum length, then they stop further downward growth but keep producing hair shaft. Up to date, the mechanisms that determine the HFs' maximum length and maintain their homeostasis are still unclear. An intuitive guess would be that there might be some signal X produced by Mx cells that inhibits ORS cell proliferation, so that when the HF reaches its maximum size, the ORS cell proliferation is greatly inhibited by this signal, allowing the HF to stay at that length. However, to our knowledge, no such signal X has been identified. Due to the lack of further evidence on the HF length control mechanism, in our model, we include this control as a function g in the ORS cell proliferation rate p_{ORS}^p . Moreover, we would like to emphasize that the feedback mechanism from Mx to ORS cells through signal A serves to activate instead of to inhibit ORS cell proliferation.

We use the size of quiescent ORS as a rough measure of the HF length, and phenomenologically model the length control in the following way:

$$g([\text{ORS}_q]) = \frac{E_q}{[\text{ORS}_q]} \quad (1.6)$$

where E_q represents the equilibrium size of quiescent ORS cells $[\text{ORS}_q]$. We point out that without the HF length control, i.e. $g \equiv 1$, equations 1.1bcd will form a closed system of $[\text{ORS}_a]$, $[\text{Mx}]$, $[\text{Apop}]$, while $[\text{ORS}_q]$ can be considered as an output of the subsystem (equations 1.1bcd) by equation 1.1a. In this case, it is easy to see the following:

Lemma 1. *If $(\overline{[\text{ORS}_q]}, \overline{[\text{ORS}_a]}, \overline{[\text{Mx}]}, \overline{[\text{Apop}]})$ is an equilibrium state of the system 1.1 with $g \equiv 1$, then for any c such that $\overline{[\text{ORS}_q]} + c \geq 0$, $(\overline{[\text{ORS}_q]} + c, \overline{[\text{ORS}_a]}, \overline{[\text{Mx}]}, \overline{[\text{Apop}]})$ is also an equilibrium state.*

Proof. With $g \equiv 1$, the equation system 1.1 can be written as

$$\frac{d[\text{ORS}_q]}{dt} = \phi_1([\text{ORS}_a]) \quad (1.7a)$$

$$\frac{d[\text{ORS}_a]}{dt} = \phi_2([\text{ORS}_a], [\text{Mx}], [\text{Apop}]) \quad (1.7b)$$

$$\frac{d[\text{Mx}]}{dt} = \phi_3([\text{ORS}_a], [\text{Mx}], [\text{Apop}]) \quad (1.7c)$$

$$\frac{d[\text{Apop}]}{dt} = \phi_4([\text{ORS}_a], [\text{Mx}], [\text{Apop}]) \quad (1.7d)$$

If $(\overline{[\text{ORS}_q]}, \overline{[\text{ORS}_a]}, \overline{[\text{Mx}]}, \overline{[\text{Apop}]})$ is an equilibrium state of the system 1.7, then

$$\Phi(\overline{[\text{ORS}_q]}, \overline{[\text{ORS}_a]}, \overline{[\text{Mx}]}, \overline{[\text{Apop}]}) = \vec{0} \quad (1.8)$$

where $\Phi = (\phi_1, \phi_2, \phi_3, \phi_4)^T$. Since the ϕ_i , $i = 1, \dots, 4$ do not depend on $[\text{ORS}_q]$, we can write equation 1.8 as

$$\Phi(\overline{[\text{ORS}_a]}, \overline{[\text{Mx}]}, \overline{[\text{Apop}]}) = \vec{0}$$

Therefore, for any constant c such that $\overline{[\text{ORS}_q]} + c \geq 0$, we have

$$\Phi(\overline{[\text{ORS}_q]} + c, \overline{[\text{ORS}_a]}, \overline{[\text{Mx}]}, \overline{[\text{Apop}]}) = \Phi(\overline{[\text{ORS}_a]}, \overline{[\text{Mx}]}, \overline{[\text{Apop}]}) = 0$$

which indicates that $(\overline{[\text{ORS}_q]} + c, \overline{[\text{ORS}_a]}, \overline{[\text{Mx}]}, \overline{[\text{Apop}]})$ is also an equilibrium state of the system 1.7. \square

The above Lemma indicates that if $g \equiv 1$, then any constant value of the ORS_q compartment size is an equilibrium of the HF model. This violates the biological fact that the homeostatic HF length (roughly represented by size of $[\text{ORS}_q]$) during anagen is well determined. This shows that a growth control mechanism that possibly depends on the HF length, or equivalently, the size of ORS_q in our model is necessary for the HF system.

Modeling IR Effect on HF Regeneration

In the experimental study from [22], different strength of IR (2 Gy and 5.5Gy) is applied to mouse HFs, and the effects are observed and analyzed in the following days. In [22] (also see figure 2.1), proliferative Mx cells are identified as BrdUrd⁺ Mx cells. There are no BrdUrd⁺ Mx cells detected at 6 hours post-exposure of either 2 Gy or 5.5 Gy IR, effectively causing a pause in the Mx cellular processes, thus we can interpret this as Mx cells entirely being affected by IR as follows. We assume that during $t < 0$, the system 1.1 is at equilibrium, corresponding to the homeostatic state in non-radiated, or controlled, mice HFs. At $t = 0$, we introduce in a new quantity Mx^{IR} denoting the Mx cells that pause their cellular processes due to IR exposure, and we assume that at $t = 0$, all current Mx cells become Mx^{IR} , i.e.,

$$\text{Simulated IR exposure: } [\text{Mx}^{IR}](0) = \lim_{t \rightarrow 0^-} [\text{Mx}](t), \quad [\text{Mx}](0) = 0$$

Also according to [22], after IR exposure, Mx cells restart their cellular processes including both cell proliferation and apoptosis, and there is an inflow of ORS cells into the hair bulb to replenish the Mx cell population. Thus, we assume that after the simulated IR exposure,

Mx^{IR} cells can either return to normal Mx cells at a rate of q , or they can start apoptosis at the rate of $1 - q$. The dynamics of the Mx^{IR} are described by the following equations, and illustrated in figure 1.2B.

$$\frac{d[Mx^{IR}]}{dt} = -\gamma[Mx^{IR}] \quad (1.9a)$$

$$\frac{d[Mx]}{dt} = \gamma q[Mx^{IR}] + 2p_{ORS}^d \nu_{ORS_a}[ORS_a] + (2p_{Mx}^p - 1) \nu_{Mx}[Mx] \quad (1.9b)$$

$$\frac{d[Apop]}{dt} = \gamma(1 - q)[Mx^{IR}] + p_{ORS}^a \nu_{ORS_a}[ORS_a] + p_{Mx}^a \nu_{Mx}[Mx] - d[Apop] \quad (1.9c)$$

γ is the “degradation” rate of Mx^{IR} , which can be understood as the rate at which the Mx^{IR} cells quit their interrupted state, and equations 1.9bc are modified from equations 1.1cd to include the post-radiation transitions of Mx^{IR} just described. That is, return to normal ($\gamma q[Mx^{IR}]$ in equation 1.9b), or start apoptosis ($\gamma(1 - q)[Mx^{IR}]$ in equation 1.9c).

Modeling of Mx Lineage Tracing after IR

In the IR simulations, we are also interested in how much the ORS-to-Mx differentiation contributes to the Mx regeneration, therefore we would like to inspect the post-radiation Mx lineage tracing. At $t = 0$, all current Mx cells turn into Mx^{IR} . For $t > 0$, we mark the Mx cells derived from ORS cells and their progeny cells as Mx+, and those that recover from Mx^{IR} as Mx-. The dynamics of [Mx] in equation 1.9 are further decomposed into the following two equations:

$$\frac{d[Mx+]}{dt} = 2p_{ORS}^d \nu_{ORS_a}[ORS_a] + (2p_{Mx}^p - 1) \nu_{Mx}[Mx+] \quad (1.10a)$$

$$\frac{d[Mx-]}{dt} = \gamma q[Mx^{IR}] + (2p_{Mx}^p - 1) \nu_{Mx}[Mx-] \quad (1.10b)$$

where $[Mx+] + [Mx-] = [Mx]$ gives the total Mx cell population.

1.3 Model Parameters

In this section, we derive additional constraints using relations obtained from the steady state of system 1.1 which corresponds to the non-radiated, or control case in mice from experimental study [22]. We then summarize the main findings in the same work, and use their experimental data to calibrate the parameters in our HF model. Lastly, we show simulation results using the parameter set obtained from the calibration.

Information from Control Case

In the control case, or equivalently, 0 Gy IR, apoptosis is hardly detected during anagen until the initiation of catagen. Therefore, $[\text{Apop}] \equiv 0$, $p_{\text{ORS}}^a = p_{\text{Mx}}^a = 0$ in the system without IR exposure (equations 1.1), and equations 1.4 give

$$p_{\text{ORS}}^a([\text{Apop}] = 0) = p_2 s_2 = 0, \quad p_{\text{Mx}}^a([\text{Apop}] = 0) = p_3 s_3 = 0$$

Since p_2 , p_3 cannot be zero otherwise the feedback controls from Apop to Mx and ORS_a will be trivially zero (equations 1.4), the above relations indicate that $s_2 = s_3 = 0$. That is, the spontaneous apoptosis rates in Mx and ORS cells during anagen are both zero.

Without radiation exposure, HF growth should stay homeostatic during anagen, thus the system 1.1 should stay in its equilibrium state. We have discussed above that at the equilibrium state, $[\text{Apop}] = 0$. Furthermore, we use data from [22] to estimate the equilibrium size of Mx, denoted E_{Mx} , by extracting the control average value of Mx, which gives $E_{\text{Mx}} \approx 128$. There is no direct clue from the data about the equilibrium values of $[\text{ORS}_q]$ and $[\text{ORS}_a]$, yet from system 1.1,

$$\frac{d[\text{ORS}_q]}{dt} = f([\text{ORS}_a]) = h_{\text{ORS}} (C_{\text{ORS}} - [\text{ORS}_a]) = 0$$

thus we should have $[\text{ORS}_a] = C_{\text{ORS}}$. Finally, considering the length control function g (equation 1.2), we take $[\text{ORS}_q] = E_q$ as the equilibrium value. Therefore, we obtain the

equilibrium state in HF growth dynamics system 1.1:

$$(\overline{[\text{ORS}_q]}, \overline{[\text{ORS}_a]}, \overline{[\text{Mx}]}, \overline{[\text{Apop}]}) = (E_q, C_{\text{ORS}}, E_{\text{Mx}}, 0)$$

where $E_{\text{Mx}} \approx 128$, while the values of E_q and C_{ORS} are to be determined.

Two other constraints for the parameters can be obtained by the steady state of the system 1.1. At the steady state, equation 1.1bc can be reduced to

$$\begin{aligned} \frac{d[\text{ORS}_a]}{dt} &= (2p_{\text{ORS}}^p - 1) \nu_{\text{ORS}}[\text{ORS}_a] = 0 \\ \frac{d[\text{Mx}]}{dt} &= 2p_{\text{ORS}}^d \nu_{\text{ORS}}[\text{ORS}_a] + (2p_{\text{Mx}}^p - 1) \nu_{\text{Mx}}[\text{Mx}] = 0 \end{aligned}$$

with

$$p_{\text{ORS}}^p = p_1 \frac{\alpha_1 E_{\text{Mx}}^{n_1}}{1 + \alpha_1 E_{\text{Mx}}^{n_1}}, \quad p_{\text{ORS}}^p + p_{\text{ORS}}^d = 1, \quad p_{\text{Mx}}^p + p_{\text{Mx}}^d = 1$$

From the above relations, we obtain the following constraints at the equilibrium:

$$p_1 \frac{\alpha_1 E_{\text{Mx}}^{n_1}}{1 + \alpha_1 E_{\text{Mx}}^{n_1}} = \frac{1}{2} \tag{1.11a}$$

$$p_{\text{Mx}}^p = \frac{1}{2} \left(1 - \frac{\nu_{\text{ORS}} C_{\text{ORS}}}{\nu_{\text{Mx}} E_{\text{Mx}}} \right) \in \left[0, \frac{1}{2} \right] \tag{1.11b}$$

Notice that we did not specify any conditions between the proliferation and differentiation rates of Mx cells, i.e., $p_{\text{Mx}}^p, p_{\text{Mx}}^d$ in equation 1.2b. Published studies suggest that Mx cells mostly respond to both proliferation (including Fgf7/10) and differentiation signals (including Bmp and its antagonist Noggin) sent from the DP [1, 2, 26–38], and that Bmp ligands might have a longer effective range than Fgf and Noggin ligands, which results in an upward-oriented pro-proliferation-to-pro-differentiation signaling gradient [30]. Since DP is relatively stable, we assume that such a pro-proliferation-to-pro-differentiation signaling gradient imposed on Mx is also stable, from which we may assume that $p_{\text{Mx}}^p/p_{\text{Mx}}^d$ keeps the same ratio during anagen. Therefore, we take the value from equation 1.11b as r , and assume the following

relations for Mx cells:

$$r = \frac{1}{2} \left(1 - \frac{\nu_{\text{ORS}} C_{\text{ORS}}}{\nu_{\text{Mx}} E_{\text{Mx}}} \right), \quad p_{\text{Mx}}^p = r(1 - p_{\text{Mx}}^a), \quad p_{\text{Mx}}^d = (1 - r)(1 - p_{\text{Mx}}^a) \quad (1.12)$$

Finally, we point out that studies also show that there are other dynamic supplementary resources for Bmp ligands that promote Mx cells differentiation, which may include ORS and another group of transient amplifying cells derived directly from Mx, called precortex [30,39]. However, considering that DP serves as the main source of Mx cell proliferation and differentiation signals, for now we do not consider these additional sources in our model and adopt the simplified assumption (equations 1.12).

With all considerations described above, we first calibrate our model parameters to data from [22] and summarize the major discoveries about IR induced HF regenerative dynamics and list them below. In the results chapter, we present discuss in more detail how the parameters are calibrated and present simulation results.

Summary of Major Discoveries from IR Experimental Results

- IR is applied to two distinct groups of mice; one is applied IR of strength 2 Gy, and the other a strength of 5.5 Gy. Through staining techniques, researchers from [22] are able to quantify the number of proliferative cells, the percent of apoptotic cells in the matrix, the HF length, as well as the tracking of Mx cells lineage post-radiation.
- *Apoptotic Mx cells.* With either 2 or 5.5 Gy IR, apoptosis is detected in Mx cells shortly after exposure during (0 - 6 h) (referred to as TUNEL⁺ Mx cells in [22]). With 2 Gy IR, the number of apoptotic Mx cells returns to zero at ~ 24 h; with 5.5 Gy IR, it takes until ~ 72 h for the number of apoptotic Mx cells to return to zero. See plots in figure 2.1AA' regenerated from data from [22].
- *Mx cells.* With 2 Gy IR, the number of Mx cells decreases to about half the initial number at ~ 24 h, then returns to the equilibrium level at ~ 72 h; with 5.5 Gy IR, the number of Mx cells continues to decrease until ~ 72 h, then increases from \sim

72 h to day 7, however catagen starts at day 7 before Mx is fully regenerated (figure 2.1BB'). Moreover, In both 2 Gy and 5.5 Gy IR, no proliferating Mx cells (referred to as BrdUrd⁺ in [22]) are detected at 6 h. After that, with 2 Gy IR, the number of proliferating Mx cells increases significantly until ~ 48 h after which point it remains at more or less the same level until day 7; with 5.5 Gy IR, the number of proliferating Mx cells shows a slightly recovery and stays at a low level during 6 - 72 h, then it returns to zero at 72 h, followed by a second recovery attempt until day 7, referred to as *the second regeneration attempt* (figure 2.5BB').

- *HF length.* With 2 Gy IR, there is a small decrease in the HF length with minimum occurring at ~ 48 h before returning to a normal level; with 5.5 Gy IR, the HF shrinks significantly to about half original length by 72 h then returns to normal by day 7 (figure 2.1CC'). In both cases the HF length is fully regenerated by day 7, when catagen starts.
- *ORS to Mx flow.* In normal HFs, keratin 5 (K5+) is present exclusively in cells in the basal area of the hair bulb. With 2 Gy or 5.5 Gy IR, K5+ is found in cells upwards of the basal area, indicating that these cells contribute to the bulb regeneration.

Chapter 2

Results

2.1 Parameter Calibration

In our model system, we classify some parameters as closely related to IR strength and apoptosis signaling dynamics. Therefore, we divide the parameters into the two groups:

$$\text{Group 1: } \quad \gamma, q, \alpha_2, \alpha_3, p_2, p_3, s_2, s_3, n_2, n_3, d \quad (2.1a)$$

$$\text{Group 2: } \quad h_{\text{ORS}}, C_{\text{ORS}}, \nu_{\text{ORS}}, \nu_{\text{Mx}}, p_1, \alpha_1, n_1, E_q, E_{\text{Mx}} \quad (2.1b)$$

Group 1 parameters either directly relate to IR (γ, q) or they participate in the apoptosis signaling pathway ($\alpha_2, \alpha_3, p_2, p_3, s_2, s_3, n_2, n_3, d$). Group 2 includes all other parameters. The parameter $\nu_{\text{Mx}} = \ln 2$, and we have determined $s_2 = s_3 = 0$, $E_{\text{Mx}} = 128$ as discussed in section 1.3. We further assume that the Hill exponents $n_1 = n_2 = n_3 = 2$ for simplicity. For other parameters, we impose that group 2 parameters should have the same value despite of IR strength, while group 1 parameters can be selectively different depending on IR strength.

We first tried to use the least square method by creating an optimization problem using Matlab functions `fcn2optimexpr` and `optimproblem`. The data to be fitted are 2 Gy and 5.5 Gy data of apoptosis Mx cells (figure 2.1AA' blue boxes), bulb cells (figure 2.1BB' blue boxes) and the percentage of HF length (figure 2.1CC' blue boxes), at time points

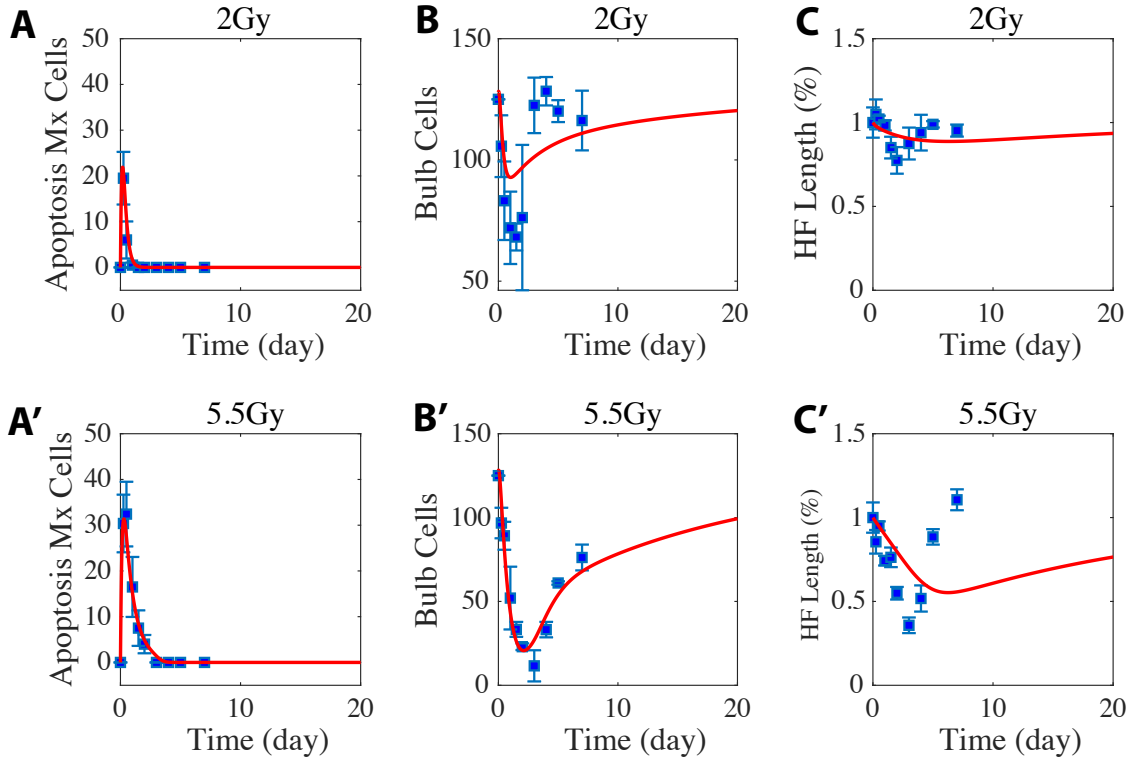


Figure 2.1: *Parameter calibration of the IR induced HF regeneration model.* Red lines show simulations results, blue boxes show experimental data. **ABC** show the simulations / experimental observations with 2 Gy IR, and **A'B'C'** show simulations / experimental observations with 5.5 Gy IR. Parameters are calibrated to apoptotic Mx cells (**AA'**), bulb cells (**BB'**) and the percentage of HF length (**CC'**) – modeled as the ratio of current ORS cell number to that in controlled mice.

hour 0, 6, 12, day 1, 1.5, 2, 3, 4, 5 and 7. We use the same parameters from group 2 (2.1b) for both 2 Gy and 5.5 Gy data, while parameters from group 1 (2.1b) are allowed to be different to fit separately to the 2 Gy and 5.5 Gy data. Initial guesses of the parameter values are randomly chosen. Unfortunately, the better results from the least square method give parameters that predict biologically unrealistic dynamics when observing the long-term behavior after the last experimental observation at time point (day 7): for example, some of the results do not show the HF regeneration observed in the 5.5 Gy IR experiments, or some others show large amplitude of oscillations in HF length. Therefore, instead of seeking the optimal fitted parameter values, we chose a set of parameter values that numerically matches

the experimental data to a reasonable extent, while remaining biologically meaningful and captures the major characteristic behaviors in IR induced HF regeneration.

The calibrated parameter values are given in table 2.1, where altogether we have 18 free variables, with p_2 , p_3 , α_2 , α_3 , q having separate values for 2 Gy and 5.5 Gy data. s_2 , s_3 , ν_{Mx} , E_{Mx} are pre-determined from literature thus are not included in these 18 free variables. The simulation results with the calibrated parameter values are shown in figure 2.1AA'BB'CC' by the red solid lines, in comparison to the IR experiment data shown by the blue boxes.

Table 2.1: *Parameter values of the HF model calibrated from the IR experimental data.*

Parameters	Values	
s_2	0	
s_3	0	
ν_{Mx}	$\ln 2$	
E_{Mx}	128	
h_{ORS}	2.2532	
ν_{ORS}	0.21907	
d	2.0755	
C_{ORS}	27.844	
ORS_{max}	108.8424	
γ	3.5262	
p_1	0.99507	
p_2	0.059416 (2 Gy)	0.9985 (5.5 Gy)
p_3	1.5273×10^{-4} (2 Gy)	0.99977 (5.5 Gy)
α_1	6.1642×10^{-5}	
α_2	0.071299 (2 Gy)	0.022659 (5.5 Gy)
α_3	0.0032523 (2 Gy)	0.042646 (5.5 Gy)
q	0.64089 (2 Gy)	0.64679 (5.5 Gy)

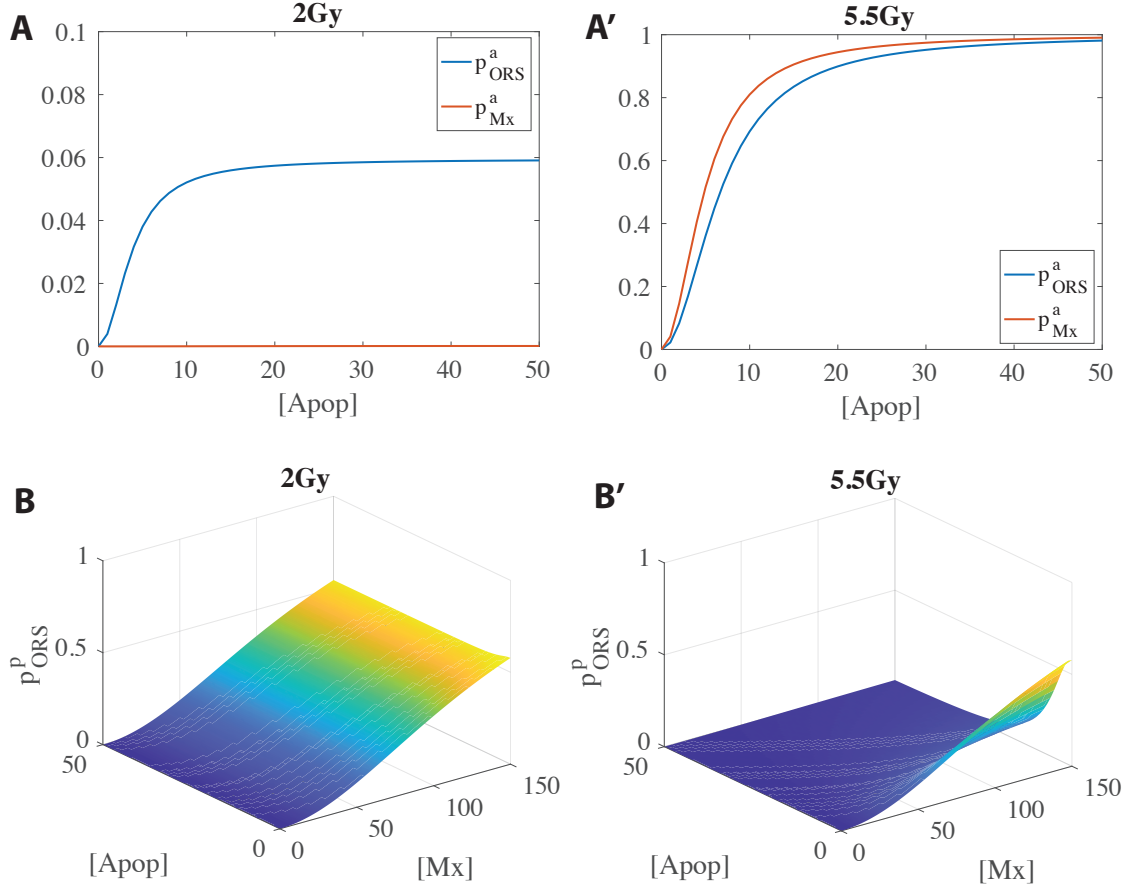


Figure 2.2: Figures of p_{ORS}^a (equation 1.4a), p_{Mx}^a (equation 1.4b), and p_{ORS}^p (equation 1.5). Parameters values are taken from the the 2 Gy (AB) and 5.5 Gy (A'B') simulations, respectively (table 2.1). In the plots of p_{ORS}^p (BB'), we take $[\text{ORS}_q] = E_q$ so that p_{ORS}^p depends on $[\text{Apop}]$ and $[\text{Mx}]$.

Comparing the simulation results with the IR experimental data, we find that apoptotic Mx cell number and bulb cell number show good agreement with the data (figure 2.1AA'BB'). On the other hand, there is some difference between the simulation and data of the HF length percentage. This is mostly because of the following two reasons. First, our model does not have spatial information, and the HF length is approximated as the ratio of the current number of ORS cells in the radiation systems to the number of ORS cells in the control case. Second, it is possible that the simple assumption of the HF length control function

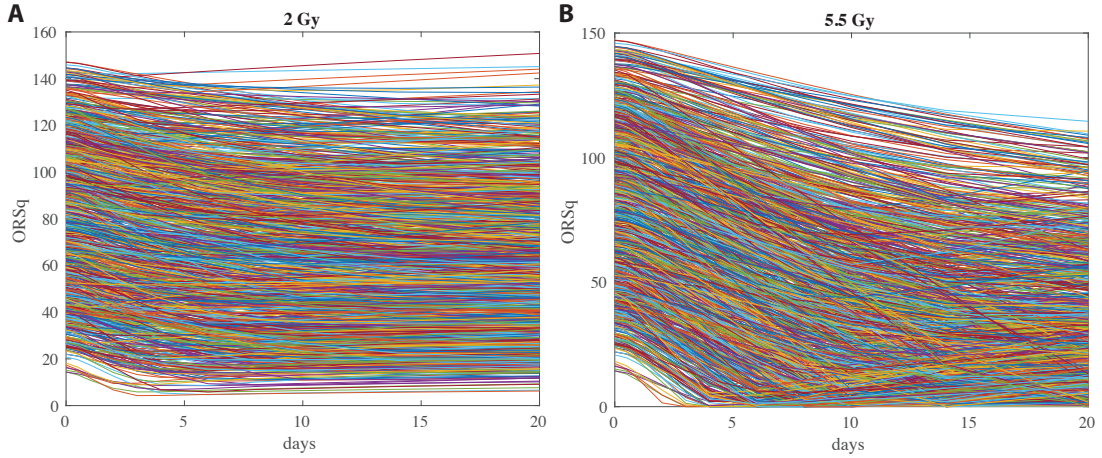


Figure 2.3: *Trajectories of ORS_q with parameters generated by LHS in the PRCC performance.*

g (equation 1.2) may lead to a slow HF regeneration, compared to the real biological HF length control mechanism. Considering these two model simplifications and that the calibrated results still capture the characteristics of the HF length regeneration dynamics, we accept this set of parameter values. From both the IR data and simulation results in figure 2.1AA'BB'CC', we see that in either 2 Gy or 5.5 Gy case, IR induces massive apoptosis but only during the early stage. 5.5 Gy IR causes significant decrease in both bulb cells and the HF length in comparison to 2 Gy IR, yet in both cases, the HF is able to return to its homeostatic state, though the simulation predicts longer time for HF length recovery.

Finally, we also point out that another dataset at day 10 post-IR is presented in [22], which clearly shows drops in both the HF length and Mx cell numbers, indicating that the HF has entered the degenerating catagen phase. Since our model does not count for the dynamics of the whole HF growth cycle, we ignore this day 10 catagen dataset as our model cannot predict an automatic onset of catagen. We also extend most of our simulations to day 20 to better assess the long-term regenerative behavior, since, as is shown in figure 2.1A'B'C', in the 5.5 Gy simulations it takes a longer time than 7 days for the HF to fully regenerate to a pre-IR level – this also seems to be true for the 5.5 Gy IR experiment; indeed,

catagen begins after day 7 before the Mx can fully return to its pre-IR level (figure 1E from [22]).

Simulation Results

In figure 2.4, we show the simulated dynamics of each HF compartment after 2 Gy or 5.5 Gy IR (figure 2.4) which show regenerative patterns. In both cases, after IR exposure, a wave of apoptosis cells is triggered but quickly goes away (black solid lines). The radiated Mx cells (Mx^{IR}) also quickly disappear from the system (magenta dashed lines); the regular Mx compartment (magenta solid lines) quickly regenerates in the 2 Gy IR simulation (2.4A), while in the 5.5 Gy IR simulation, it first regenerates quickly, but is then followed by another drop, then regenerates again (2.4B). For ORS, we notice that the ORS_a compartment mostly maintains its size despite the strength of IR (blue solid lines); while ORS_q relatively maintains its regular size in the 2 Gy IR simulation (2.4A), indicating little change in the HF length, yet in the 5.5 Gy IR simulation, a clear drop in the ORS_q size is observed, followed by a slow regeneration, which indicates an early degenerating HF followed by a regeneration. Comparing the 2 Gy vs. 5.5 Gy IR simulations, we find that while all HF compartments regenerate relatively quickly in the 2 Gy IR simulations, it takes much longer to regenerate in the 5.5 Gy IR simulations, especially for Mx and ORS_q . The slow regeneration of the Mx compartment predicted from our 5.5 Gy IR simulations seems to coincide with that shown by the 5.5 Gy IR experiment (figure 1E from [22]), although the experiment shows a faster regeneration in the HF length.

We now show our model results when simulating Mx proliferation and the ORS-to-Mx differentiation dynamics and compare to the experimental data. We mention that we did not use this data in our parameter calibration, since, as we will explain below, the simulated terms are only approximations to what is measured in experiments.

We first compare the proliferating Mx cells (defined as $\nu_{Mx} p_{Mx}^p [Mx]$) to the BrdUrd+ Mx cell data (figure 2.5AA'). In the experimental 2 Gy IR case, BrdUrd+ Mx data indicates that Mx cells return to proliferation soon after radiation, while in the 5.5 Gy IR case, two

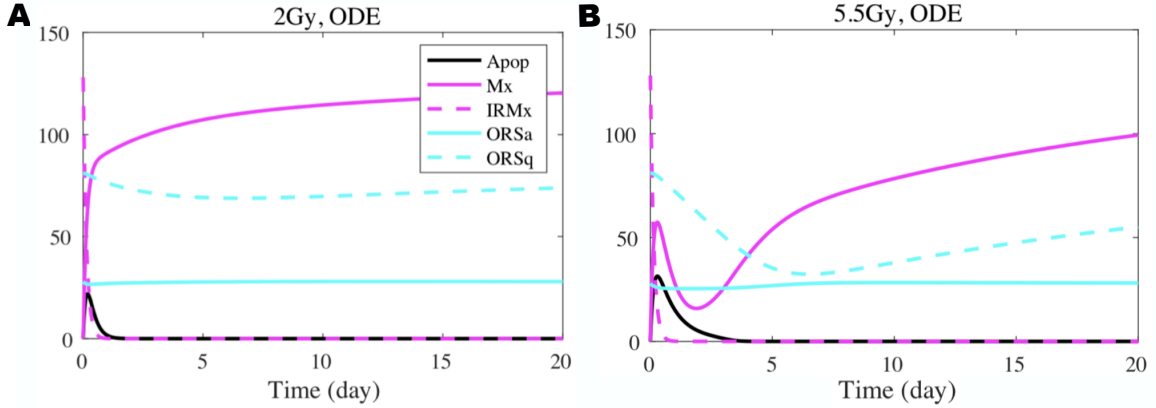


Figure 2.4: *Simulations of IR induced HF regenerative dynamics. A 2 Gy IR, B 5.5 Gy IR.*

proliferation restoration attempts can be observed, both of which stay at low levels. The increase in proliferation after day 3 is what we characterize as the second regeneration attempt. When observing the simulation results, proliferation in the 2 Gy case exhibits an immediate sharp increase which quickly appears to settle at a similar level as the experimental data. On the other hand, proliferation in the 5.5 Gy simulations fail to capture the two regeneration attempts (figure (2.4C)), although when looking close, we do see a small sharp increase and decrease in proliferation very early, followed by another, much more slow increase. Additional mechanisms might contribute to this second regeneration attempt, which need to be investigated.

Next, we simulated the K5+ Mx cell lineage by tracking the Mx cells that were derived either from Mx ([Mx-]) or ORS ([Mx+]) after IR is applied, which indicate the ORS-to-Mx flow in the model. We compare the results with the K5+ Mx cell data. Both the 2 Gy and 5.5 Gy IR experimental observations show a quick increase in K5+ Mx cells at early stage (figure 2.5B' blue squares), indicating a fast upward migration of Mx cells after radiation, which is possibly driven by a quick ORS-to-Mx flow. Computationally, in the 2 Gy IR simulation, during the early stage, ORS cells steadily flow into Mx (figure 2.5B red solid line); while in the 5.5 Gy IR simulation, a slow early ORS-to-Mx flow is followed by a sudden increase in the flow speed (figure 2.5B' red solid line), occurring significantly later

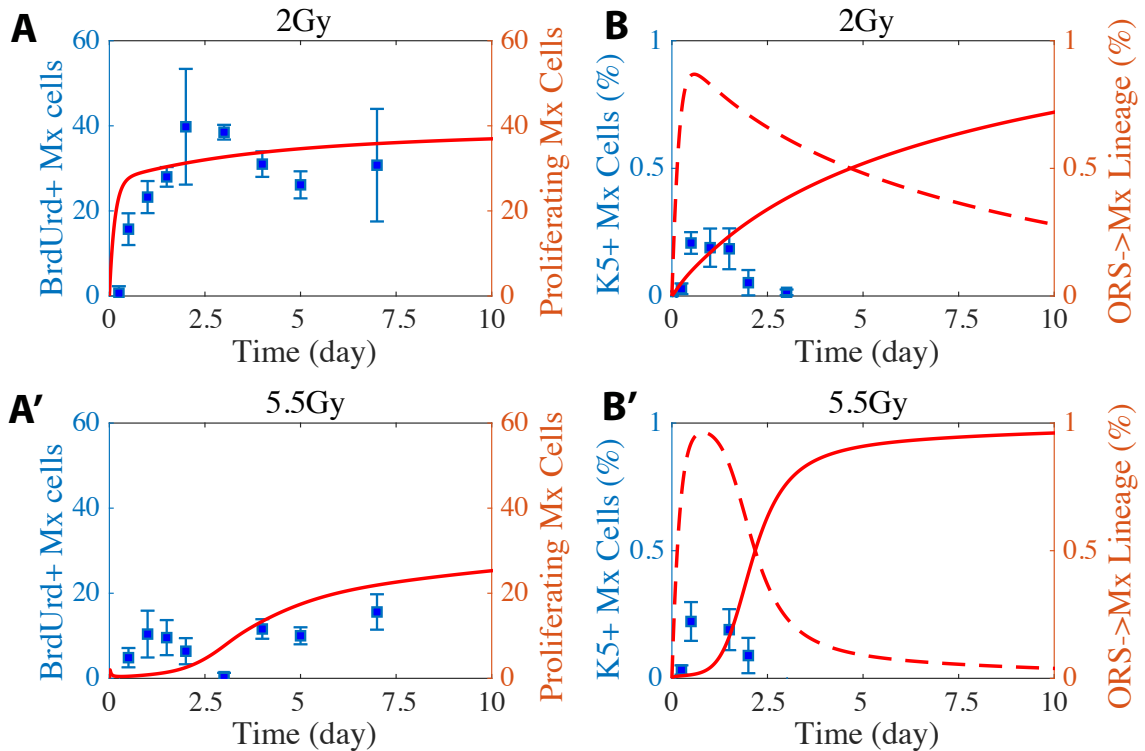


Figure 2.5: Model-data comparison of the IR induced HF regeneration model. Red lines show simulation results with the red y-axis on the right, blue boxes show experimental data with the blue y-axis on the left. **AB** show the simulation / experimental observations with 2 Gy IR, and **A'B'** show simulation / experimental observations with 5.5 Gy IR. **AA'** compare the simulated proliferation Mx cells and the BrdUrd+ Mx cells from experimental observations. **BB'** show the K5+ Mx cells and simulated ORS-to-Mx flow, with red solid lines showing the percentage of post IR Mx cells that are derived from ORS, and red dashed lines showing the percentage of post IR Mx cells that are derived from Mx cells.

than in the experimental observations. This may indicate that additional mechanisms are needed to drive the early ORS-to-Mx flow when subject to strong IR. We point out that observing K5+ Mx cells is not exactly the same as a lineage tracing experiment. This can be easily understood from the decrease in the K5+ Mx cell number soon after the early sudden increase (figure 2.5BB', blue boxes), which would not be seen in a lineage tracing experiment. This results in the long term behavior of K5+ Mx cell data being essentially different from our simulations, though they share some similarity at the early stage. Finally, in both 2 Gy and 5.5 Gy simulations, there is a quick and significant increase in Mx cells

derived from radiated Mx cells returning normal and their proliferation (figure 2.5B red dashed lines).

2.2 Stability of the Homeostatic State of Anagen HF

The major goal of this modeling research is to understand the control mechanisms of the HF regenerative dynamics. In particular, why is the HF able to regenerate itself from the IR induced degeneration during anagen, but cannot stop the progressive degeneration during the catagen? In this part, we apply linear stability analysis, sensitivity analysis, and bifurcation analysis to address this question.

Linear Stability Analysis

In our model, several parameters are identified as directly related to the IR and apoptosis dynamics (group 1 from equation 2.1a). Within these parameters, γ and q depend on the IR strength, Hill exponents n_2 and n_3 are assumed to be a constant, d is the “death” rate of apoptosis cells – the rate at which they quit the system, and usually such a rate is considered to be stable. This leaves six other parameters in this group: the spontaneous apoptosis rates in ORS and Mx cells – s_2 , s_3 , and the Apop-to-ORS, Apop-to-Mx feedbacks strength – α_2 , p_2 , α_3 , p_3 that control the coordinated apoptosis dynamics in ORS and Mx. In controlled mice, during anagen, spontaneous apoptosis in the HF epithelium is hardly detected, as is reported in [22]. Based on this observation, we set the spontaneous apoptosis rates in ORS and Mx, $s_2 = s_3 = 0$ as discussed in section 1.3. Furthermore, the anagen HF homeostasis is characterized by the steady state $(E_q, C_{ORS}, E_{Mx}, 0)$ in our model, as discussed above. Interestingly, linear stability analysis reveals the following result:

Lemma 2. *During anagen with $s_2 = s_3 = 0$, the homeostatic state $(E_q, C_{ORS}, E_{Mx}, 0)$ is stable, and the stability does not depend on the apoptosis feedback strength parameters α_2 , p_2 , α_3 , p_3 .*

Proof. We apply the linear stability to the system equation 1.1 and at the steady state $(E_q, C_{\text{ORS}}, E_{\text{Mx}}, 0)$. For simplicity, we denote $[\text{ORS}_q]$, $[\text{ORS}_a]$, $[\text{Mx}]$, $[\text{Apop}]$ as x_1, x_2, x_3, x_4 , respectively. During anagen, with the assumption $s_2 = s_3 = 0$, the Jacobian at this steady state is

$$J = \begin{pmatrix} 0 & h_{\text{ORS}} & 0 & 0 \\ E & A & B & 0 \\ F & C & D & 0 \\ 0 & 0 & 0 & -d \end{pmatrix}$$

where

$$\begin{aligned} E &= -\frac{\nu_{\text{ORS}}C_{\text{ORS}}}{E_q} \\ A &= -h_{\text{ORS}} \\ B &= 2\nu_{\text{ORS}}C_{\text{ORS}}p_1 \frac{2\alpha_1 E_{\text{Mx}}}{(1 + \alpha_1 E_{\text{Mx}}^2)^2} = \frac{2\nu_{\text{ORS}}C_{\text{ORS}}}{E_{\text{Mx}}(1 + \alpha_1 E_{\text{Mx}}^2)} \\ C &= \nu_{\text{ORS}} \\ D &= -\frac{2\nu_{\text{ORS}}C_{\text{ORS}}}{E_{\text{Mx}}(1 + \alpha_1 E_{\text{Mx}}^2)} + \nu_{\text{Mx}}(2r - 1) \end{aligned}$$

With the fitted parameter values from the IR experiment data, the above Jacobian yields four eigenvalues:

$$\lambda_1 = -d = -2.0755, \lambda_2 = -2.1785, \lambda_3 = -0.0258, \lambda_4 = -0.1440$$

all of which are negative, indicating that the steady state of anagen HF homeostasis is stable. Moreover, notice that the parameters participating in the apoptotic events $(\alpha_2, p_2, \alpha_3, p_3)$ do not show up in the Jacobian, indicating that this steady state stays stable and is independent of these parameter values. \square

This Lemma explains the highly regenerative ability of the HF during anagen, even when subject to high dose of IR. Since the anagen homeostasis is stable and presumably the IR only affects the apoptosis events, the system is able to return to the homeostatic steady state despite strong IR, or equivalently, large α_2 , p_2 , α_3 , p_3 values.

Local Sensitivity Analysis

To further understand the effects of each parameter on the HF regenerative dynamics, we perform both local and global sensitivity analysis in this and the next parts.

For the local sensitivity analysis, we use the one-factor-at-a-time (OFAT) method, that is, changing the value of a particular parameter within a range while keeping the other parameter values fixed. For each parameter, we take the parameter values ranged from 0.5 to 1.5 folds, centered at the calibrated value, and we compare the numerical results of the number of quiescent ORS cells (ORS_q) at day 20, since the number of ORS_q long after application of IR can reflect the HF's ability of regeneration. The parameter sensitivity results from controlled mice (0 Gy IR, no radiation), 2 Gy and 5.5 Gy IR simulations are shown in figure 2.6, where in the 0 Gy simulations (figure 2.6A) we also use the calibrated values of α_2 , p_2 , α_3 , p_3 from the 2 Gy IR data. First, as is already shown by the stability analysis, the HF homeostatic state does not depend on the apoptosis feedback strength parameters α_2 , p_2 , α_3 , p_3 , and the size of ORS_q does not change (figure 2.6A). Next, the 0 Gy system is very sensitive to the parameters p_1 , α_1 , ORS_{max} , where ORS_{max} is defined as $ORS_{max} = E_q + C_{ORS}$, the total number of ORS cells at homeostasis in controlled mice. Decreasing the values of these parameters will greatly inhibit the HF regeneration ability (figure 2.6A). The 0 Gy system is also sensitive to C_{ORS} . Notice that these parameters directly relate to the ORS cell proliferation, thus our results imply that during anagen when spontaneous apoptosis is at a very low level, the regenerative ability of the HF highly depends on its ORS cell proliferation and less on the apoptosis dynamics control. In particular, the sensitivity on p_1 , α_1 should be easy to understand, as we pointed earlier in section 1.3, p_1 and α_1 have to satisfy the constraint equation (1.11) to keep the HF in the

homeostatic state. Therefore changing only one of their values at a time will surely break homeostasis and lead to abnormal regeneration behavior of the HF.

When subjected to radiation (figure 2.6BC), first, as we pointed earlier in parameter calibration (for example, see figure 2.1C'), especially at 5.5 Gy IR, it may take > 20 days for our modeled HF to fully return to the length at homeostasis, therefore all parameter values return a slightly shorter HF at day 20 (figure 2.6C). Next and more important, the system becomes sensitive to more parameters than in the controlled case. These parameters include ν_{ORS} and d , as well as p_3, α_3 which control the apoptosis feedback on Mx cells. As these parameters are varied, there is a subtle decrease in modeled HF length (ORS_q) in the 2Gy case and a much more visible one in the 5.5Gy case. However, no clear change in the sensitivity to the parameters controlling apoptosis feedback on ORS cells (p_2, α_2) is observed in either 2Gy or 5.5Gy case.

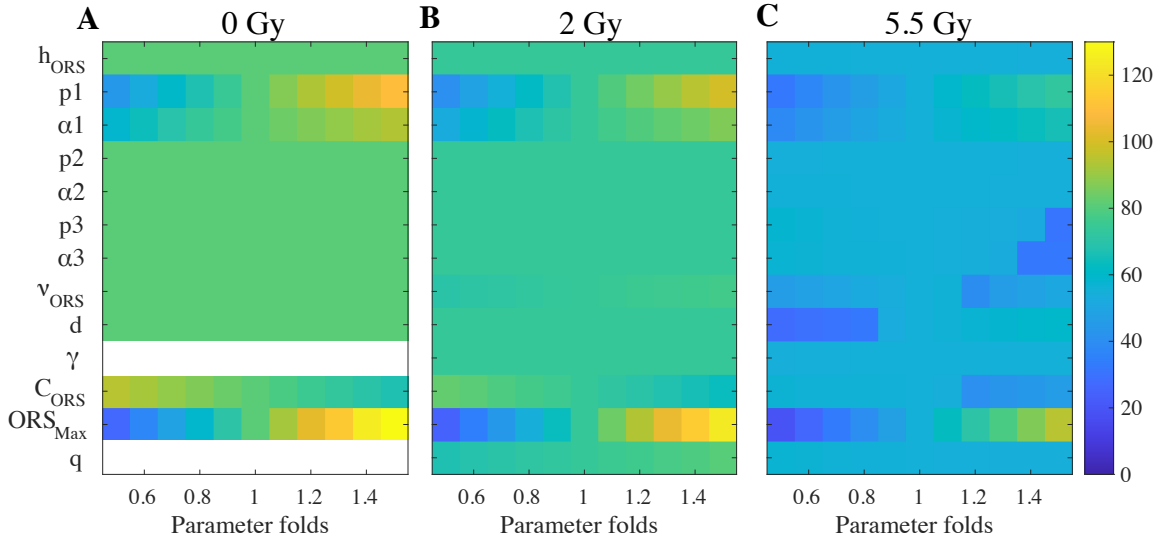


Figure 2.6: Sensitivity of the parameters. At each time, only one parameter value changes, ranged from 0.5- to 1.5-fold of the calibrated value. Heatmap shows the number of quiescent ORS cells (ORS_q) at day 20, as a measure of the HF regeneration ability. Simulations are taken from **A** 0 Gy IR, no radiation, **B** 2 Gy IR and **C** 5.5 Gy IR models. In 0 Gy simulations, we use the calibrated values of α_2 , p_2 , α_3 , p_3 from the 2 Gy IR data.

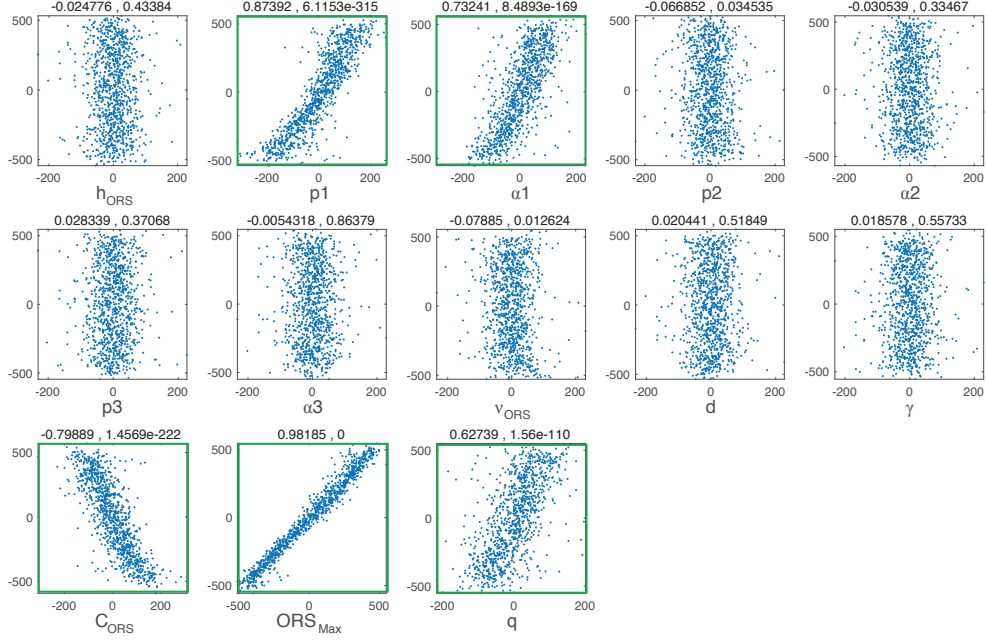
Global Sensitivity Analysis

Next, we perform a global sensitivity analysis on the parameters using the partial rank correlation coefficient (PRCC) measure [63]. Latin hypercube sampling (LHS) is implemented to generate sample parameters, with parameter values uniformly distributed from 0.5 to 1.5 folds of the calibrated value. Similar to the local sensitivity analysis, we assess the number of quiescent ORS cells (ORS_q) at day 20. The PRCC results of 2 Gy and 5.5 Gy IR simulations are shown in figure 2.7, and the trajectories of the $[ORS_q]$ from day 0 (application of the IR) to day 20 are given in figure 2.3. In figure 2.7, the first index on the top of each panel gives the PRCC of that parameter, and the second index gives the p-value.

In 2 Gy simulations, five parameters give nearly zero p-values: p_1 , α_1 , C_{ORS} , ORS_{max} , q , indicating that the output ($[ORS_q]$ at day 20) is sensitive to these parameters. Among them, four (p_1 , α_1 , ORS_{max} , q) show large positive PRCC measures, indicating a positive correlation between them and the output; while C_{ORS} shows a negative correlation with the output. Comparing with the local sensitivity results (figure 2.6B), the system appears to be sensitive to p_1 , α_1 , C_{ORS} , ORS_{max} with both local and global sensitivity analyses, while the PRCC further reveals the sensitivity on q .

In 5.5 Gy simulations, first, we notice that most parameters have smaller p-values comparing to the 2 Gy simulations, indicating that the the system is more sensitive to the parameters comparing to the 2 Gy simulations – this is mostly due to that in the 5.5 Gy simulations, at day 20 mostly the HF has not fully returned to the length at the 510 homeostatic state, as we discussed in the local sensitivity analysis. Next, several parameters show close to 0 p-values. These are p_1 , α_1 , p_3 , α_3 , ν_{ORS} , d , C_{ORS} , ORS_{max} ; they also show large, positive or negative PRCC values. We also notice that the results no longer show sensitivity to q , as in the case of 2 Gy simulations. Moreover, comparing these results with the local sensitivity results (figure 2.6B), we see that they present the same list of sensitive parameters. Among these parameters, p_1 , α_1 , d , ORS_{max} show positive PRCC measures, indicating positive correlations between the parameters and the output, while p_3 , α_3 , ν_{ORS} , C_{ORS} show negative PRCC measures thus negative correlations with the output.

A. 2 Gy, PRCC and p-value



B. 5.5 Gy, PRCC and p-value

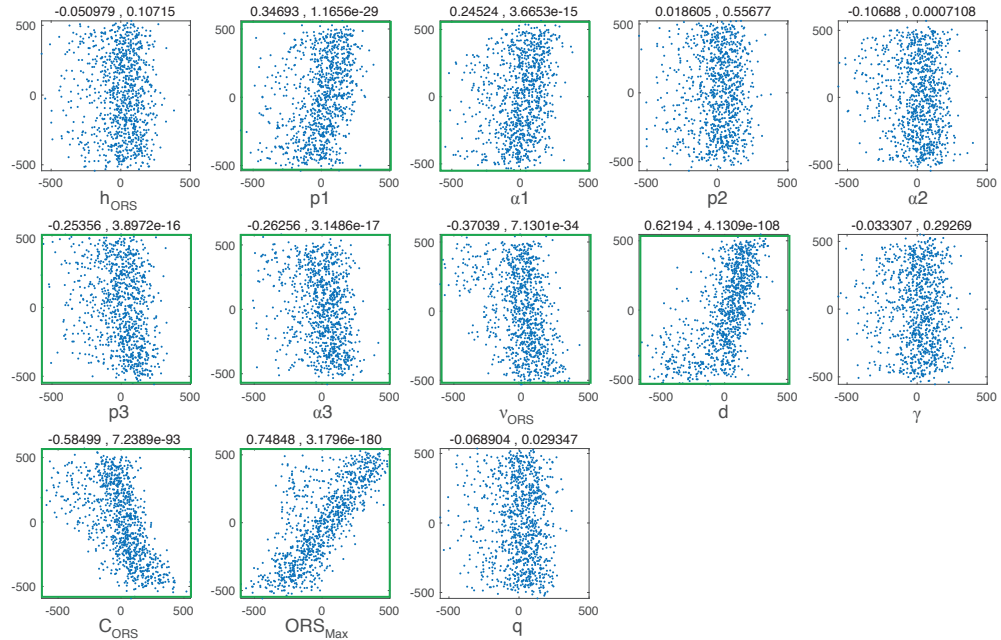


Figure 2.7: PRCC performed on the A) 2 Gy and B) 5.5 Gy IR models. Parameter values are sampled using LHS, with each parameter uniformly distributed between 0.5 to 1.5 folds of the calibrated value. The first / second index on top of each panel shows the PRCC / p-value of that parameter. Parameters showing large PRCC and small p-value are highlighted by the green boxes.

Bifurcation Analysis

At the late stage of anagen, spontaneous apoptosis becomes prominent in Mx, which later triggers the upward propagating apoptosis wave, marking the anagen-to-catagen transition. Unlike the IR induced HF degeneration, the degeneration during catagen is irreversible and only comes to a stop when the HF enters the resting telogen phase.

In our model, the spontaneous apoptosis rate in Mx is controlled by the parameter s_3 , previously set to zero to represent the absence of spontaneous apoptosis in anagen. To understand its effect, we apply bifurcation analysis with respect to s_3 on the following systems. System 1.1 with the 2Gy calibrated parameter values, system 1.1 with the 5.5 Gy calibrated parameter values, and a few more “intermediate systems” (IS) with values of p_2 , α_2 , p_3 , α_3 varying between the 2 Gy and 5.5 Gy calibrated values (figure 2.8, all bifurcation diagrams generated by XPPAuto, parameter values of p_2 , α_2 , p_3 , α_3 listed in table 2.2).

Table 2.2: *Parameter values of p_2 , α_2 , p_3 , α_3 in the bifurcation diagrams from figure 2.8. IS stands for “intermediate system”.*

	2Gy IR	IS 1	IS 2	IS 3	IS 4	5.5 Gy IR
p_2	0.059416	0.1	0.4	0.7	0.8	0.9985
α_2	0.071299	0.05	0.03	0.02	0.021	0.022659
p_3	0.00015273	0.1	0.4	0.7	0.8	0.99977
α_3	0.0032523	0.01	0.02	0.03	0.04	0.042646

First, in the 2 Gy case we observe that the stability of the steady state does not change with s_3 (figure 2.8A). Considering that the 2 Gy IR system has very weak apoptosis feedbacks on both Mx and ORS cells, determined mostly by the values of p_2 , p_3 (table 2.2), this implies that increasing the spontaneous apoptosis rate (s_3) alone cannot lead to the apoptosis wave or the catagen HF degeneration. On the other hand, in the 5.5 Gy IR system (figure 2.8F), due to the strong apoptosis feedback on both ORS and Mx cells (p_2 , p_3), an

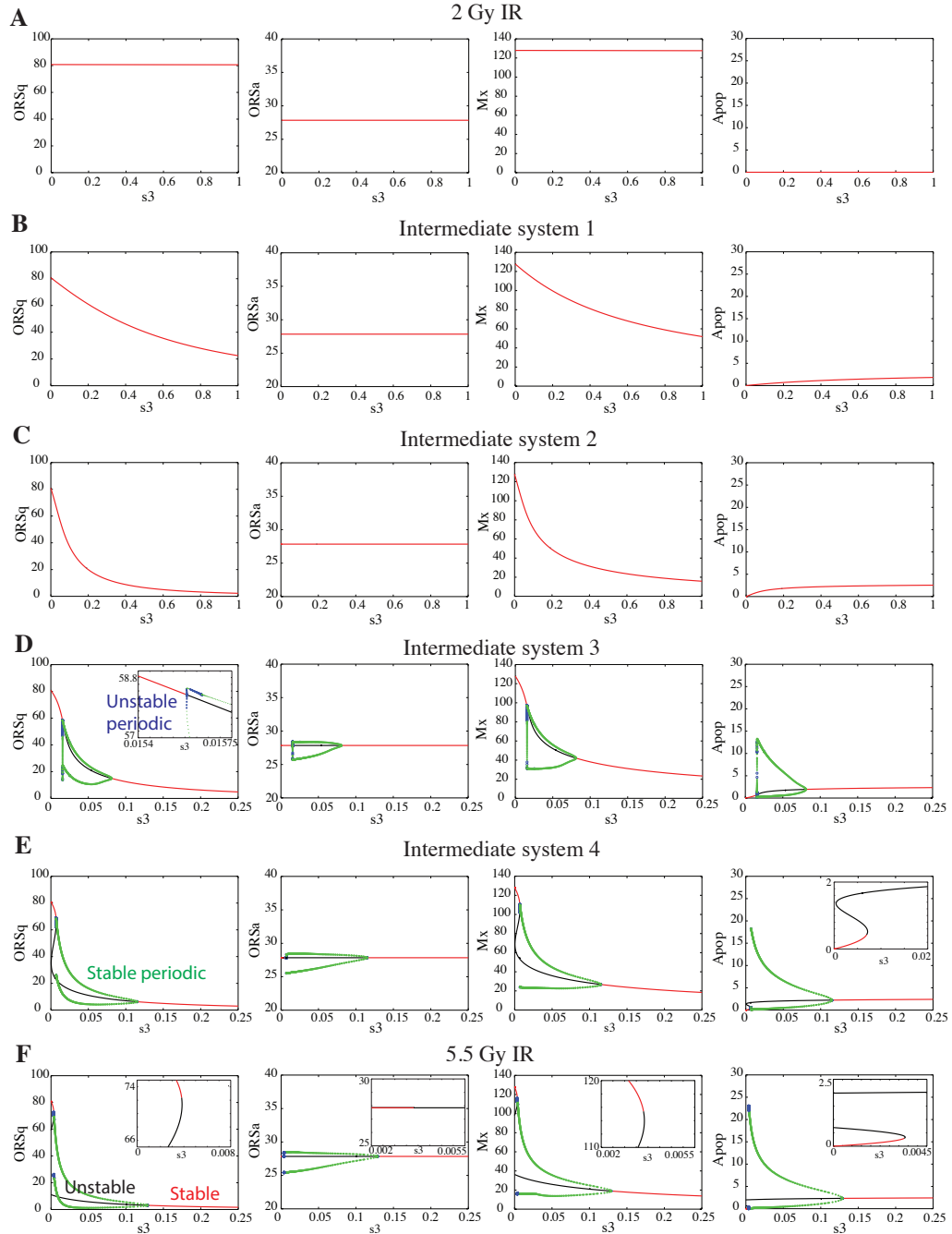


Figure 2.8: Bifurcation diagrams of the HF regeneration dynamics with respect to the Mx cells' spontaneous apoptosis rate s_3 . **A**, 2 Gy IR system. **BCDE**, intermediate systems 1-4, **F** 5.5 Gy IR system. Parameter values of p_2 , p_3 , α_2 , α_3 of the systems are provided in table 2.2. Red solid line - stable state, black solid line - unstable state, green dots - stable periodic solution, blue circles - unstable periodic solution. A close up view in **D** shows a small region of unstable periodic solution. Close up views of the stable (red) and unstable (black) solutions near the anagen HF homeostatic state are shown in **F**, with the dots indicating periodic solutions removed.

increase in the spontaneous apoptosis rate in Mx cell (s_3) quickly breaks down the stability of the homeostatic state: first, a Hopf bifurcation is triggered leading to a periodic solution region (figure 2.8F, green dots), followed by another stable steady state representing the degenerated HF (figure 2.8F, red solid lines).

The intermediate systems show how the steady state evolves as the apoptosis feedbacks get stronger. With weak apoptosis feedbacks (figure 2.8BC), the steady state is able to remain stable as s_3 increases, pushing the HF system from the homeostatic state to the degenerated state. Then at a certain level of apoptosis feedback, a Hopf bifurcation occurs and a transient periodic domain shows up (figure 2.8DEF). The Hopf bifurcation is identified as subcritical, that is, an unstable periodic solution region (shown by blue circles in the close-up plot in figure 2.8D), is quickly followed by a stable periodic solution region (green dots in figure 2.8DEF). We point out that the unstable periodic-solution region is very small, and difficult to identify in XPPAuto, showing a jump from the homeostatic stable steady state to the periodic solution (figure 2.8EF).

Dynamic simulations of system 1.1 with 5.5 Gy calibrated parameter values $p_2, \alpha_2, p_3, \alpha_3$ and different s_3 values are shown in figure 2.9. In agreement with the bifurcation diagrams (figure 2.8), with $s_3 = 0$, that is, no spontaneous apoptosis in Mx cells, the HF stays in the stable homeostatic state (figure 2.9A). A small value of s_3 results in the degeneration of the HF, followed by periodic dynamics (figure 2.9B), while further increasing s_3 results in the full degeneration of the HF without showing periodic dynamics (figure 2.9C), which could represent the full degeneration dynamics of the catagen phase. This reveals the important roles of the Mx spontaneous apoptosis rate (s_3) and the apoptosis feedback strengths ($p_2, \alpha_2, p_3, \alpha_3$) on the HF degeneration dynamics.

We continue our bifurcation analysis on the apoptosis feedback strengths by making a simplifying assumption on the model and letting $p = p_2 = p_3$. The values of α_2 and α_3 are fixed as the 5.5 Gy calibrated values. For small values of s_3 , increasing the bifurcation parameter p induces a decrease in both ORS_q and Mx cells in the stable steady state, together with a slight increase in apoptosis cells (figure 2.10A). As the apoptosis feedback

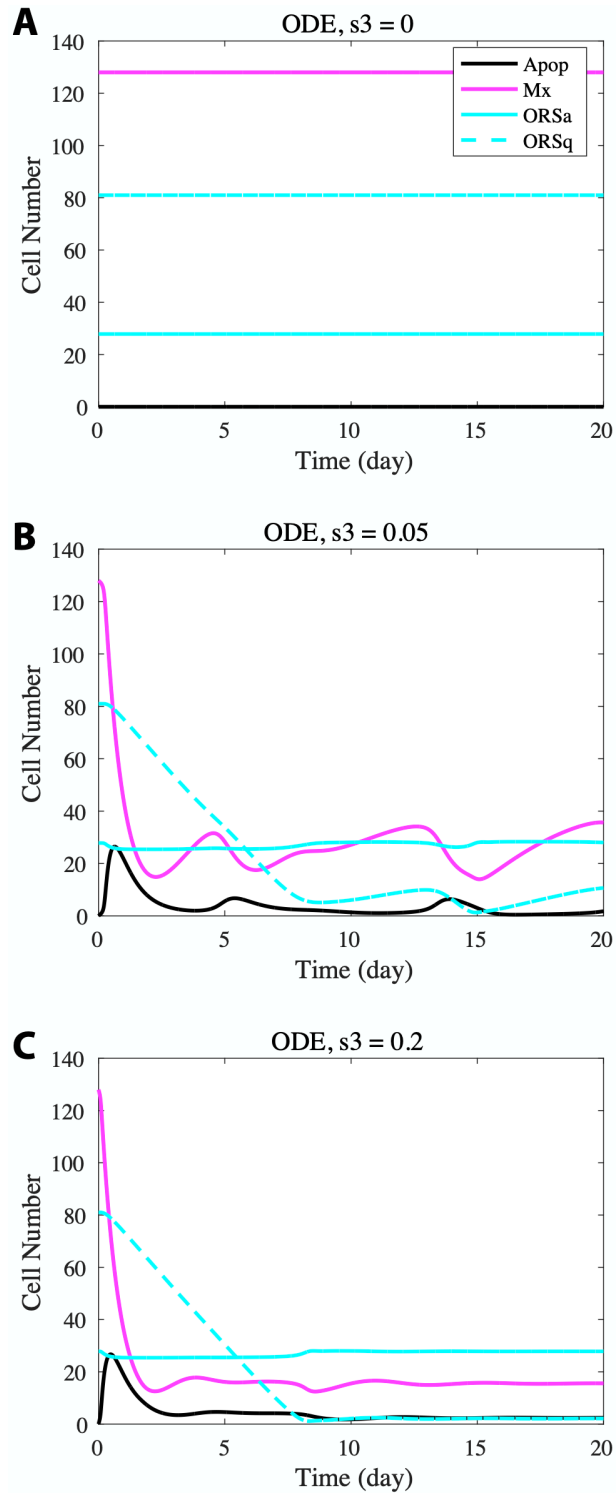


Figure 2.9: *Dynamic simulations of the HF cell population system with different Mx spontaneous apoptosis rate values (s_3). A, $s_3 = 0$, no spontaneous apoptosis in Mx cells, HF stays in the stable homeostatic state. B, $s_3 = 0.05$, HF degenerates, followed by small amplitude of periodic dynamics. C, $s_3 = 0.2$, HF fully degenerates.*

strength ($p = p_2 = p_3$) keeps increasing, a Hopf bifurcation is triggered and the system enters the periodic solution domain. On the other hand, when s_3 is larger, no bifurcation occurs with p , and increasing the apoptosis feedback strength causes a decrease in ORS_q and Mx cells in the stable steady state, together with an increase in the apoptosis cells. Also refer to example dynamic simulations in figure 2.9.

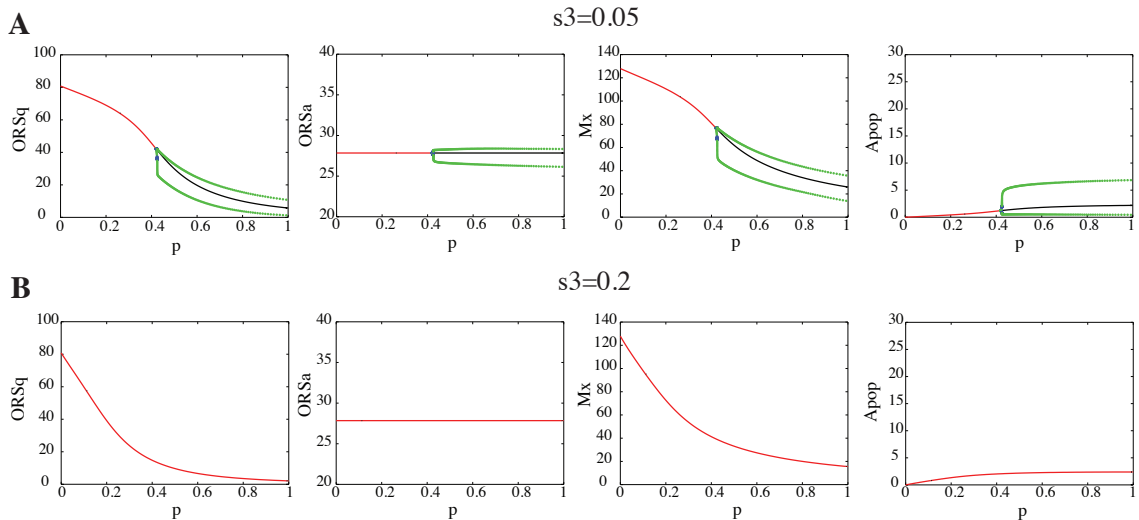


Figure 2.10: *Bifurcation diagrams of the HF regeneration dynamics with respect to the apoptosis feedback strength $p = p_2 = p_3$. α_2, α_3 values are taken from the 5.5 Gy IR system. A, $s_3 = 0.05$. B, $s_3 = 0.2$.*

Finally, we point out that catagen is a transient phase that is typically much shorter than anagen or telogen. If the Mx cells' spontaneous apoptosis rate (s_3) quickly increases at the anagen-to-catagen transition, it may push the system from the anagen homeostatic state (small s_3) to the degenerating state (large s_3), completely bypassing the periodic behavior. This is illustrated by our simulation of the anagen-to-catagen transition dynamics in figure 2.11, where we set up a linear increase of s_3 from day 5 to day 10 (figure 2.11A). The resulting deterministic dynamics are shown in figure 2.11B, from which we see that the increase in s_3 steadily induces the degeneration of the HF, and we hardly see any periodic dynamics. This may explain why periodicity is not observed in experiments. In addition, during catagen, more complicated morphological deformations occur in the HF, therefore

at the late catagen stage, our cell differentiation population model might no longer be adequate.

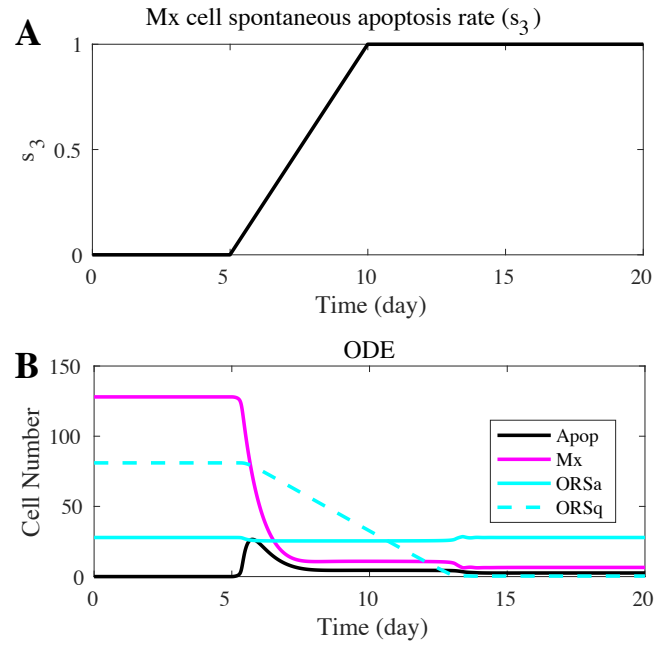


Figure 2.11: *Simulation of the anagen-to-catagen transition dynamics. A* At day 5, s_3 increases linearly, causing the degeneration of the HF epithelium. *B* ODE simulation results.

2.3 Modeling Effect of PGE2 Treatment on IR-exposed HF

New experimental results testing effectiveness of Prostaglandin E2 (PGE2) drug against radiotherapy-induced alopecia (RIA) reveal that PGE2 treatment reduced hair loss in mouse HF by preventing premature termination of anagen and enhancing HF self repair. PGE2 did not activate HF stem cells, but it preserved more transit amplifying cells (TACs) for regenerative attempts. Pretreatment of PGE2 lessened radiosensitivity of TACs and reduced TAC apoptosis and therefore mitigated HF dystrophy [65].

We would like to further validate our mathematical model by replicating the new experimental results in simulations. Modeling results should show regenerative dynamics in Mx and ORS (which are TACs), and simultaneously a delay and decrease in apoptosis cells. We hope that by perturbing certain parameters in our model, we can observe the expected behavior. We point out that a stronger dose of 8.5Gy IR is administered in the recent experiments; given the current fit of apoptosis feedback parameters p_2, p_3 , in our model (2.1) for the 5.5Gy system being nearly at their maximum value of one, we attempt to model the stronger 8.5Gy IR effect by instead perturbing the spontaneous apoptosis rates (s_2 or s_3) and IR-related parameters q and γ , where the terms γq and $\gamma(1 - q)$ in equations 1.9 represent the rate at which IRMx return to normal Mx and the rate at which IRMx start apoptosis, respectively. In our current 2Gy and 5.5Gy models, s_2 or s_3 are set to zero to represent the absence of spontaneous apoptosis in the anagen phase, however our bifurcation analysis revealed that by increasing s_3 , those systems with strong enough apoptosis feedback i.e. systems IS3, IS4 and 5.5 Gy, show a bifurcation pushing the homeostatic steady state of the anagen HF away from stability (see Figure 2.8). Thus, we further explore the s_3 bifurcating region in search of similar dynamics to those observed in experiments with PGE2 treatment.

We arbitrarily choose a region of s_3 that contains the bifurcating region in each system, q ranges along its domain which is $(0, 1)$, and the γ region is chosen arbitrarily with the only requirement that it contains its fitted value. Thus by means of LHS on $s_3, q, \gamma \in$

$(0.01, 0.04) \times (0, 1) \times (0, 5)$ for the systems IS3, IS4 and 5.5Gy, we run $N = 2000$ sample dynamics using our model and categorize each as either being of regenerative or degenerative trend; the criteria is that if the last trajectory point value is greater than the previous, the trajectory is considered regenerative, and it is considered degenerative if the opposite is true. In Figure 2.12, degenerative trajectories are the black open dots, all other solid dots are regenerative trajectories. We also plot the sample trajectories of ORSq with respect to time.

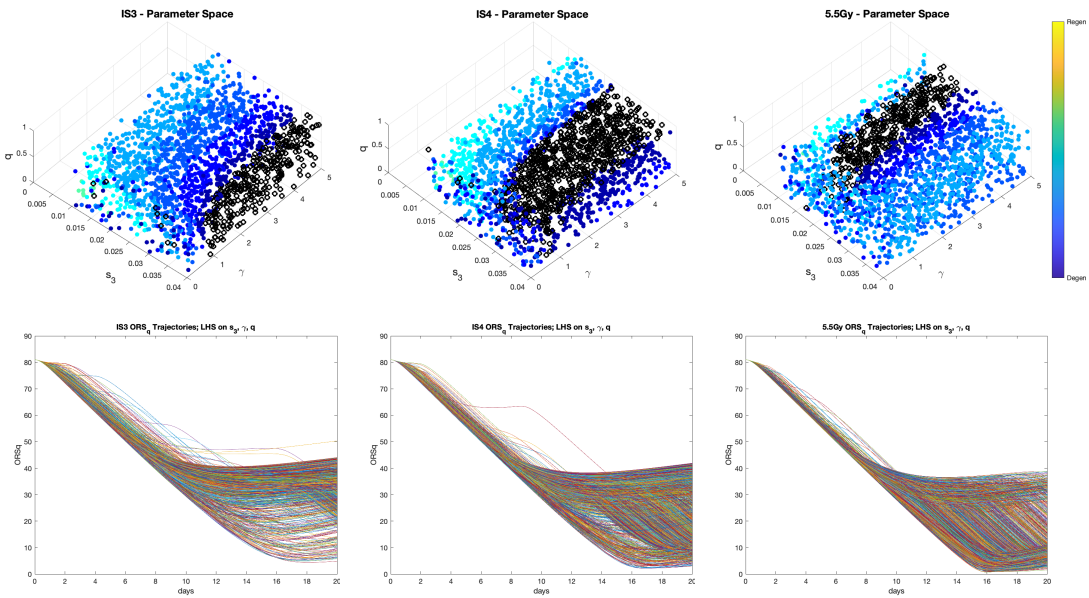


Figure 2.12: s_3, q, γ parameter space (top) and trajectories (bottom) for systems IS3, IS4 and 5.5Gy In parameter space, degenerative trajectories of ORSq are represented as black open dots, other solid dots are regenerative trajectories. The bottom figures are the sample trajectories of ORSq over time.

The LHS reveals what that the ORSq (which we take as a rough indicator of HF length) can display regenerative dynamics, even when IR- related parameters q and γ are high. However we also hope to see a general delay and/or decrease in the dynamics of apoptotic cells. Logically, we can deduce that a higher q value, or higher rate of return to normalcy, implies a lower $(1 - q)$ value and thus a lower rate of apoptosis in IRMx. In Figure 2.13, we choose two values of s_3 and a high q value, while γ is fixed at its originally 5.5Gy fitted value.

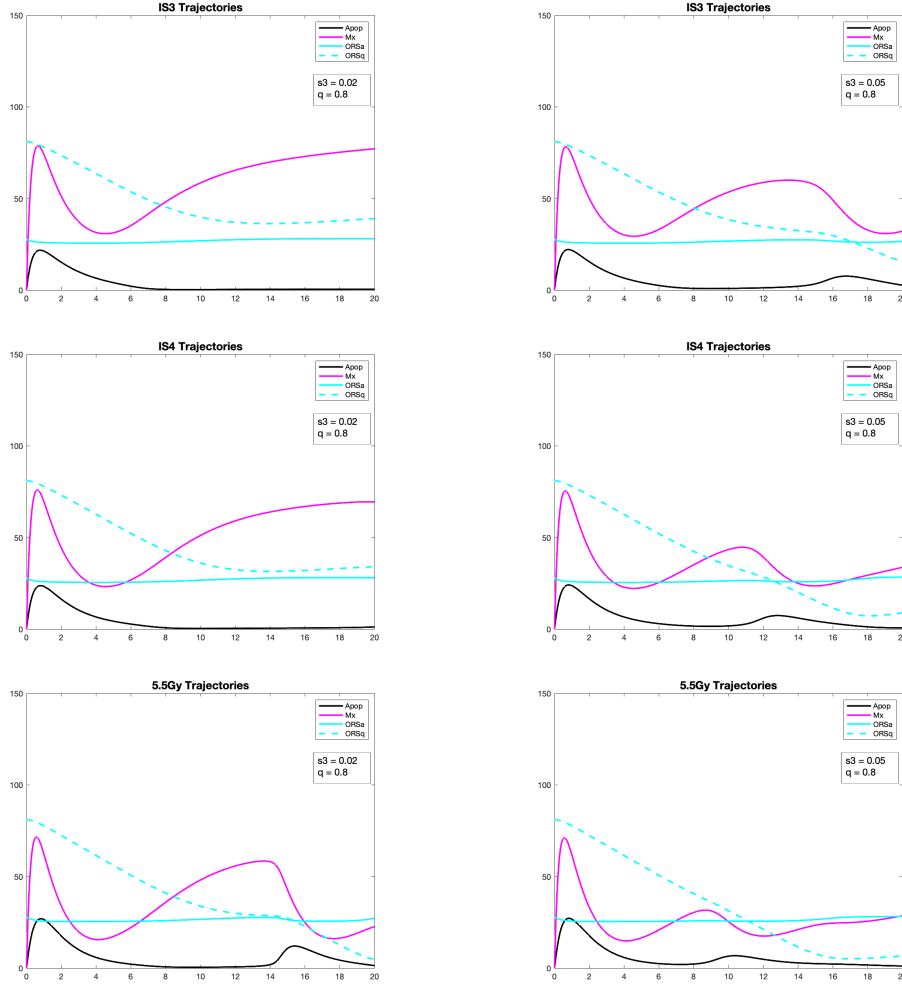


Figure 2.13: HF dynamics for IS3, IS4 and 5.5Gy systems with increased s_3 and q . Increase in Mx cells' spontaneous apoptosis rate s_3 and rate q at which IRMx returns to Mx, results in a less abrupt spike in Apop cells compared to the dynamics from Figure 2.4, which can be considered a slight delay in apoptosis. When we compare the trajectories of the 5.5Gy system with $s_3 = 0.05$ and $q = 0.8$ to the dynamics of 5.5G in Figure 2.9 B, we note that the increase in q results in less-oscillating dynamics for all compartments. Here, γ is fixed at the 5.5Gy fitted value.

Additionally, in Figure 2.14 we also choose a low γ value, representing a lower frequency at which IRMx quits its interrupted state. Here we point out that indeed the apoptosis cells dynamics seem to change into a gradual increase and decrease in the population size that rather than a spike as in the previous cases. We also note that the Mx population seems to make a substantial recovery.

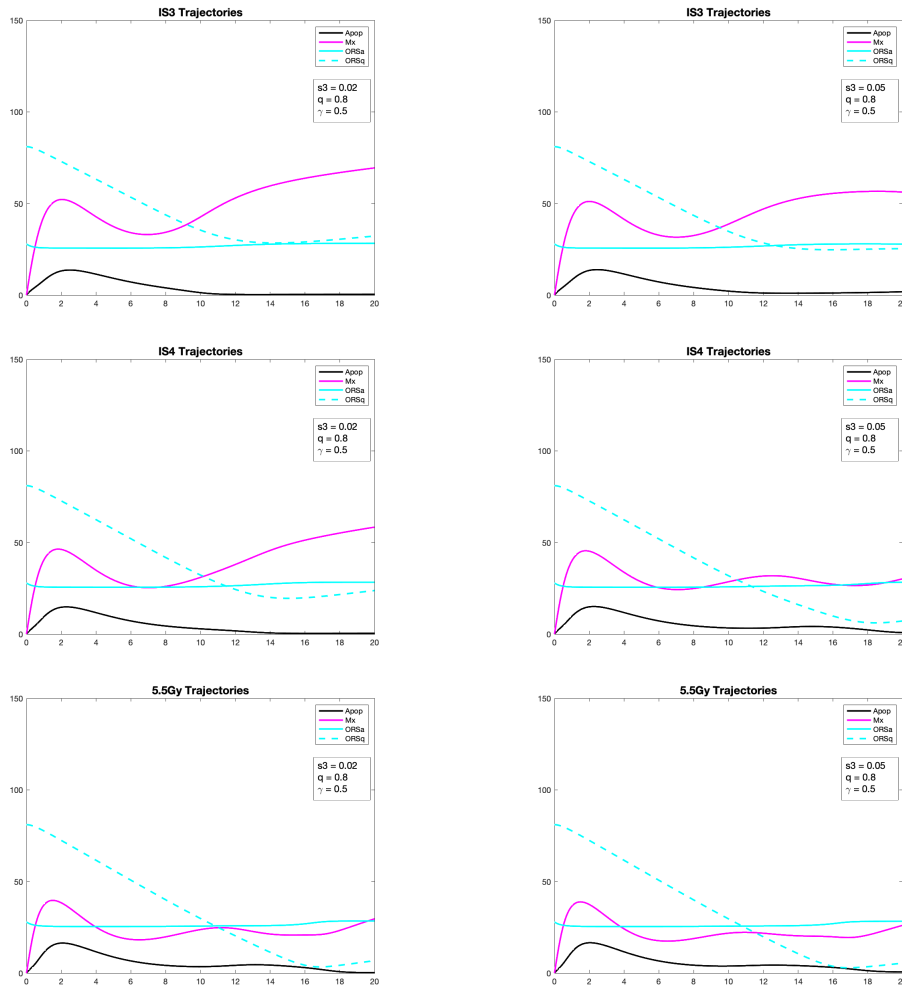


Figure 2.14: *HF dynamics for IS3, IS4 and 5.5Gy systems with increased s_3 and q and decreased γ . Increase in Mx cells' spontaneous apoptosis rate s_3 and rate q at which $IRMx$ returns to Mx while also reducing the frequency at which $IRMx$ quits interrupted state, γ , results in a less abrupt wave of apoptosis that is subtle yet prolonged over time.*

These preliminary results show that the model can produce desirable effect on the dynamics of the apoptosis cells in agreement with those observed in the experiments, however we realize that ideally all other compartments would also show regenerative dynamics. Thus we discuss possible future directions in the next chapter that can potentially help to improve our model and better replicate the newest experimental findings.

Chapter 3

Conclusions and Discussion

In this work, we developed a new ODE type of HF cell differentiation population model, and used it to investigate the underlying mechanisms of the IR induced HF regeneration and the catagen HF degeneration. The model for controlled mice includes four cell states – quiescent ORS, active ORS, Mx and apoptosis cells. While the last three types of cells together make up the dynamic part at the bottom of an anagen HF, the HF length can be estimated by the size of ORS – including both quiescent and active ORS – as ORS forms the outer concentric epithelial layer of the HF (Figure 1.1B), and it connects the bulge stem cell niche near the top of the HF and the HF dynamic part at the bottom. We also extend this model by adding another state representing the radiated Mx cells, and apply this extended model to study the IR induced HF regeneration dynamics. Model parameters are calibrated from IR experimental data, subjected to either 2 Gy or 5.5 Gy IR. Data calibration results show a good match between the model and the data, especially in the 2 Gy IR system, though in the 5.5 Gy IR system, the model shows a slower HF regeneration compared to the data. However our ODE model still validates the regenerative dynamics induced by IR to a reasonable extent. Furthermore, the stability, sensitivity and bifurcation analyses reveal that during anagen, due to the extremely low spontaneous apoptosis rates in epithelial cells (s_2, s_3), the homeostatic anagen HF steady state is stable, and does not depend on the apoptosis feedback strength ($p_2, \alpha_2, p_3, \alpha_3$). This explains why an anagen HF is able to return to its

homeostatic state despite large scale degeneration caused by strong IR. Sensitivity analysis reveals a few factors that are important to the HF regenerative ability, including ORS cell proliferation, and that though the apoptosis feedback strength does not affect the HF regeneration in controlled mice, Mx cells' apoptosis feedback strength (p_3, α_3) may indeed affect the HF regeneration when subjected to IR. Further bifurcation analysis reveals that to push the HF from the anagen homeostasis to the irreversible degeneration in catagen, the system needs both Mx cells' spontaneous apoptosis rate (s_3) and the apoptosis feedback strength (p_2, p_3) to be strong. A transient periodic domain is revealed from the bifurcation analysis and the simulations, though in reality, a fast anagen-to-catagen transition may quickly push the system from the anagen steady state to the catagen steady state, without clearly showing the periodic dynamics – yet further experimental and modeling research would be needed to confirm this prediction. We also point out that in our current parameter calibration, while the results show good match with the 2 Gy IR data, in the 5.5 Gy IR case, it seems that the data shows a faster ORS-to-Mx flow right after the IR application as well as a faster HF regeneration when compared to our model. We suspect that this is partially due to our simple assumption of the HF length control mechanism (equation 1.2). We expect more biological evidence to emerge in the future, from which we can improve on the HF length control function in a more mechanistic way.

We also presented some preliminary modeling results in an attempt to replicate new experimental findings that strong-IR-induced HF damage can be attenuated with treatment of PGE2 drug. Despite the model producing some desirable attributes on the dynamics of the apoptotic cells that could correspond to PEG2 treatment, we realize that ideally all other compartments would also show a regenerative trend. Some ways to improve our model in the future model is to recalibrate the model parameters incorporating the newly obtained experimental data. However, before performing new parameter calibrations, we also propose a reformatting of the apoptosis feedback signal functions that could potentially reduce the

number of parameters to calibrate. We can modify the functions in 1.4 as

$$p_{\text{ORS}}^a([\text{Apop}]) = p_2 \left[s_2 + \frac{1}{1 + \left(\frac{[\text{Apop}]}{\alpha_2} \right)^{n_2}} \right] \quad (3.1a)$$

$$p_{\text{Mx}}^a([\text{Apop}]) = p_3 \left[s_3 + \frac{1}{1 + \left(\frac{[\text{Apop}]}{\alpha_3} \right)^{n_3}} \right] \quad (3.1b)$$

Note that in this notation, the parameters $\alpha_2, \alpha_3, n_2, n_3$ are not the same as in equations 1.4. Here, α_2 represent the amount of [Apop] at which the apoptosis feedback rate of ORSa is $p_2/2$, and similarly for α_3 and the apoptosis feedback rate of Mx. Additionally, imposing better constrains may also help improve the apoptotic feedback signals, for example, future fittings should add the constrains that intuitively α_2, α_3 be larger for 2Gy than for 5.5Gy, indicating that the apoptosis feedback mechanism activates with a smaller current quantity of apoptosis cells in the 5.5Gy case than in the 2Gy. Furthermore, we can also let n_2, n_3 be some negative integer of larger magnitude such as $n_2 = n_3 = -10$, this way the feedback mechanism exhibits a more instantaneous activation rate. The parameters p_2, p_3 then represent the magnitude of such feedback signals and intuitively should have lower values for lower IR and higher values for higher IR systems. Using this representation, we may be able to perturb these parameters manually and remove from the fitting process. This essentially entails repeating the entire calibration process and is an avenue that may or may not want to be explored.

All in all, our current model still provides a mathematical explanation of the underlying mechanisms of an anagen HF, IR-induced regenerative dynamics and the catagen degenerative dynamics, and it provides potential guidance in future HF biology experimental research and radio-therapeutic study. Other directions that can be further improved in the future are the following. Currently in our model, there are two major simplifying assumptions: 1) while ORS is a continuum whose activation and quiescence is regulated by signaling gradients, in our model we assume them to be two sub-states as *active* and *quiescent* ORS,

and 2) the HF length control in our system is currently modeled phenomenologically by equation 1.2, where in reality, this mechanism has not yet been identified in current HF biology. In the future, a PDE type of cell differentiation population model incorporating the spatial information in HF growth – or more specifically, the growth of the ORS, might well substitute our assumption of the *active* and *quiescent* ORS sub-states, and provide more accurate description and better insights of the HF generation dynamics. In addition, further modeling development on the signaling regulation might also be helpful. Currently in our model we include signal A - which may represent for example Tnf - that regulates HF epithelial cells' apoptosis, and signal B - which may represent Wnt and Shh - that regulates ORS cells' proliferation. However, Shh may also play a role in regulating Mx cell proliferation, by either directly signaling to Mx or indirectly signaling to DP to perturb other signals affecting Mx cell proliferation. Furthermore, there are other well-known signaling pathways that cooperatively regulate HF growth, for example, Bmp, Tgf- β and Fgf. How these signals react to IR and thus regulate the HF regeneration needs to be explored from both experimental and modeling sides.

Finally, recent experimental research also reveal the HF degenerative / regenerative dynamics after chemotherapy [61,62]: when the HF is exposed to a low level of chemo-drug, the HF is able to stay in anagen despite a damaged hair fibre, referred to as the dystrophic anagen; on the other hand, when exposed to a high level of chemo-drug, the HF enters catagen and starts degeneration, followed by telogen until it enters the next anagen phase, referred to as the dystrophic catagen. While the low level chemo-drug induced dystrophic anagen shares some similarities with the 2 Gy IR-induced HF regeneration, the high level chemo-drug induced dystrophic catagen is very different from the 5.5 Gy IR-induced HF regeneration. What causes the difference between the chemo- vs. IR-induced HF degenerative / regenerative dynamics is an interesting question and needs further investigations on both experimental and modeling sides, and we suspect that though some similarities probably exist, chemotherapy and IR may trigger different signaling pathways that lead to the different regenerative dynamics. For example, it is reported that Shh may play a bigger role in

the chemo-drug induced HF degenerative dynamics, comparing to in the IR-induced HF regenerative dynamics [22,61,62]. Considering that disrupting the Shh signal may inhibit Mx cell proliferation leading to HF degeneration, and that Mx is a major source of Shh signal, how such feedback affects the chemo- vs. IR-induced HF degeneration / regeneration should be studied in the future.

Bibliography Part I

- [1] Ralf and Foitzik Paus Kerstin, *In search of the “hair cycle clock”: a guided tour*, *Differentiation* **72** (2004), no. 9-10, 489–511, DOI 10.1111/j.1432-0436.2004.07209004.x.
- [2] Ya-Chieh and Li Hsu Lishi and Fuchs, *Transit-amplifying cells orchestrate stem cell activity and tissue regeneration*, *Cell* **157** (2014), no. 4, 935–949, DOI 10.1016/j.cell.2014.02.057.
- [3] KS and Paus Stenn Ralf, *Controls of hair follicle cycling*, *Physiological reviews*, posted on 2001, DOI 10.1152/physrev.2001.81.1.449.
- [4] EJ and Ekel Van Scott TM and Auerbach, *Determinants of rate and kinetics of cell division in scalp hair*, *Journal of investigative dermatology* **41** (1963), no. 5, 269–273.
- [5] FREDERICK D and KEANE MALKINSON JOHN T, *Hair matrix cell kinetics: a selective review*, *International journal of dermatology* **17** (1978), no. 7, 536–551, DOI 10.1111/j.1365-4362.1978.tb05997.x.
- [6] Ya-Chieh and Pasolli Hsu H Amalia and Fuchs, *Dynamics between stem cells, niche, and progeny in the hair follicle*, *Cell* **144** (2011), no. 1, 92–105, DOI 10.1016/j.cell.2010.11.049.
- [7] Gerd and Botchkarev Lindner Vladimir A and Botchkareva, *Analysis of apoptosis during hair follicle regression (catagen)*, *The American journal of pathology* **151** (1997), no. 6, 1601.
- [8] Sven and Rossiter Müller-Röver Heidi and Lindner, *Hair follicle apoptosis and Bcl-2*, *Journal of Investigative Dermatology Symposium Proceedings*, 1999, pp. 272–277, DOI 10.1038/sj.jidsp.5640228.
- [9] William E and Chase Straile Herman B and Arsenault, *Growth and differentiation of hair follicles between periods of activity and quiescence*, *Journal of Experimental Zoology* **148** (1961), no. 3, 205–221, DOI 10.1002/jez.1401480304.
- [10] Anne R and Polakowska Haake Renata R, *Cell death by apoptosis in epidermal biology*, *Journal of Investigative Dermatology* **101** (1993), no. 2, 107–112, DOI 10.1111/1523-1747.ep12363594.
- [11] Rald and Rosenbach Paus Thomas and Haas, *Patterns of cell death: the significance of apoptosis for dermatology*, *Experimental dermatology* **2** (1993), no. 1, 3–10, DOI 10.1111/j.1600-0625.1993.tb00192.x.
- [12] Renata R and Piacentini Polakowska Mauro and Bartlett, *Apoptosis in human skin development: morphogenesis, periderm, and stem cells*, *Developmental Dynamics* **199** (1994), no. 3, 176–188, DOI 10.1002/aja.1001990303.
- [13] D and Strutton Weedon G, *Apoptosis as the mechanism of the involution of hair follicles in catagen transformation.*, *Acta dermato-venereologica* **61** (1981), no. 4, 335–339.
- [14] Natalia V and Ahluwalia Botchkareva Gurpreet and Shander, *Apoptosis in the hair follicle*, *Journal of investigative dermatology* **126** (2006), no. 2, 258–264, DOI 10.1038/sj.jid.5700007.
- [15] Keizo and Mori Matsuo Osamu and Hashimoto, *Apoptosis in murine hair follicles during catagen regression*, *Archives of dermatological research* **290** (1998), no. 3, 133–136, DOI 10.1007/s004030050278.
- [16] Li Chun and Liu Wang Zhong-Ying and Shapiro, *Conditional disruption of hedgehog signaling pathway defines its critical role in hair development and regeneration*, *Journal of Investigative Dermatology* **114** (2000), no. 5, 901–908, DOI 10.1046/j.1523-1747.2000.00951.x.

- [17] Noboru and Leopold Sato Philip L and Crystal, *Induction of the hair growth phase in postnatal mice by localized transient expression of Sonic hedgehog*, The Journal of clinical investigation **104** (1999), no. 7, 855–864.
- [18] Wing-Cheong and Chou Lo Ching-Shan and Gokoffski, *Feedback regulation in multistage cell lineages*, Mathematical biosciences and engineering: MBE **6** (2009), no. 1, 59, DOI 10.3934/mbe.2009.6.59.
- [19] Arthur D and Gokoffski Lander Kimberly K and Wan, *Cell lineages and the logic of proliferative control*, PLoS Biol **7** (2009), no. 1, e1000015, DOI 10.1371/journal.pbio.1000015.
- [20] Marie and Marciniak-Czochra Doumic Anna and Perthame, *A structured population model of cell differentiation*, SIAM Journal on Applied Mathematics **71** (2011), no. 6, 1918–1940, DOI doi.org/10.1137/100816584.
- [21] Anna and Stiehl Marciniak-Czochra Thomas and Ho, *Modeling of asymmetric cell division in hematopoietic stem cells—regulation of self-renewal is essential for efficient repopulation*, Stem cells and development **18** (2009), no. 3, 377–386, DOI 10.1089/scd.2008.0143.
- [22] Wen-Yen and Lai Huang Shih-Fan and Chiu, *Mobilizing transit-amplifying cell-derived ectopic progenitors prevents hair loss from chemotherapy or radiation therapy*, Cancer research **77** (2017), no. 22, 6083–6096, DOI 10.1158/0008-5472.
- [23] M and Derry Eroglu WB, *Your neighbours matter—non-autonomous control of apoptosis in development and disease*, Cell Death & Differentiation **23** (2016), no. 7, 1110–1118, DOI 10.1038/cdd.2016.41.
- [24] Ainhoa and Fuchs Pérez-Garijo Yaron and Steller, *Apoptotic cells can induce non-autonomous apoptosis through the TNF pathway*, Elife **2** (2013), e01004, DOI 10.7554/eLife.01004.001.
- [25] Tsutomu and Ogo Soma Masashi and Suzuki, *Analysis of apoptotic cell death in human hair follicles in vivo and In vitro*, Journal of Investigative Dermatology **111** (1998), no. 6, 948–954, DOI 10.1046/j.1523-1747.1998.00408.x.
- [26] Sarah E Millar, *Molecular mechanisms regulating hair follicle development*, Journal of Investigative Dermatology **118** (2002), no. 2, 216–225, DOI 10.1046/j.0022-202x.2001.01670.x.
- [27] Ya-Chieh and Fuchs Hsu Elaine, *A family business: stem cell progeny join the niche to regulate homeostasis*, Nature reviews Molecular cell biology **13** (2012), no. 2, 103–114, DOI 10.1038/nrm3272.
- [28] Amélie and Wang Rezza Zichen and Sennett, *Signaling networks among stem cell precursors, transit-amplifying progenitors, and their niche in developing hair follicles*, Cell reports **14** (2016), no. 12, 3001–3018, DOI 10.1016/j.celrep.2016.02.078.
- [29] Holger and Turk Kulesa Gail and Hogan, *Inhibition of Bmp signaling affects growth and differentiation in the anagen hair follicle*, The EMBO journal **19** (2000), no. 24, 6664–6674, DOI 10.1093/emboj/19.24.6664.
- [30] Hiroshi and Ikeda Takahashi Tohru, *Transcripts for two members of the transforming growth factor- β superfamily BMP-3 and BMP-7 are expressed in developing rat embryos*, Developmental dynamics **207** (1996), no. 4, 439–449, DOI 10.1002/(SICI)1097-0177(199612)207:4<439::AID-AJA8>3.0.CO;2-I.
- [31] Chao-Chun and Cotsarelis Yang George, *Review of hair follicle dermal cells*, Journal of dermatological science **57** (2010), no. 1, 2–11, DOI 10.1016/j.jdermsci.2009.11.005.
- [32] Rachel and Rendl Sennett Michael, *Mesenchymal-epithelial interactions during hair follicle morphogenesis and cycling*, Seminars in cell & developmental biology, 2012, pp. 917–927, DOI 10.1016/j.semcd.2012.08.011.
- [33] Michael and Polak Rendl Lisa and Fuchs, *BMP signaling in dermal papilla cells is required for their hair follicle-inductive properties*, Genes & development **22** (2008), no. 4, 543–557, DOI 10.1101/gad.1614408.
- [34] Krzysztof and Pasolli Kobiela H Amalia and Alonso, *Defining BMP functions in the hair follicle by conditional ablation of BMP receptor IA*, The Journal of cell biology **163** (2003), no. 3, 609–623, DOI 10.1083/jcb.200309042.
- [35] Ryan R and Clavel Driskell Carlos and Rendl, *Hair follicle dermal papilla cells at a glance*, Journal of cell science **124** (2011), no. 8, 1179–1182, DOI 10.1242/jcs.082446.
- [36] Vladimir A and Kishimoto Botchkarev Jiro, *Molecular control of epithelial-mesenchymal interactions during hair follicle cycling*, Journal of Investigative Dermatology Symposium Proceedings, 2003, pp. 46–55, DOI 10.1046/j.1523-1747.2003.12171.x.

- [37] Vladimir A Botchkarev, *Bone morphogenetic proteins and their antagonists in skin and hair follicle biology*, Journal of Investigative Dermatology **120** (2003), no. 1, 36–47, DOI 10.1046/j.1523-1747.2003.12002.x.
- [38] Vladimir A and Botchkareva Botchkarev Natalia V and Roth, *Noggin is a mesenchymally derived stimulator of hair-follicle induction*, Nature cell biology **1** (1999), no. 3, 158–164, DOI 10.1038/11078.
- [39] M and Nanney Blessing LB and King, *Transgenic mice as a model to study the role of TGF-beta-related molecules in hair follicles.*, Genes & Development **7** (1993), no. 2, 204–215, DOI 10.1101/gad.7.2.204.
- [40] David and Kolligs Van Mater Frank T and Dlugosz, *Transient activation of β -catenin signaling in cutaneous keratinocytes is sufficient to trigger the active growth phase of the hair cycle in mice*, Genes & development **17** (2003), no. 10, 1219–1224.
- [41] Cristina Lo and Prowse Celso David M and Watt, *Transient activation of β -catenin signalling in adult mouse epidermis is sufficient to induce new hair follicles but continuous activation is required to maintain hair follicle tumours* (2004).
- [42] Haihua and Nan Zhang Weixiao and Wang, *Epidermal growth factor promotes proliferation and migration of follicular outer root sheath cells via Wnt/ β -catenin signaling*, Cellular Physiology and Biochemistry **39** (2016), no. 1, 360–370.
- [43] Valerie PI and Chaboissier Vidal Marie-Christine and Lützkendorf, *Sox9 is essential for outer root sheath differentiation and the formation of the hair stem cell compartment*, Current Biology **15** (2005), no. 15, 1340–1351.
- [44] Joerg and Vogel Huelsken Regina and Erdmann, *β -Catenin controls hair follicle morphogenesis and stem cell differentiation in the skin*, Cell **105** (2001), no. 4, 533–545.
- [45] KS and Lawrence Stenn Laura and Veis, *Expression of the bcl-2 protooncogene in the cycling adult mouse hair follicle*, Journal of Investigative Dermatology **103** (1994), no. 1, 107–111.
- [46] Kurt Stenn, *Growth of the hair follicle: a cycling and regenerating biological system*, Molecular basis of epithelial appendage morphogenesis (1998).
- [47] Albert M Kligman, *The human hair cycle*, Journal of Investigative Dermatology **33** (1959), no. 6, 307–316.
- [48] Paul F Parakkal, *Morphogenesis of the hair follicle during catagen*, Zeitschrift für Zellforschung und mikroskopische Anatomie **107** (1970), no. 2, 174–186.
- [49] Sven and Rossiter Müller-Röver Heidemarie and Paus, *Overexpression of Bcl-2 protects from ultraviolet B-induced apoptosis but promotes hair follicle regression and chemotherapy-induced alopecia*, The American journal of pathology **156** (2000), no. 4, 1395–1405.
- [50] R and Lindner Rückert G and Bulfone-Paus, *High-dose proinflammatory cytokines induce apoptosis of hair bulb keratinocytes in vivo*, British Journal of Dermatology **143** (2000), no. 5, 1036–1039.
- [51] KJ and Hunt Painter GS and Wells, *Towards an integrated experimental–theoretical approach for assessing the mechanistic basis of hair and feather morphogenesis*, Interface focus **2** (2012), no. 4, 433–450.
- [52] José and Bernard Halloy Bruno Alain and Loussouarn, *Modeling the dynamics of human hair cycles by a follicular automaton*, Proceedings of the National Academy of Sciences **97** (2000), no. 15, 8328–8333.
- [53] Maksim V and Baker Plikus Ruth E and Chen, *Self-organizing and stochastic behaviors during the regeneration of hair stem cells*, Science **332** (2011), no. 6029, 586–589.
- [54] Yusur and Goodfellow Al-Nuaimi Marc and Paus, *A prototypic mathematical model of the human hair cycle*, Journal of theoretical biology **310** (2012), 143–159.
- [55] Philip J and Maini Murray Philip K and Plikus, *Modelling hair follicle growth dynamics as an excitable medium*, PLoS computational biology **8** (2012), no. 12, e1002804.
- [56] Qixuan and Oh Wang Ji Won and Lee, *A multi-scale model for hair follicles reveals heterogeneous domains driving rapid spatiotemporal hair growth patterning*, Elife **6** (2017).
- [57] Wen-Yen and Lin Huang Edrick Tai-Yu and Hsu, *Anagen hair follicle repair: timely regenerative attempts from plastic extra-bulge epithelial cells*, Experimental dermatology **28** (2019), no. 4, 406–412.
- [58] M Shafayet and Harland Zamil Duane P and Fisher, *Biomechanics of hair fibre growth: A multi-scale modeling approach*, Journal of the Mechanics and Physics of Solids **148** (2021), 104290.

- [59] Nicholas and Sennett Heitman Rachel and Mok, *Dermal sheath contraction powers stem cell niche relocation during hair cycle regression*, *Science* **367** (2020), no. 6474, 161–166.
- [60] Pieter A and Heitman Martino Nicholas and Rendl, *The dermal sheath: An emerging component of the hair follicle stem cell niche*, *Experimental Dermatology* **30** (2021), no. 4, 512–521.
- [61] ZhiCao and Lei Yue Mingxing and Paus, *The global regulatory logic of organ regeneration: circuitry lessons from skin and its appendages*, *Biological Reviews* **96** (2021), no. 6, 2573–2583.
- [62] Iain S and Zhou Haslam GuiXuan and Xie, *Inhibition of Shh signaling through MAPK activation controls chemotherapy-induced alopecia*, *Journal of Investigative Dermatology* **141** (2021), no. 2, 334–344.
- [63] Simeone and Hogue Marino Ian B and Ray, *A methodology for performing global uncertainty and sensitivity analysis in systems biology*, *Journal of theoretical biology* **254** (2008), no. 1, 178–196.
- [64] Katherine Dinh and Qixuan Wang, *A probabilistic Boolean model on hair follicle cell fate regulation by TGF- β* , *Biophysical Journal* **121** (2022), no. 13, 2638–2652.
- [65] Shih-Fan and Huang Lai Wen-Yen and Wang, *Prostaglandin E2 prevents radiotherapy-induced alopecia by attenuating transit amplifying cell apoptosis through promoting G1 arrest*, *Journal of Dermatological Science* **109** (2023), no. 3, 117–126, DOI 10.1016/j.jdermsci.2023.02.005.
- [66] Cecilia and Barcenas Duran Manuel and Wang, *Modeling of ionizing radiation induced hair follicle regenerative dynamics*, *Journal of Theoretical Biology* **555** (2022), 111–283, DOI <https://doi.org/10.1016/j.jtbi.2022.111283>.

Part II

Autonomous Regulation can Produce Robust Polarization Pattern

Chapter 4

Introduction

Cell polarity, a fundamental aspect of cellular development, plays a pivotal role in a multitude of biological functions such as cell division, morphology, migration, and signaling. At the single-cellular level, it refers to the asymmetrical distribution of components or substances within a cell from an initially homogeneous distribution. The study of polarity establishment in cells is vital for unraveling the mechanisms underlying growth patterns, tissue differentiation, and environment interactions. Popular model organisms to study the polarization process include budding yeast, *Saccharomyces cerevisiae*, where polarization initiates the processes of budding and mating. The *Drosophila* wing disc is another prominent model used to study tissue development and growth regulation, processes which are strongly dependent on mechanical reactions to polarized chemical gradients. *Arabidopsis thaliana* is a plant organism whose leaf pavement cells (PCs) form multiple specialized molecule clusters along the cell membrane until shape-change is initiated and the cell terminally differentiates into its distinctive puzzle-piece shape.

These organisms are optimal models due to their genetic tractability and experimental accessibility. Furthermore many fundamental mechanisms and signaling pathways are conserved across other organisms, including humans for the case *S. cerevisiae* and *Drosophila*, and crops of agricultural importance for the case of *A. thaliana*. Thus understanding such

mechanisms can inform research on similar processes for higher organisms. In addition, it has now been experimentally shown that the polarized arrangement of molecular and structural components of the cell into one or multiple isolated high-concentration regions, activates a variety of chemical signals which intricately coordinate successive events like cell-shape change and cell division. The mating process of *S. cerevisiae*, in which the growth of a projection breaks the cellular symmetry as a response to sensing of a pheromone gradient, has been shown in [1,2] to be initiated by the rearrangement of the actin skeleton which then mediates transport of proteins and GTPases and directs the cell to localize the concentration of Cdc42 at a single location towards the direction of the pheromone. In [3], the development of the *Drosophila* wing is initiated at the single-cellular level by establishing and maintaining domains of multiple target genes as well as controlling the distribution of the small GTPase Rho1, activating regulatory mechanisms that later specify the different compartments of the adult tissue. In [4], polarization of the PCs of *A. thaliana* as a response to the phytohormone auxin begins by the accumulation of proteins and lipids into multiple clusters on the cell membrane, activating the ROP6 signaling pathway which then coordinates intracellular component arrangement towards the clustering site until cell-shape change is initiated.

Irrespective of the organism, it has now become standard to use mathematical modeling to complement experimental observations. In particular, the use of reaction-diffusion models to simulate polarization via signaling and regulatory mechanisms has now widely been adopted due to their high success in the study of pattern formation [5]. In this work, we study autoregulated reaction-diffusion models using three numerical methods for simulating polarization at a single cell membrane. In particular, we test various diffusion mechanisms in order to determine the role of positive and negative feedbacks in the early polarization process. We begin in the preliminaries section 4.1 by giving a brief mathematical background. We then describe the numerical methods in section 4.2 and present various preliminary simulation results to their performance, and assess which model mechanisms have potential to achieve polarization. In the results chapter, we focus on two selected models and proceed to systematically explore their respective parameter space to find regimes that can produce

polarization, as well as observe changes in each model's behaviors as parameters vary. We finish by giving our conclusions and discussion of future direction for this project.

4.1 Preliminaries

A single-component, or autonomous, reaction-diffusion system on a specified domain is a partial differential equation (PDE) of the form

$$u_t = \cdot (D\nabla u) + f(u, x, t)$$

where the solution $u(x, t)$ gives information about the concentration distribution over space and time. The first term on the right-hand side of the equation is the diffusion term, while the function f represents any number of reaction terms. In the diffusion term, if the diffusion coefficient is a constant D , then the diffusion rate is homogeneous across the domain and we can write the diffusion term as $D\Delta u$. If D is a function of x , the diffusion rate is spatially-dependent (SD) nonhomogenous; if D is a function of u , it is concentration-dependent (CD) nonhomogeneous.

Since we are interested in a diffusion process along a single cell membrane, we assume that the cell has circular shape and we take our domain to be the topologically equivalently one-dimensional interval $(0, 2\pi]$ with endpoints identified. This naturally implies periodic boundary conditions

$$u(0, t) = u(2\pi, t) \quad \forall t$$

$$u_x(0, t) = u_x(2\pi, t) \quad \forall t$$

We also point out that because of the domain equivalence, the diffusion operators involve the usual one-dimensional spatial derivatives $\Delta = \frac{\partial^2}{\partial x^2}$ and $\nabla = \frac{\partial}{\partial x}$. If the domain was any other non-circular closed curve, say parametrized by $(u(x), v(x))$, $x \in [0, L]$, one should use

the surface diffusion operator $\nabla_s(D\nabla_s) = \frac{1}{\eta} \frac{\partial}{\partial x} \left(D \frac{1}{\eta} \frac{\partial}{\partial x} \right)$, where $\eta = \sqrt{u_x^2 + v_x^2}$, where again, D can be either constant, SD or CD nonhomogeneous.

To solve the reaction-diffusion problem on the interval with periodic boundary conditions, we develop numerical models using Fourier spectral methods and compare their performance with a traditional finite difference model. More specifically, we use the central finite difference for derivative approximations; from Taylor's Theorem, if f is smooth in a neighborhood of x , and h is a mesh point in that neighborhood, then $f'(x) \approx \frac{f(x+h)-f(x-h)}{h}$ and $f''(x) \approx \frac{f(x+h)-2f(x)+f(x-h)}{h^2}$.

In contrast, Fourier spectral methods refer to a class of numerical algorithms which use the fast Fourier transform (FFT) to approximate derivatives. The Fourier transform takes functions of Euclidean time or space to functions of frequency in the Fourier domain. If f is a smooth function of $x \in \mathbb{R}$, the Fourier transform pair, meaning the Fourier transform of f and its inverse, is defined as

$$\hat{f}(k) = \mathcal{F}(f(x)) = \int_{-\infty}^{\infty} f(x)e^{-ikx} dk$$

$$f(x) = \mathcal{F}^{-1}(\hat{f}(k)) = \frac{1}{2\pi} \int_{-\infty}^{\infty} \hat{f}(k)e^{ikx} dk$$

The number $\hat{f}(k)$ can be interpreted as the amplitude of the density of f at the frequency or wavenumber k . One key property of the Fourier transform is how it interacts with the derivative operator. Specifically, obtaining the derivative of a function in the spatial domain corresponds to multiplying its Fourier transform by ik in the frequency domain and then

inverting:

$$\begin{aligned}
\mathcal{F}\left(\frac{d}{dx}f(x)\right) &= \int_{-\infty}^{\infty} f'(x)e^{-ikx} dx \\
&= \left[f(x)e^{-ikx}\right]_{-\infty}^{\infty} - \int_{-\infty}^{\infty} f(x)[-ike^{-ikx}] dx \\
&= ik \int_{-\infty}^{\infty} f(x)e^{-ikx} dx \\
&= ik\mathcal{F}(f(x)) \\
\implies \frac{d}{dx}f(x) &= \mathcal{F}^{-1}ik\mathcal{F}(f(x))
\end{aligned}$$

The order of the derivative is the number of factors of ik we must multiply by in the Fourier domain such as

$$\mathcal{F}\left(\frac{d^2}{dx^2}f(x)\right) = -k^2\mathcal{F}(f(x))$$

and so on. This is the basis of FFT-differentiation in the class of Fourier spectral methods.

In a discrete spatial domain, if $x_n = nh \in (0, 2\pi]$ for $n = 1, \dots, N$ and with $h = 2\pi/N$ where N is even, then the frequency domain is by convention the interval $(-\pi/h, \pi/h] = (-N/2, N/2]$. Then the discrete Fourier transform (DFT) pair is defined as

$$\hat{f}_k = h \sum_{n=1}^N f_n e^{-ikx_n}, \quad k = -N/2 + 1, -N/2 + 2, \dots, N/2$$

$$f_n = \frac{1}{2\pi} \sum_{k=-N/2+1}^{N/2} \hat{f}_k e^{ikx_n}, \quad n = 1, \dots, N$$

Given a vector of data $[f_1 \ f_2 \ \dots \ f_N]$, naively computing \hat{f} from the above definition is computationally expensive for large N , with $O(N^2)$ computations. However it is now standard to perform this operation by using the fast Fourier transform (FFT) algorithm which reduces the number of operations to $O(N \log N)$. Most computing software comes with a built-in FFT function and inverse; in this work, we use MATLAB to build our

numerical models and perform FFT-based differentiation which we describe in more detail in the next section. For a more detailed review of the Fourier transform and Fourier spectral methods, we refer the reader to [6, 7].

4.2 Numerical Methods

We develop three numerical models and compare simulations of various reaction-diffusion processes; two of the numerical models are developed using Fourier spectral methods, or FFT-based differentiation, and the third one is of finite difference type. Simultaneously, we aim to analyze what mechanisms contribute to cell polarization, in particular we are interested in the role of positive and negative feedbacks in the reaction-diffusion process. To begin, we take a diffusive molecule whose concentration is $u(x, t)$, bound in a circular cell membrane equivalent to the interval $(0, 2\pi]$ with endpoints identified and thus with periodic boundary conditions. Here, we let diffusion rates be either homogeneous with constant diffusion rate D , spatially-dependent (SD) nonhomogeneous, or concentration-dependent (CD) nonhomogeneous; the latter in the form of negative Hill-function feedback. More specifically, we will test the following diffusion terms in various reaction-diffusion models

- $D\Delta u = \frac{\partial^2}{\partial x^2} u$ with constant diffusion rate D .
- $\nabla(D(x)\nabla u) = \frac{\partial}{\partial x} (D(x) \frac{\partial}{\partial x} u) = \frac{d}{dx} D(x) \frac{\partial}{\partial x} u - D(x) \frac{\partial^2}{\partial x^2} u$, with SD diffusion rate of the form $D(x) = \sum_i d_i e^{\left(-\frac{x-\theta_i}{\sigma_i}\right)^2}$.
- $\nabla(D(u)\nabla u) = \frac{\partial}{\partial x} (D(u) \frac{\partial}{\partial x} u) = \frac{d}{du} D(u) \left(\frac{\partial}{\partial x} u\right)^2 - D(u) \frac{\partial^2}{\partial x^2} u$, with CD diffusion rate of the form $D(u) = D_{\min} + \frac{D_{\max} - D_{\min}}{1 + \left(\frac{u}{k_D}\right)^n}$.

using the three numerical methods. Each numerical method is different in the diffusion term approximation; method 1 and method 3 approximate the derivatives $u' \approx \frac{\partial}{\partial x} u$, $u'' \approx \frac{\partial^2}{\partial x^2} u$ so that switching to prime notation for derivatives, we have

- $\nabla(D(x)\nabla u) \approx D'(x)u' + Du'''$, for SD diffusion rate.
- $\nabla(D(u)\nabla u) \approx (D'(u)u')u' - D(u)u''$, for CD diffusion rate.

(all other derivatives in the above expression are analytically computed). The spatial interval $(0, 2\pi]$ is discretized into N equidistant nodes x_1, \dots, x_N with $N = 512$, $h = 2\pi/N$ so that $x_n = 2\pi n/N$. Method 1 uses FFT-based algorithms 1 and 2 from [8], and reiterated below

Algorithm 1 - First Derivative

Obtain the first derivative approximation $u' \approx u'_n = u'(n2\pi/L)$ from the discrete vector function $u_n = u(n2\pi/L)$

1. Use the fft MATLAB function to obtain the Fourier coefficients U_k , $0 < k \leq N$.
2. Multiply U_k by ik for $k < N/2$, by zero if $k = N/2$ and by $i(k - N)$ for $k > N/2$ to obtain U'_k .
3. Obtain u'_n by inverting U'_k via the inverse fft Matlab function (ifft).

Algorithm 2 - Second Derivative

Obtain the second derivative approximation $u'' \approx u''_n = u''(n2\pi/L)$ from the sampled function $u_n = u(n2\pi/L)$

1. Use the fft MATLAB function to obtain the Fourier coefficients U_k , $0 < k \leq N$.
2. Multiply U_k by $-k^2$ for $k \leq N/2$ and by $-(k - N)^2$ for $k > N/2$ to obtain U''_k .
3. Obtain u''_n by inverting U''_k via the inverse fft Matlab function (ifft).

Method 3 uses the central finite difference to approximate u' , and u'' . Method 2 is FFT-based but uses algorithm 4 in [8] to approximate the diffusion as

- $\nabla (D(x)\nabla u) \approx (D(x)u')'$, for SD diffusion rate.
- $\nabla (D(u)\nabla u) \approx (D(u)u')'$, for CD diffusion rate..

We also reiterate algorithm 4 below

Algorithm 4 - Position-varying Derivative Operator

Obtain the position-varying derivative approximation $(D(x)u')' \approx (Du'_n)' = (Du'(n2\pi/L))'$ from the sampled function $u_n = u(n2\pi/L)$

1. Use Algorithm 1 to compute u'_n , except set $U'_{k=N/2} = \frac{\pi i}{L} N U_{k=N/2}$ for N even.
2. Compute $v_n = Du'_n$ for $0 \leq n < N$.
3. Obtain $(Du'_n)'$ applying Algorithm 1 to v_n except set $V_{k=N/2} = \frac{\pi i}{L} N V_{k=N/2}$ for N even.

We use Gaussian initial conditions, that is, $u_0 = \sum_i c_i e^{-\left(\frac{x-\theta_i}{\sigma_i}\right)^2}$ for all our simulation tests presented below. We use the Euler temporal scheme with $dt = 1e^{-7}$. Simulation time is from $t = 0$ to $t = 1$, with evolution plotted at time points $t = 0, 0.1, 0.2, \dots, 0.9, 1$ over the interval $(0, 2\pi]$, with initial concentration u_0 in blue.

Simulation Tests

Spatially-dependent (SD) Nonhomogeneous Diffusion

$$\begin{aligned} u_t &= \nabla(D(x)\nabla u) \\ u_0 &= e^{-\frac{(x-\theta_1)^2}{\sigma^2}} + e^{-\frac{(x-\theta_2)^2}{\sigma^2}}, \quad \theta_1 = \frac{\pi}{4}, \quad \theta_2 = \frac{5\pi}{4}, \quad \sigma = 0.25 \\ D(x) &= 0.5 + e^{-\frac{(x-\theta_1)^2}{\sigma^2}} - 0.25e^{-\frac{(x-\theta_2)^2}{\sigma^2}} \end{aligned}$$

This diffusion rate is chosen to be faster near θ_1 and slower near θ_2 , with $D(\theta_1) = 1.5 > .25 = D(\theta_2)$, so it is expected that the concentration will diffuse faster near θ_1 than near θ_2 . This is confirmed in figure 4.1, where we observe that methods 1 and 2 yield similar results, while method 3 results in a more drastically fast diffusion near θ_1 . Successful polarization appears unlikely for either numerical method.

Concentration-dependent (CD) Nonhomogeneous Diffusion

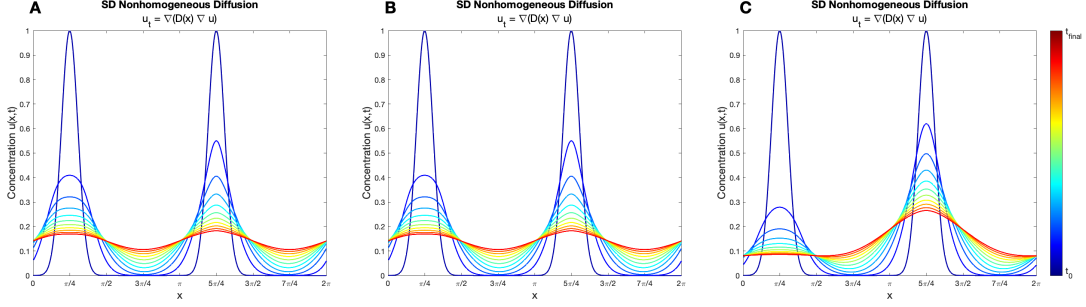


Figure 4.1: SD Nonhomogeneous Diffusion. Temporal evolution of u on $(0, 2\pi]$, that is the family of functions $\{u_t | t = 0, 0.1, 0.2, \dots, 1\}$. **A** Method 1. **B** Method 2. **C** Method 3.

$$\begin{aligned}
 u_t &= \nabla(D(u)\nabla u) \\
 u_0 &= e^{-\frac{(x-\theta)^2}{\sigma^2}}, \quad \theta = \frac{\pi}{4}, \quad \sigma = 0.25 \\
 D(u) &= D_{\min} + \frac{D_{\max} - D_{\min}}{1 + \left(\frac{u}{k_D}\right)^{n_D}}
 \end{aligned}$$

The diffusion rate in this model is a negative Hill-function feedback that indicates that u self-inhibits its diffusion depending on the parameter k_D . If at any time the concentration $u > k_D$, the diffusion inhibition mechanism is activated, and it is unactivated otherwise. More specifically, those locations in the domain where the concentration $u > k_D$ will have slower diffusion rate, and those locations where $u \leq k_D$ will have faster diffusion rate. The Hill exponent is fixed at $n_D = 15$ and we let the parameters $D_{\min} = 0.01$, $D_{\max} = 20$; this large choice of diffusion maximum reflects the fast-diffusing nature of biological substances at the molecular level. From figure 4.2, it seem plausible that this model may achieve polarization. The results for methods 1 and 2 are qualitatively similar in the shape of the polarization site, except that method 2 diffuses more quickly and also exhibits oscillatory behavior at the base of the polarization site, this is more noticeable at earlier times then appears to attenuate later. Method 3 also produces plausible polarizing results that are slightly qualitatively different in shape.

Next we add reaction terms to the previous models. We start by adding a constant production term M and linear degradation with rate d fixed at $d = 0.5$. Since degradation rates are difficult to measure experimentally, this choice is arbitrary.

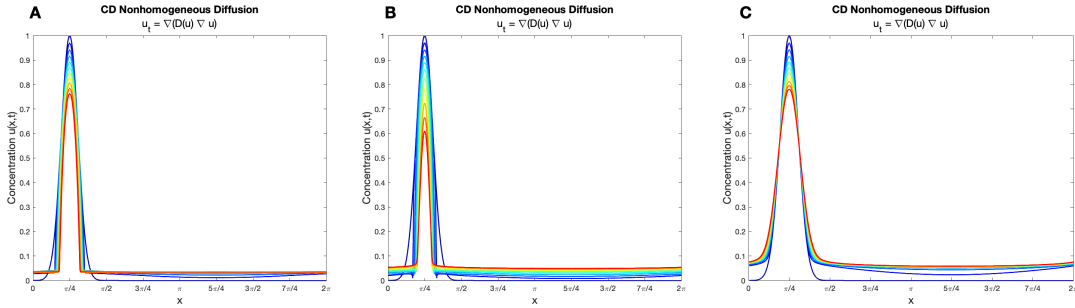


Figure 4.2: CD Nonhomogeneous Diffusion. Temporal evolution of u on $(0, 2\pi]$, that is the family of functions $\{u_t|t = 0, 0.1, 0.2, \dots, 1\}$. Diffusion-related parameters $k_D = 0.05$, $n_D = 15$, $D_{\min} = 0.01$, $D_{\max} = 20$. **A** Method 1. **B** Method 2. **C** Method 3.

SD Nonhomogeneous Diffusion with Constant Production and Linear Degradation

$$u_t = \nabla(D(x)\nabla u) + M - du$$

$$u_0 = e^{-\frac{(x-\theta_1)^2}{\sigma^2}} + e^{-\frac{(x-\theta_2)^2}{\sigma^2}}, \quad \theta_1 = \frac{\pi}{4}, \quad \theta_2 = \frac{5\pi}{4}, \quad \sigma = 0.25$$

$$D(x) = 0.5 + e^{-\frac{(x-\theta_1)^2}{\sigma^2}} - 0.25e^{-\frac{(x-\theta_2)^2}{\sigma^2}}$$

The diffusion rate here is the same as in the first case. This model also seems unlikely to achieve polarization as can be seen in figure 4.3 below.

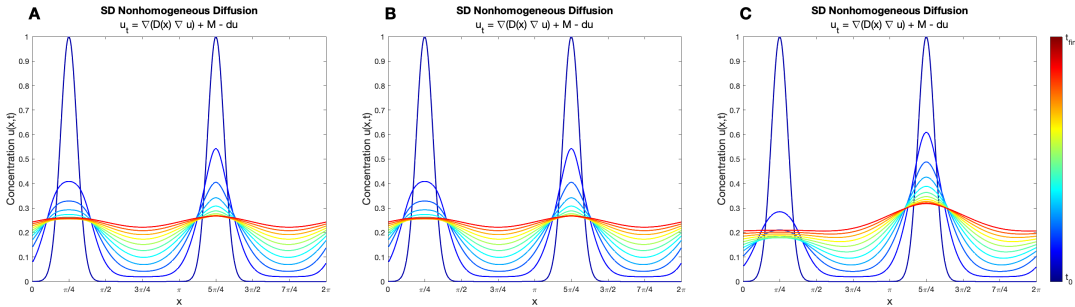


Figure 4.3: SD Nonhomogeneous Diffusion, Constant Production, Linear Degradation. Temporal evolution of u on $(0, 2\pi]$, that is the family of functions $\{u_t|t = 0, 0.1, 0.2, \dots, 1\}$. Parameter values $M = 0.2$, degradation $d = 0.5$. **A** Method 1. **B** Method 2. **C** Method 3.

CD Nonhomogeneous Diffusion with Constant Production and Linear Degradation

$$\begin{aligned}
 u_t &= \nabla(D(u)\nabla u) + M - du \\
 u_0 &= e^{-\frac{(x-\theta)^2}{\sigma^2}}, \quad \sigma = 0.25 \\
 D(u) &= D_{\min} + \frac{D_{\max} - D_{\min}}{1 + \left(\frac{u}{k_D}\right)^{n_D}}
 \end{aligned}$$

This model has the same Hill-function feedback as the second case. Here, from figure 4.4 we see that method 2 and method 3 yield similar results at the end of simulation time; at earlier times the solutions differ moderately with method 2 again exhibiting oscillatory behavior. Method 1 yields an artificial polarization site that is not observed in the other two methods. Overall, polarization seems plausible for this model and will be investigated further.

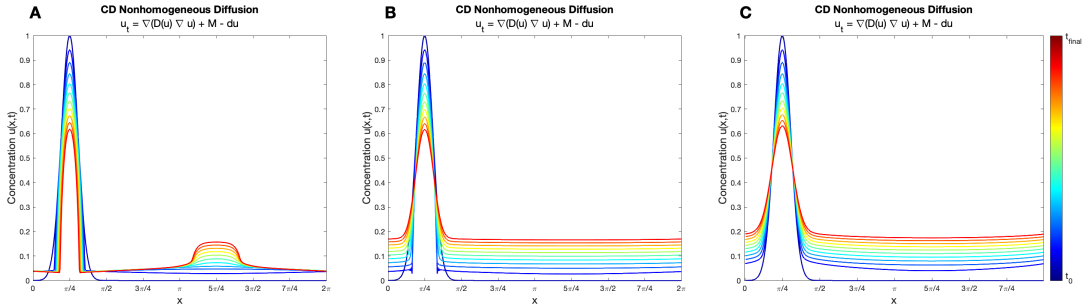


Figure 4.4: CD Nonhomogeneous Diffusion, Constant Production, Linear Degradation. Temporal evolution of u on $(0, 2\pi]$, that is the family of functions $\{u_t | t = 0, 0.1, 0.2, \dots, 1\}$. Parameter values $M = 0.2$, degradation $d = 0.5$. Diffusion-related parameters $k_D = 0.05$, $n_D = 15$, $D_{\min} = 0.01$, $D_{\max} = 20$. **A** Method 1. **B** Method 2. **C** Method 3.

For now we proceed to further modify the production term by letting f be a positive Hill-function feedback, M now denotes the magnitude of the production feedback; additional production feedback parameters are set to $k_f = 0.15$ and $n_f = 15$. The production feedback works similarly to the diffusion feedback. Any time the $u > k_D$, production is activated, and is unactivated otherwise. This means that those locations where $u > k_D$ will have greater production than where $u \leq k_D$. The role of this feedback is of high interest; we'd like to know whether positive production feedback alone can generate polarity, thus we also perform a simulation test for the case of homogeneous diffusion with constant rate D . We also point out that in this case, we only perform methods 1 and 3.

Homogeneous Diffusion with Positive Production Feedback and Linear Degradation

$$u_t = D\Delta u + M \left(\frac{1}{1 + \left(\frac{u}{k_f}\right)^{n_f}} \right) - du$$

$$u_0 = e^{-\frac{(x-\theta)^2}{\sigma^2}}, \quad \theta = \frac{\pi}{4}, \quad \sigma = 0.25$$

Figure 4.5 shows that both methods 1 and 3 produce indistinguishable results for this model, which are unlikely to polarize. This means that a production feedback mechanism alone is not sufficient for polarization in a reaction-diffusion model.

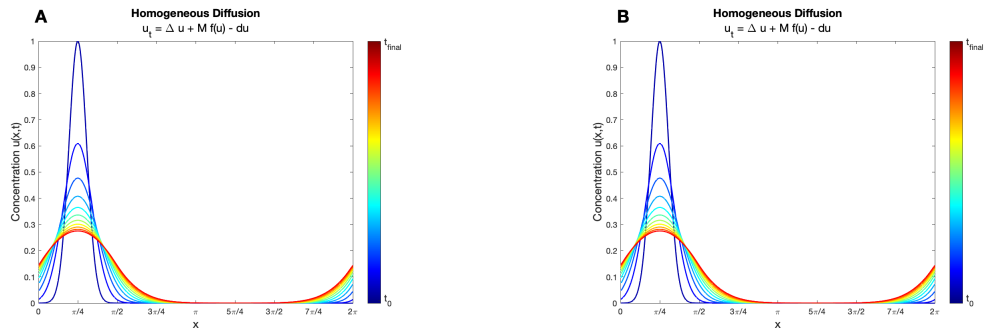


Figure 4.5: Homogeneous Diffusion, Positive Production Feedback, Linear Degradation. Temporal evolution of u on $(0, 2\pi]$, that is the family of functions $\{u_t|t = 0, 0.1, 0.2, \dots, 1\}$. Parameter values $M = 0.2$, degradation $d = 0.5$. Diffusion-related parameters $k_D = 0.05$, $n_D = 15$, $D_{\min} = 0.01$, $D_{\max} = 20$. Production feedback parameters $k_f = 0.15$, $n_f = 15$. **A** Method 1. **B** Method 3.

SD Nonhomogeneous Diffusion with Positive Production Feedback and Linear Degradation

$$u_t = \nabla(D(x)\nabla u) + M \left(\frac{1}{1 + \left(\frac{u}{k_f}\right)^{n_f}} \right) - du$$

$$u_0 = e^{-\frac{(x-\theta_1)^2}{\sigma^2}} + e^{-\frac{(x-\theta_2)^2}{\sigma^2}}, \quad \theta_1 = \frac{\pi}{4}, \quad \theta_2 = \frac{5\pi}{4}, \quad \sigma = 0.25$$

$$D(x) = 0.5 + e^{-\frac{(x-\theta_1)^2}{\sigma^2}} - 0.25e^{-\frac{(x-\theta_2)^2}{\sigma^2}}$$

Again, the diffusion rate here works the same as the respective previous cases, while the production term has a positive Hill-function feedback. Simulation results in figure 4.6 show that it is unlikely that polarization can be attained.

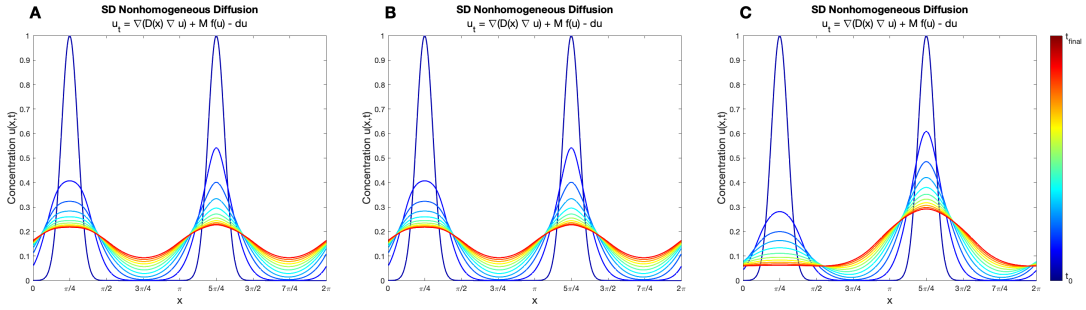


Figure 4.6: SD Nonhomogeneous Diffusion, Production Feedback, Linear Degradation. Temporal evolution of u on $(0, 2\pi]$, that is the family of functions $\{u_t | t = 0, 0.1, 0.2, \dots, 1\}$. Parameter values $M = 0.2$, degradation $d = 0.5$. Production feedback parameters $k_f = 0.15$, $n_f = 15$. **A** Method 1. **B** Method 2. **C** Method 3.

CD Nonhomogeneous Diffusion with Positive Production Feedback and Linear Degradation

$$u_t = \nabla(D(u)\nabla u) + M \left(\frac{1}{1 + \left(\frac{u}{k_f}\right)^{n_f}} \right) - du$$

$$u_0 = e^{-\frac{(x-\theta)^2}{\sigma^2}}, \quad \theta = \frac{\pi}{4}, \quad \sigma = 0.25$$

$$D(u) = D_{\min} + \frac{D_{\max} - D_{\min}}{1 + \left(\frac{u}{k_D}\right)^{n_D}}$$

The simulation results in figure 4.7 show the three methods give slightly different results. Methods 1 and 2 have the polarization site conserve a similar shape as it diffuses, although

method 2 shows faster diffusion and oscillatory behavior at early times. The polarization site for method 3 is slightly qualitatively different in shape. In all cases the results seem promising so we will continue to study this model in the next chapter.

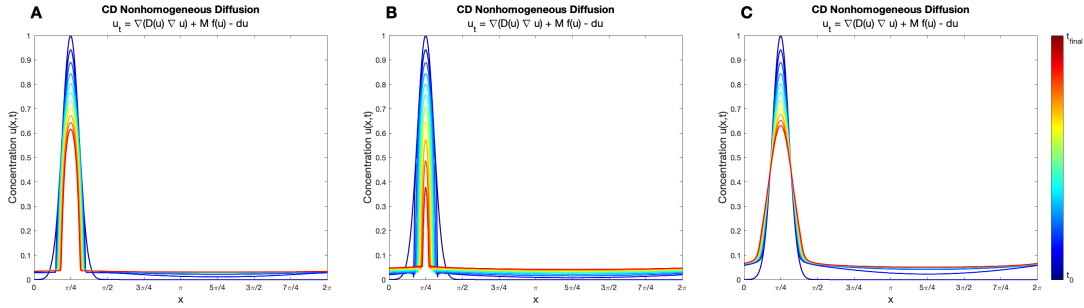


Figure 4.7: CD Nonhomogeneous Diffusion, Production Feedback, Linear Degradation. Temporal evolution of u on $(0, 2\pi]$, that is the family of functions $\{u_t|t = 0, 0.1, 0.2, \dots, 1\}$. Parameter values $M = 0.2$, degradation $d = 0.5$. Diffusion-related parameters $k_D = 0.05$, $n_D = 15$, $D_{\min} = 0.01$, $D_{\max} = 20$. Production feedback parameters $k_f = 0.15$, $n_f = 15$. **A** Method 1. **B** Method 2. **C** Method 3.

From these preliminary simulation tests we learn that some mechanisms are unlikely to result in a polarized concentration. The reaction-diffusion models with CD nonhomogeneous diffusion, constant production and linear degradation and with CD nonhomogeneous diffusion, positive production feedback and linear degradation are selected for further study. We describe the methodology in the following section.

4.3 Methodology

Testing different reaction-diffusion mechanisms allowed us to assess the role of positive and negative feedbacks in the polarization process. For the remainder of this work, we select two promising reaction-diffusion models from the previous section, which we refer to as model 1 and model 2 from this point forward.

- Model 1. $u_t = \nabla \cdot (D(u)\nabla u) + M - du$
- Model 2. $u_t = \nabla \cdot (D(u)\nabla u) + Mf(u) - du$

Both models have negative feedback in the diffusion $D(u) = D_{\min} + \frac{D_{\max} - D_{\min}}{1 + \left(\frac{u}{k_D}\right)^{n_D}}$ which has a self-inhibiting effect. Model 2 has an additional positive feedback in the production term $f(u) = \frac{1}{1 + \left(\frac{u}{k_f}\right)^{-n_f}}$, while model 1 has constant production M . The feedbacks work in the following way; the diffusion rate is a Hill function such that diffusion is slower in those regions x where the concentration $u(x, t) > k_D$ (the diffusion inhibition mechanism is activated), diffusion is faster in those regions x where the concentration $u(x, t) \leq k_D$ (the diffusion inhibition mechanism is unactivated). The positive production feedback in Model 2 is a Hill function that works similarly; the production is greater in those regions x where the concentration $u(x, t) > k_D$ (the production mechanism is activated), and production is lower in those regions x where the concentration $u(x, t) \leq k_D$ (the production mechanism is unactivated).

To investigate the extent to which these feedback mechanisms contribute to the polarization process, we first modify the initial condition by introducing white noise. Instead of initial Gaussian curves which already consist of high-concentration regions, we use randomized initial conditions of the form $u_0 = c_0 + \varepsilon c_0 \chi$ with $c_0 = 0.25$, $\varepsilon = 0.5$ and $\chi \sim N(0, 1)$ as seen in figure 4.8.

We'd also like to continue to compare the performance of the three numerical methods described earlier. However since this is currently ongoing work, in this thesis we only present our analysis for numerical method 1. Similar analyses will be performed for all methods for any potential upcoming publications.

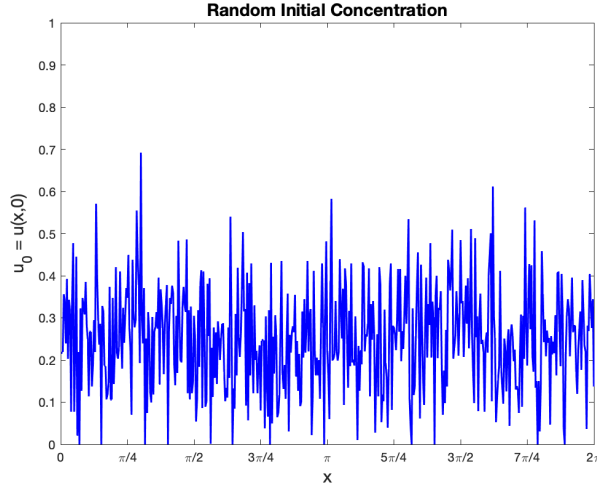


Figure 4.8: Random initial concentration. $u_0 = c_0 + \varepsilon c_0 \chi$, $c_0 = 0.25$, $\varepsilon = 0.5$, $\chi \sim N(0, 1)$

We proceed to study reaction-diffusion models 1 and 2 using numerical method 1, by assessing simulation results as parameters are varied. That is, we systematically run simulations with random initial conditions over their respective parameter space. The varying-parameter space for model 1 is $\{(M, k_D) \mid M = 0.2, 0.4, 0.6, 0.8, 1, 1.2 \text{ and } k_D = 0.02, 0.03, \dots, 0.07\}$, while for model 2 it is $\{(M, k_D, k_f) \mid M = 0.4, 0.6, 0.8, 1, k_D = 0.03, 0.04, 0.05, 0.06, \text{ and } k_f = 0.1, 0.15, 0.2, 0.25\}$.

For each model and for each parameter point we run ten sample simulations. The simulation time interval is $[0, 10]$. We would like to know if simulations with random initial concentrations can be successful at achieving and maintaining polarization; by maintaining we mean that steady state of the reaction-diffusion process is reached and the final concentration profile exhibits a pattern of isolated high-concentration regions. To make this assessment, we produce video simulations where, in the time interval $[0, 1]$ we save and plot data more frequently at times $t = 0, 0.1, 0.2, \dots, 0.9, 1$ since the diffusion process initiates immediately and quickly, while for the time interval $(1, 10]$ data is saved and plotted at every integer t i.e. $t = 2, 3, 4, \dots, 10$. We then make the assumption that simulations reach steady state if the concentration profile does not exhibit significant qualitative change in the last three time units $t = 8, 9, 10$.

Simulations results presented in this thesis will consist of final concentration simulation results, meaning the concentration $u(x, t_{final}) = u(x, 10)$. The data collected for each simulation is the number of polarization sites of the concentration profile of $u_{t_{final}}$, and each of their height and their width. We will often refer to $u_{t_{final}}$ simply as u for brevity, unless emphasizing is needed. The height of a polarization site refers to the respective local max of the concentration profile; the width of a polarization site refers to the distance from the left and the right of the peak where u intersects the horizontal line passing through the corresponding peak's half-height value. This data is then used to compute the average μ and coefficient of variation σ/μ of each property at each parameter point, and they are then plotted as heatmaps over the parameter space. In the next chapter, we describe each model's results by analyzing simulation data and dividing the parameter space into zones characterized by distinct qualitative behavior.

Chapter 5

Results

In this chapter, we investigate model 1 and model 2 using numerical method 1 in the way just described in section 4.3. We systematically explore the parameter space for each model to find regimes where polarization can be achieved and maintained, as well as to assess parameter sensitivity and robustness.

We point out that most simulations reach a steady state by the temporal choice $t_{\text{final}} = 10$, however some parameter sets produce simulations where it is not evident that steady state has been reached. Regardless of this, any such simulation that renders distinguishable polarization sites at the end of simulation is measured and included in the computed averages and coefficients of variation of each property.

5.1 Model 1

The first model we study is

$$u_t = \nabla_s (D(u)\nabla_s u) + M - du$$

where

$$D(u) = D_{min} + \frac{D_{max} - D_{min}}{1 + \left(\frac{u}{k_D}\right)^{n_D}}$$

This model features a CD nonhomogeneous diffusion rate that is self-inhibiting, constant production M and linear degradation du .

The varying parameters in this model are k_D in the diffusion rate and M in the production term, so that the parameter space explored is $\{(M, k_D) \mid M = 0.2, 0.4, 0.6, 0.8, 1, 1.2 \text{ and } k_D = 0.02, 0.03, \dots, 0.07\}$. The other model parameters are fixed at the values $D_{max} = 20$, $D_{min} = 0.01$, $n_D = 15$ and $d = 0.5$. We use random initial condition for each simulation $u_0 = c_0 + \epsilon c_0 \chi$, $c_0 = 0.25$, $\epsilon = 0.5$, $\chi \sim N(0, 1)$.

In what follows, we proceed to examine the average and coefficient of variation heatmaps for the number of polarization sites. In figure 5.1, the left map displays the average value at each parameter point, furthermore, some cells also display a percentage quantity which represents the proportion of *successful* simulation results, meaning those simulations that both reach steady state *and* yield polarization. In figure ??, the parameter space is divided into zones that separate different qualitative behaviors observed in simulations, which we will describe momentarily.

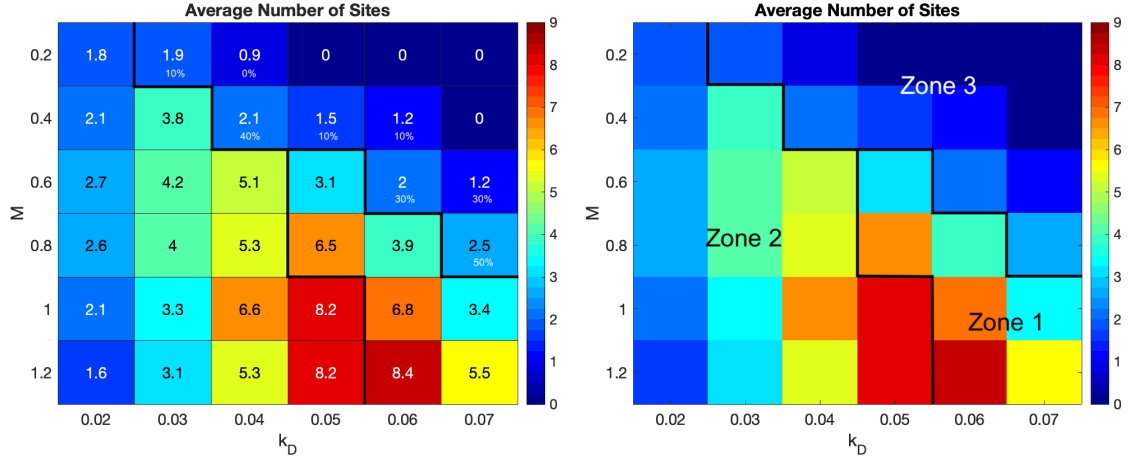


Figure 5.1: Model 1. Average number of polarization sites heatmaps. (Left) Average (μ) number of polarization sites with percentages in zone 3 cells representing the proportion of successful simulations; all other cells have a success rate of 70% or higher. (Right) Heatmap zone designation.

We first describe the general trend along the horizontal and vertical directions of the parameter space. From figure 5.1, we can observe that for $k_D < 0.05$ and as the production M increases, there's an increasing then decreasing trend in the average number of polarization sites, whereas in the case of $k_D \geq 0.05$, the trend is only increasing. However, it may be possible that a decreasing trend eventually occurs if the parameter space is extended to further values of M . On the other hand, fixing a production value M while increasing k_D produces a trend of increase then decrease in average number of polarization sites, which is amplified with M .

We now proceed to describe the different zones and the behavior that characterize them, we illustrate by including some simulation results. We identify zone 1 in the parameter space as the main region that is successful in maintaining polarization and the resulting polarized concentration has the right attributes. It is surrounded by zone 2 on the left and zone 3 to the upper right side. We choose a parameter point in zone 1 to show some sample simulation results (see figure 5.2).

In zone 2, simulations reach steady state however they fail to produce polarization sites that are sufficiently spatially isolated. Simulations for parameter values in the left-most part of this zone render low number of large polarization sites in very close proximity. On

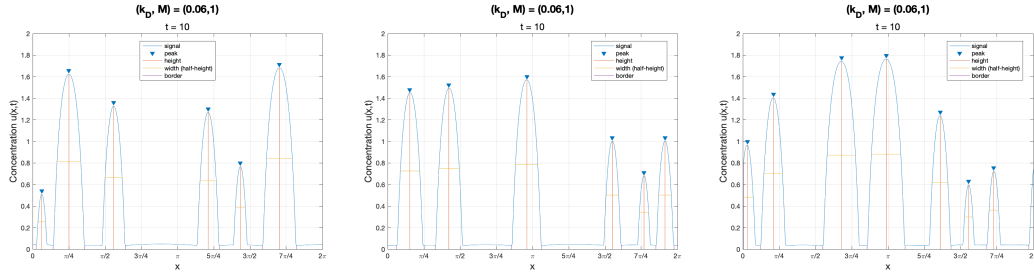


Figure 5.2: *Model 1, zone 1 simulation results* Sample simulations for parameter pair $(k_D, M) = (0.06, 1)$.

the other hand, the region of zone 2 that has higher average number still renders very close polarization sites and the domain is overcrowded with both large and small polarization sites; thus results in zone 2 are not considered optimal. We choose a parameter point in zone 2 to show some sample simulation results (see figure 5.3). Despite the outcome, the simulation results in zone 2 are not physically unreasonable since a low k_D value implies larger domain regions with low diffusion rate, or a "stronger" diffusion-inhibition effect which helps establish large polarization sites early on.

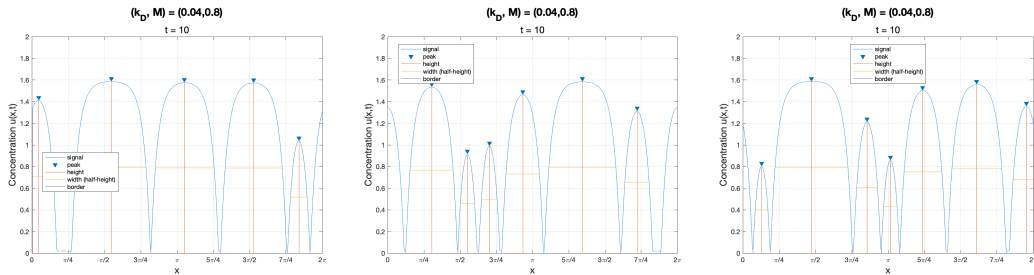


Figure 5.3: *Model 1, zone 2 simulation results* Sample simulations for parameter pair $(k_D, M) = (0.04, 0.8)$.

On the other hand, zone 3 is characterized by a low success rate in reaching steady state or in maintaining polarization. More specifically, the boundary between zone 3 and zone 1 is defined in a way that if the percent of successful simulations is larger than 70%, the parameter point belongs to zone 1, otherwise it belongs to zone 3, and similarly for the boundary between zone 3 and zone 2. Notice that this does not imply zone 3 is incapable of maintaining polarization; boundary values with higher percent success rate are sometimes able to produce good results, however, as parameter values move away from the boundary, simulations yield polarization sites of irregular shapes and the ability to produce steady state, polarized concentration decreases. Despite these irregularities in polarization site shape, those final concentration profiles that rendered "measurable" polarization sites are still included in our statistics calculations. In upper-right-most region of the parameter space, where the average of number of polarization sites is zero, polarization fails to be attained and the final concentration is high everywhere and tending towards the value M/d . Due to weak production and weak diffusion-inhibition effect, any early polarization attempt is lost as the concentration diffuses to a uniform level just above the value of k_D . At some further time, the concentration surpasses k_D in the entirety of the domain, this completely stops any further diffusion and the constant production causes the concentration to steadily increase toward M/d . We choose a parameter point in zone 3 to show some sample simulation results (see figure 5.4).

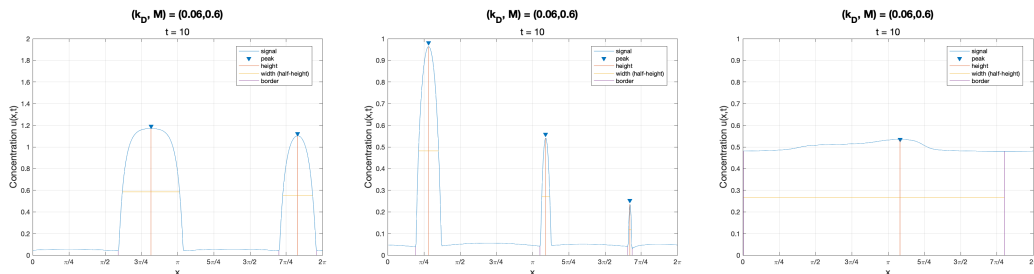


Figure 5.4: *Model 1, zone 3 simulation results* Sample simulations for parameter pair $(k_D, M) = (0.06, 0.6)$.

Comparing the behavior of zone 3 and zone 1 reveals that there's an intricate relationship between parameters k_D and M , more specifically, increasing the production M tends to stabilize the polarization process, and the larger k_D is, the larger M has to be as well.

Overall, the results for model 1 suggest that the polarization process strongly depends on the diffusion-inhibition feedback mechanism.

We present all other heatmaps in section 5.3 at the end of this chapter and compare results with model 2.

5.2 Model 2

The second model we investigate is

$$u_t = \nabla_s (D(u)\nabla_s u) + Mf(u) - du$$

where

$$D(u) = D_{min} + \frac{D_{max} - D_{min}}{1 + \left(\frac{u}{k_D}\right)^{n_D}}, \text{ and } f(u) = \left(\frac{1}{1 + \left(\frac{u}{k_f}\right)^{-n_f}} \right)$$

This model features the same CD nonhomogeneous diffusion rate as model 1, but also a positive feedback mechanism in the production term, and linear degradation du . We point out that model 1 is the limit of model 2 as $k_f \rightarrow 0$, thus for low values of k_f we expect similar results to model 1.

The varying parameters for model 2 are k_D , M and k_f , so that the parameter space explored is $\{(k_D, M, k_f)\}$ where $k_D = 0.03, 0.04, 0.05, 0.06$, $M = 0.4, 0.6, 0.8, 1$ and $k_f = 0.1, 0.15, 0.2, 0.25$. Similar to model 1, remaining parameters are fixed at the values $D_{max} = 20$, $D_{min} = 0.01$, $n_D = 15$, $n_f = 15$, $d = 0.5$. To make the description of model 2 results similar to model 1, we plot heatmaps over the $\{(k_D, M)\}$ parameter space for each fixed value of k_f , which are slices of the three-dimensional model 2 parameter space. Notice that we reduce the size of the parameter space in the k_D and M dimensions due to the computational expense of having two feedback mechanisms and having an additional parameter dimension

with k_f . Nonetheless, we believe we will still be able to capture optimal polarization results for model 2.

Same as before, we initiate ten sample simulations for each parameter set using random initial conditions of the form $u_0 = c_0 + \epsilon c_0 \chi$, $c_0 = 0.25$, $\epsilon = 0.5$, $\chi \sim N(0, 1)$. Each slice is divided into zones that separate different qualitative simulation behaviors in terms of the average number of polarization sites, similar to the classification of model 1. Figure 5.5 shows the heatmaps for the average number of polarization sites, with those cells displaying a percent quantity also indicating the proportion of successful polarization, i.e. simulations reaching steady state and polarized concentration profile.

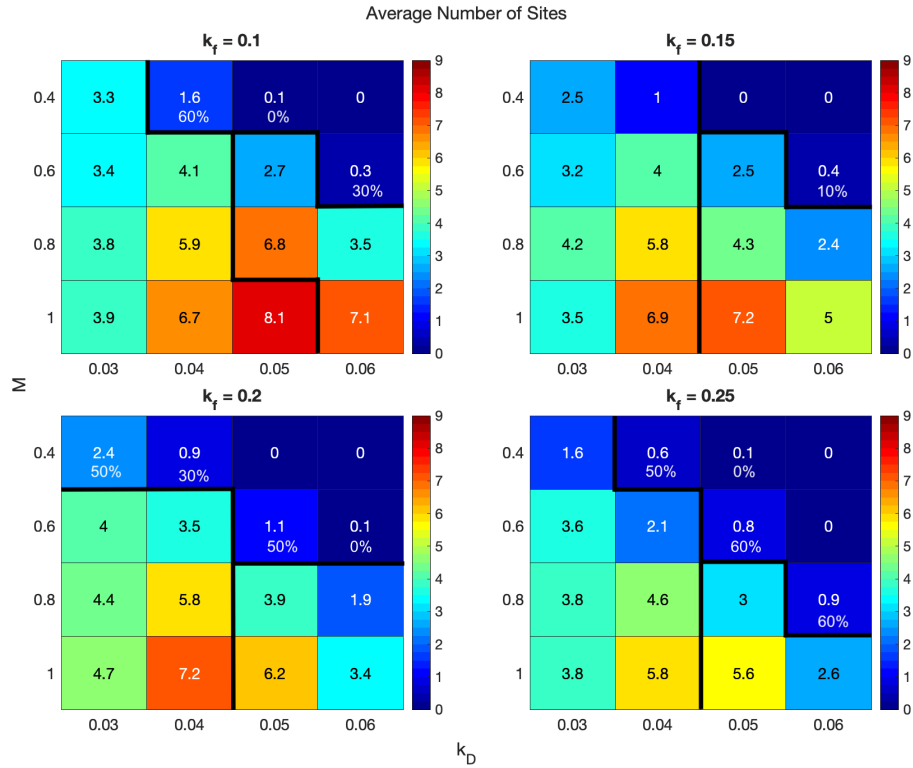


Figure 5.5: Model 2 Average number of polarization sites heatmaps. Each heatmap is a slice of the parameters space for different values of k_f , with the average value (μ) displayed in each cell. Percentages in zone 3 cells represent the proportion of successful simulations, all other cells have a success rate of 70% or higher.

Zone 1 is the bottom-right region in all parameter space slices and is the region that produces the most optimal results. We include simulation samples in this zone for low and high k_f values in figure 5.6.

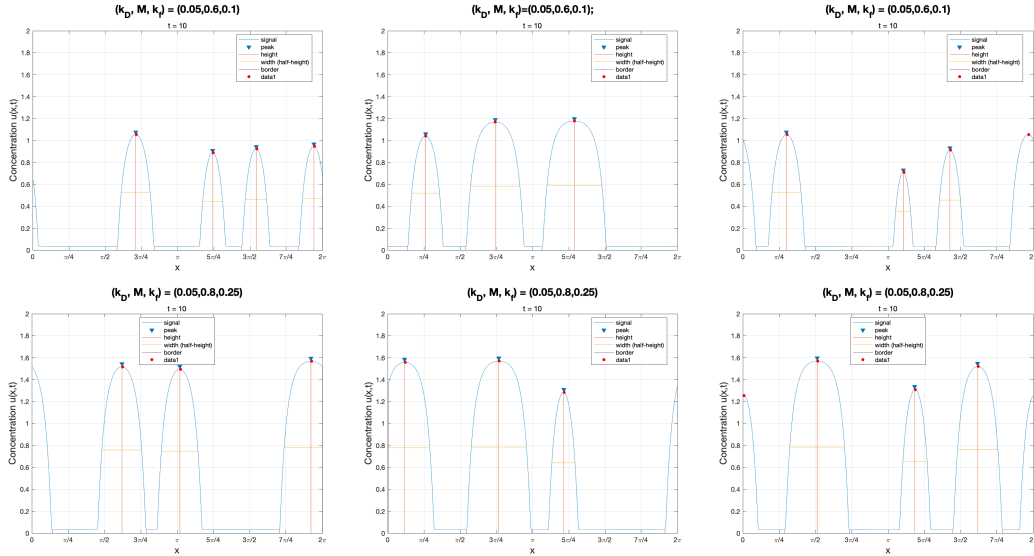


Figure 5.6: *Model 2, zone 1 simulation samples for low and high k_f . Simulation results for parameter points $(k_D, M, k_f) = (0.05, 0.6, 0.1)$ and $(k_D, M, k_f) = (0.05, 0.8, 0.25)$*

Zone 2 behavior is also similar to zone 2 in model 1. That is, for any fixed k_f , zone 2 produces either large polarization sites or a combination of small and large polarization sites that cover almost the entire domain. The boundary is defined similarly as before, meaning that simulations in this zone reach steady state with 70% success rate or higher. Furthermore, the size of polarization sites increases with M . One difference between the slices is that as k_f increases, the proximity of polarization sites decreases. When k_f is low, the simulation results are very similar to model 1, while for high k_f value, simulations yield polarization sites that have larger low-concentration regions that separate them. We illustrate this by including simulation samples for low and high k_f values where the average number of polarization sites is comparable (figure 5.7).

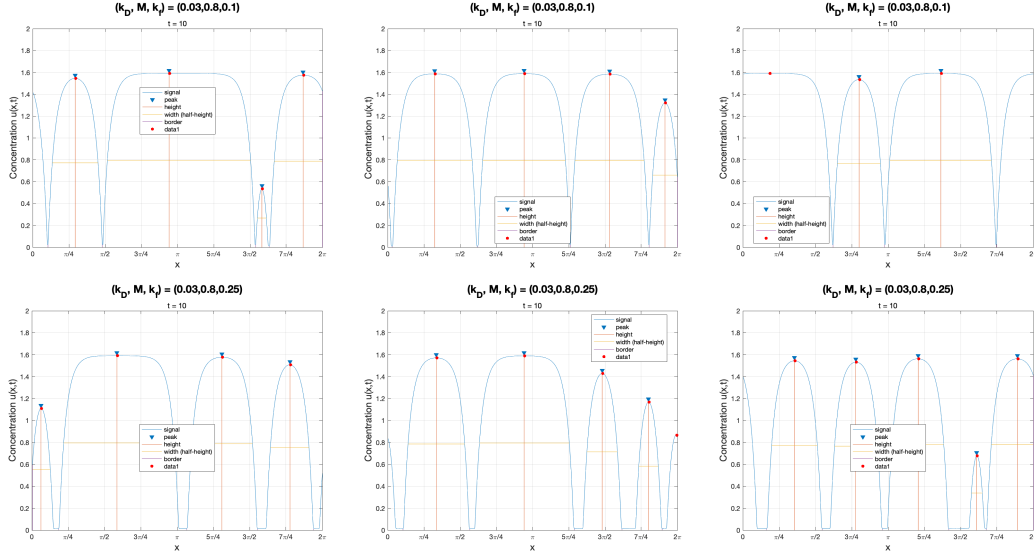


Figure 5.7: *Model 2, zone 2 simulation samples for low and high k_f . Simulation results for parameter points $(k_D, M, k_f) = (0.03, 0.8, 0.1)$ and $(k_D, M, k_f) = (0.03, 0.8, 0.25)$*

Zone 3 for this model is also characterized by none to low average number of polarization sites, with low rate of successful polarization. We note that this zone has transitioned inward in the parameter space for model 2. We also note that unsuccessful polarization simulations here render near-zero concentration everywhere in the domain, this contrasts with the same zone in model 1, where unsuccessful polarization simulations rendered high concentration everywhere, approaching the value M/d .

Overall, the results for model 2 suggest that the positive production feedback mechanism may help improve the polarization process by increasing the size of the separating low-concentration regions in the domain, this effect is most noticeable in zone 2. Comparing the zones among the k_f slices of the parameter space, we observe that the optimal zone 1 increases in size then decreases again, with the slice of $k_f = 0.15$ having the largest optimal region. We also report that the two feedback mechanisms result in significantly longer simulation times, compared with model 1.

We present all other heatmaps in section 5.3 below and compare results with model 1.

5.3 Model 1 and Model 2 Comparison

In this section we present the heatmaps for model 1 against those for model 2 for comparison. All heatmaps contain their respective zone outline, where the zones represent different qualitative behavior observed in simulations as described above. From just the heatmaps alone it is uncertain whether one model is superior or more robust than the other.

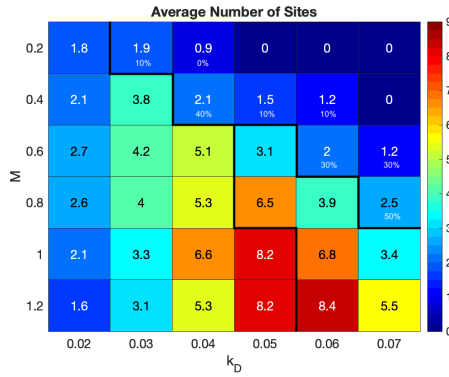


Figure 5.8: *Model 1 average number of polarization sites.*

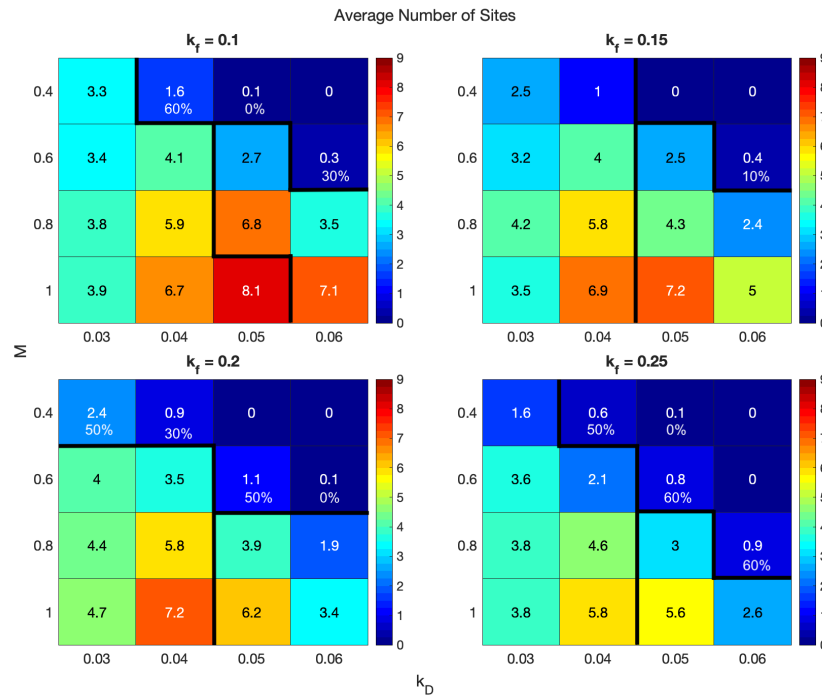


Figure 5.9: *Model 2 average number of polarization sites.*

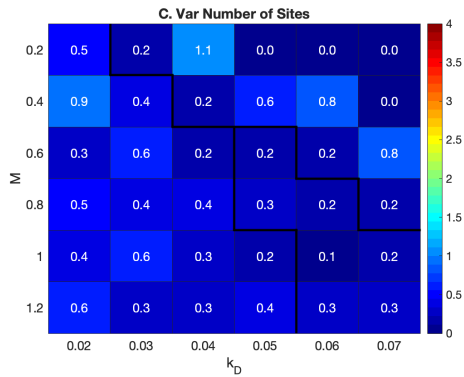


Figure 5.10: *Model 1 coefficient of variation of number of polarization sites.*

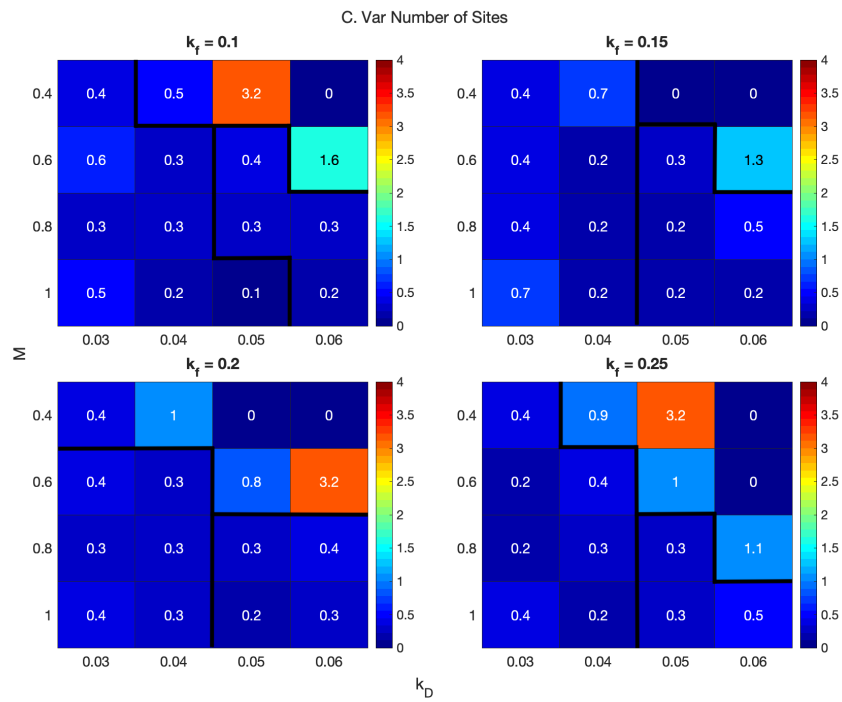


Figure 5.11: *Model 2 coefficient of variation of number of polarization sites.*

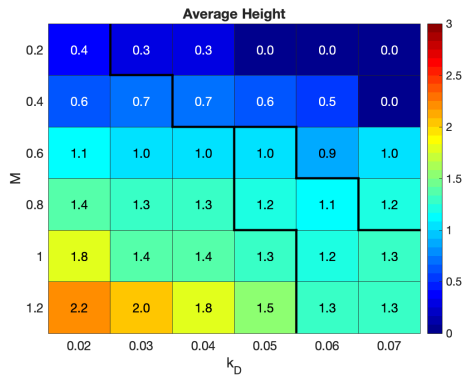


Figure 5.12: Model 1 average height of polarization sites.

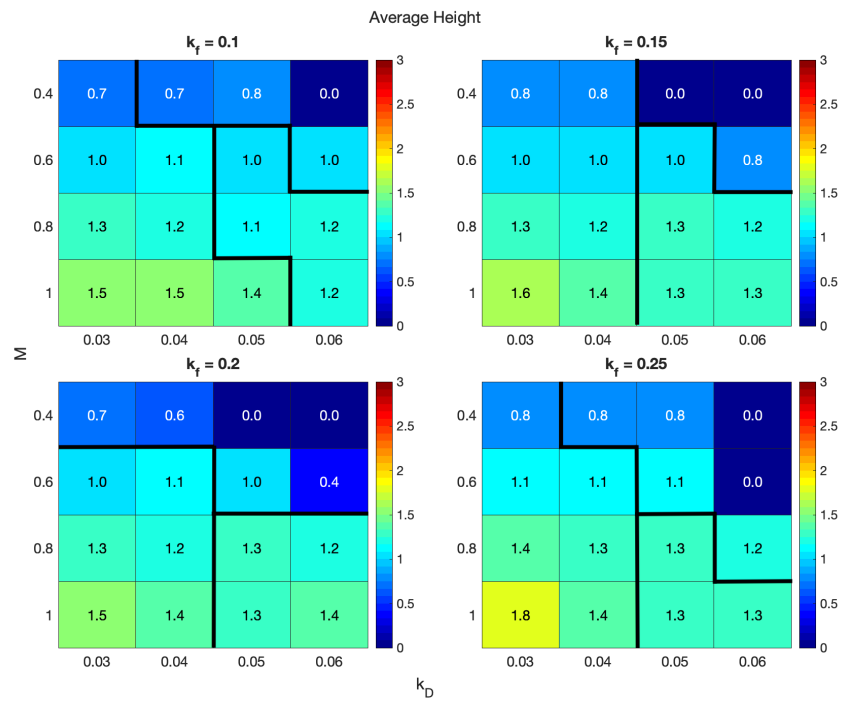


Figure 5.13: Model 2 average height of polarization sites

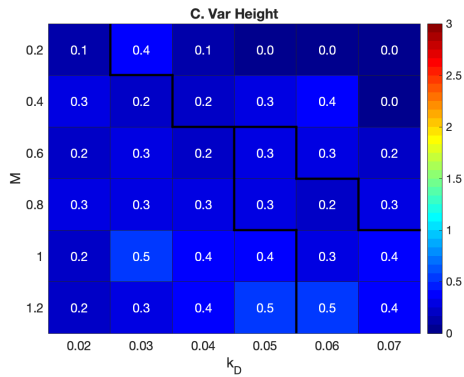


Figure 5.14: *Model 1 coefficient of variation of height of polarization sites.*

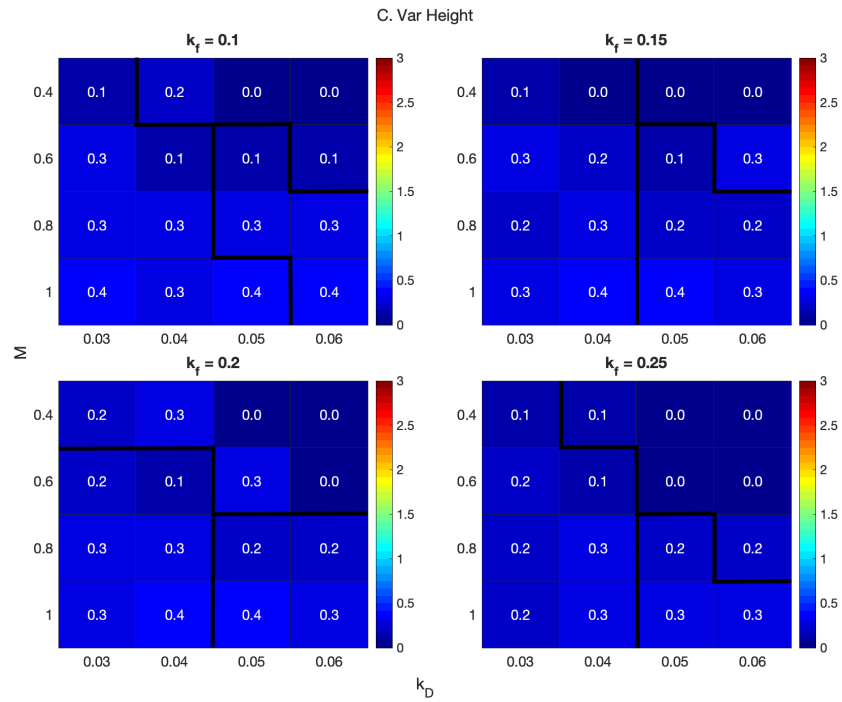


Figure 5.15: *Model 2 coefficient of height variation of polarization sites*

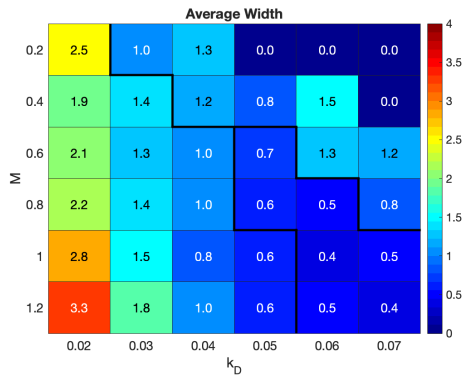


Figure 5.16: Model 1 average width of polarization sites.

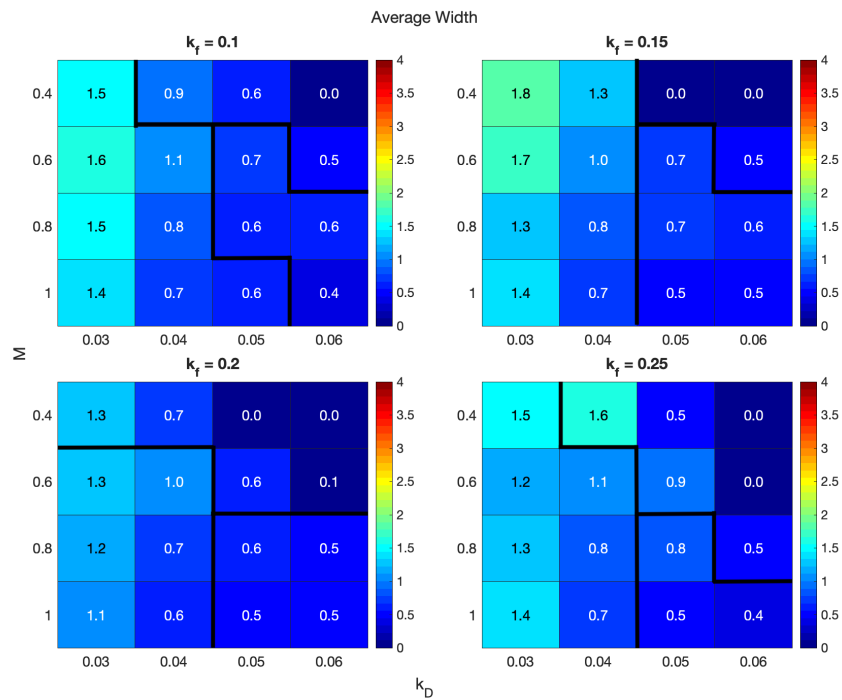


Figure 5.17: Model 2 average width of polarization sites

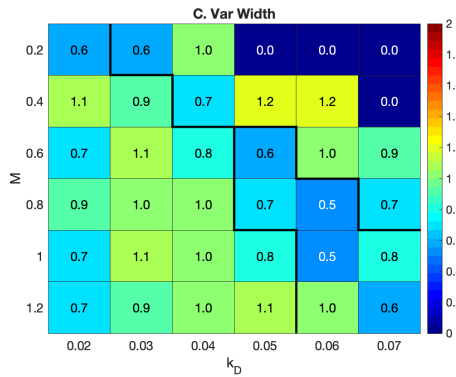


Figure 5.18: *Model 1 coefficient of variation of width of polarization sites.*

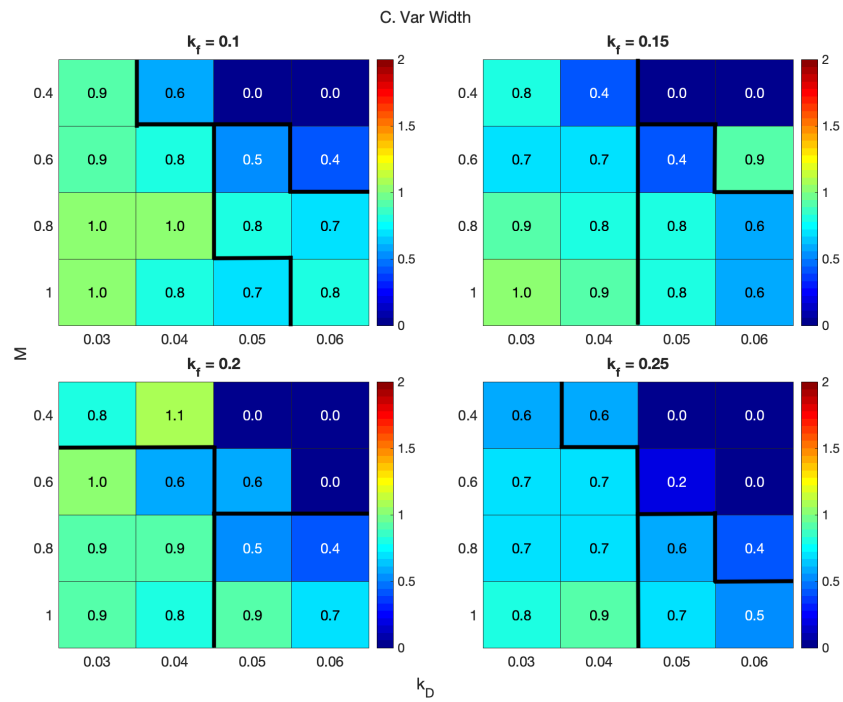


Figure 5.19: *Model 2 coefficient of variation of width of polarization sites*

In the next chapter we will summarize our conclusions and discuss possible improvements for this and future analyses.

Chapter 6

Conclusions and Discussion

In this work, we developed numerical models to test various autonomous reaction-diffusion mechanisms; in particular to investigate the role of positive and negative feedback in the polarization process. We performed ample simulation tests and compared the performance of the three numerical methods on those reaction-diffusion mechanisms. In the results section we presented a deeper study of two particular models using numerical method 1, which is FFT-based. The two reaction-diffusion models, which we refer to as model 1 and model 2, exhibit the same negative feedback mechanism in the diffusion rate, which means diffusion is self-inhibiting depending on a threshold value k_D . Model 2 also has a positive feedback in the production term that is self-promoting depending on a threshold value k_f . The results for both models reveal that feedback mechanisms are essential components to achieve and maintain a polarized concentration using a reaction-diffusion model. In particular, we can deduce that a diffusion-inhibition negative feedback is necessary to achieve polarization; model 1 further suggests that it may also be sufficient. Model 1 also reveals the intricate, positive relationship between the threshold k_D , which dictates the diffusion-inhibition activation, and the production M . More specifically, even though polarization is achieved in the majority of the parameter space, only zone 1 is capable of producing suitable results for a biological model. Zone 1 consists of those parameter sets with high k_D and large production M , this suggests that some initial diffusion must occur, that is, the

diffusion-inhibition effect should not be immediately activated as in the case of lower k_D values. Model 2 reveals that the additional feedback in the production serves to enhance the polarization results. In particular, we notice that polarization sites are more isolated as k_f , the production feedback activation threshold, increases. This effect is most noticeable in zone 2, where for model 2, despite the large size and number of polarization sites, they are separated by larger low concentration regions. This desirable attribute that the additional feedback provides comes at the price of more than twice the computation time than model 1. Additionally, when comparing the qualitative zones among the k_f parameter space slices for model 2, we observe that intermediate values of k_f have larger optimal zone. Based on these results, we are not yet able to draw a conclusion on whether one model outperforms the other. One way to improve this analysis would be to remove all simulations that do not reach steady state from our computations of averages and coefficients of variation to help improve the heatmap results. Then proceed to perform the corresponding analysis for numerical methods 2 and 3.

Bibliography Part II

- [1] Ching-Shan and Moore Chou Travis and Chang, *Signaling Regulated Endocytosis and Exocytosis Lead to Mating Pheromone Concentration Dependent Morphologies in Yeast*, FEBS Letters **586** (2012), no. 23, 4208-4214, DOI <https://doi.org/10.1016/j.febslet.2012.10.024>.
- [2] Weitao and Nie Chen Qing and Yi, *Modelling of Yeast Mating Reveals Robustness Strategies for Cell-Cell Interactions*, PLOS Computational Biology **12** (2016), 1-25, DOI <https://doi.org/10.1371/journal.pcbi.1004988>.
- [3] Alireza and Britton Ramezani Samuel and Zandi, *A multiscale chemical-mechanical model predicts impact of morphogen spreading on tissue growth*, npj Systems Biology and Applications **9** (2023), no. 16, DOI <https://doi.org/10.1038/s41540-023-00278-5>.
- [4] Xue and Fang Pan Linjing, *Auxin-induced signaling protein nanoclustering contributes to cell polarity formation*, Nat Commun **11** (2020), no. 3914.
- [5] Alan M. Turing, *The Chemical Basis of Morphogenesis*, Philosophical of the Royal Society of London. Series B, Biological Sciences **237** (1952), no. 641, 37-72.
- [6] Lloyd N. Trefethen, *Spectral Methods in MATLAB*, Society for Industrial and Applied Mathematics, 2000.
- [7] Steve and Kutz Brunton J. Nathan, *Data-Driven Science and Engineering: Machine Learning, Dynamical Systems, and Control*, Cambridge University Press, 2019.
- [8] Steven G. Johnson, *Notes on FFT-based differentiation*, 2011.